Double-Diffusive Convection Due To Lateral Thermal Forcing

JURJEN KRANENBORG

Chapter 1

Introduction and summary

This chapter serves as an introduction to the research questions and results on double-diffusive convection due to sidewall heating or cooling as presented in chapters 2 – 6 of this thesis. An example of a numerical simulation of double-diffusive convection is presented, together with a description of the mechanism of layer formation (1.1). A review of the modern literature on experimental and numerical models of double-diffusive convection due to lateral forcing then follows (1.2). Based on this review the research questions are posed that are addressed in the subsequent chapters. The contents of these chapters are briefly summarized (1.3).

1.1 Motivation

Density gradients due to temperature and salinity differences are for a large part responsible for convective transports of heat, salt and other constituents in the ocean. Some decades ago, it was assumed that these transports primarily took place in an environment dominated by large-scale turbulence resulting in locally well mixed distributions. As a result of this assumption, transport was modelled through eddy mixing coefficients relating fluxes of constituents to the mean smoothed gradients, and the measurements available were interpreted as to fit into these models in a continuous way. The availability of an increasing amount of measurements on a smaller scale, however, lead to problems with the qualitative interpretation of the data in terms of the model assumptions [*Turner*, 1981].

Nowadays, with the advent of measuring instruments that are able to record salinity and temperature profiles on centimeter scales, it has become clear that the distribution of these properties is generally not smooth; small scale (i.e. tenths to hundreds of metres) layered structures exist

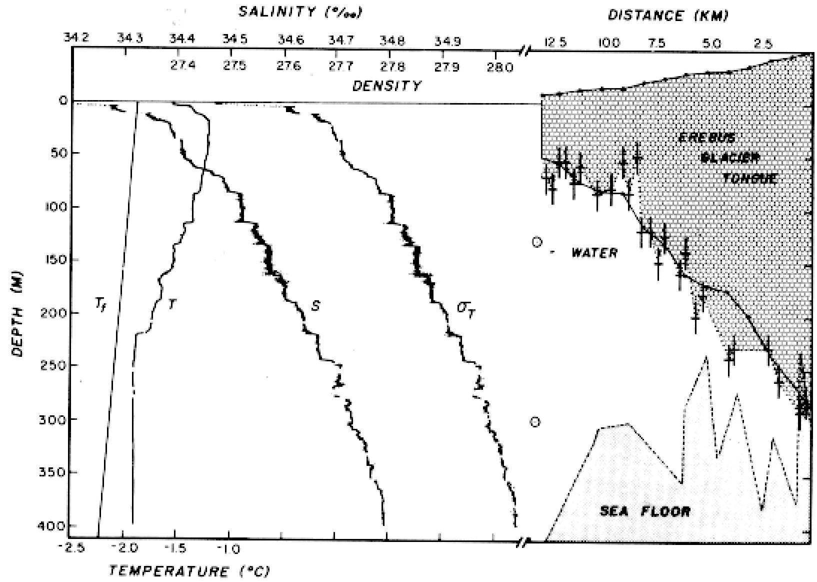

Figure 1.1: *Vertical temperature (T), salinity (S) and density (σ_T) distributions as measured about 200 meters from the upper edge of Erebus Glacier Tongue, Antarctica (from: Jacobs et al. [1981]). The profiles reveal a layered structure in the upper 300 metres of the ocean.*

in several parts of the ocean in which well mixed regions are separated by interfaces in which steep vertical property gradients are present. Often, these structures result from perturbations of a stable salt-stratified ocean by thermal gradients.

The investigations in this thesis are motivated by the recordings of layered structures in a stably stratified polar ocean in the vicinity of icebergs. In such an environment, a stable stratification in the ocean set up by a stabilizing salinity gradient is laterally cooled by the edge of an iceberg. The structures have been reported in several regions of both the northern part of the Antlantic and around the Antarctic. As an example, Fig. 1.1 shows the vertical temperature, salinity and density distributions as recorded by *Jacobs et al.* [1981] near Erebus Glacier Tongue in the Antarctic. The figure reveals a structure consisting of well-mixed horizontal layers with an average thickness of 17 metres, separated by thin diffusive interfaces in which steep temperature and salinity gradients exist. In the region where layers are present the overall distribution of heat and salt is stable, which indicates that lateral cooling of the ocean by the tongue is responsible for the layer formation, not vertical cooling at the top due to a cold atmosphere. The observed layer thickness is of the same order as would be expected from physical arguments discussed below.

The transport of heat and salt induced by these structures is expected to be quite different from the transport that is induced by thermal convection alone, and will both influence the local transports as well as the way in which the iceberg melts. This motivates a deeper study on the origins of layer formation and both the qualitative and quantitative aspects of the layer formation process.

The convection that is generated in stably stratified liquids by the opposing buoyancy effects of temperature and salinity (or a couple of different fluid constituents with this property) and their different molecular diffusivities is known as *double-diffusive* convection. Different types of motion exist depending on whether the stable stratification is provided by the component with the lowest or the highest molecular diffusivity.[1] Furthermore, the direction of the gradients heavily influences the evolution of the flow.

In this thesis we restrict ourselves to the case of a stable salt-stratified, initially motionless water column in a container to which a lateral temperature gradient is applied by heating or cooling (one of) the sidewalls. When the temperature difference between a vertical wall and the liquid exceeds a critical value, a layered system develops which consists of horizontal convection cells separated by diffusive interfaces. At this point a picture of the layer formation process is helpful. Fig. 1.2 shows the simulation of layer formation in a square cavity of 20 cm height containing a liquid which was initially motionless and linearly stratified with salt. The salinity gradient is maintained by prescribing a constant salinity difference between the horizontal walls. A lateral temperature difference far beyond the critical value is applied by heating the left boundary of the cavity with a constant value for the temperature. The sequence of pictures shows the formation of a series of layers extending horizontally into the bulk, separated by sharp interfaces. Several features of the layer formation in Fig. 1.2, like the characteristic thickness of the layers, the mixing properties and the merging of layers observed at several stages, are subject of investigation in this thesis.

The structure of the different dependent quantities in the layers in Fig. 1.2f is revealed in Fig. 1.3. In the convective layers salt is well mixed and the temperature is stably stratified. In the interface between the layers the temperature distribution is unstable and a large shear exists, but the very strong salinity gradient prevents shear instability to occur.

---

[1] If the stratification is provided by the component with the lower molecular diffusivity, the stratification is of *diffusive* type, otherwise it is of *finger* type. Although finger type systems are important in oceanography [*Schmitt*, 1994], they are not investigated in this thesis.

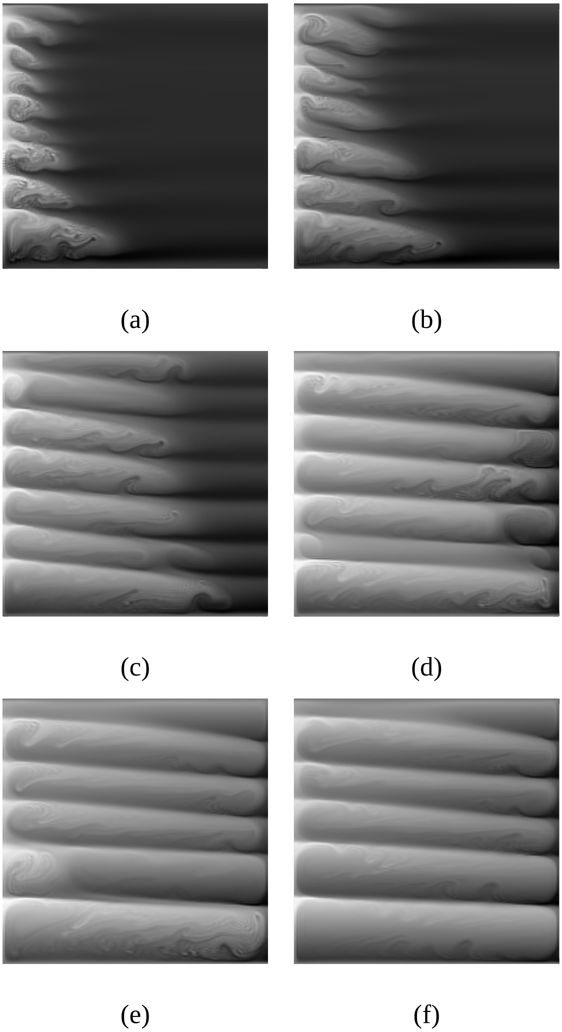

(a) (b) (c) (d) (e) (f)

Figure 1.2: *Development in time of the double-diffusive intrusions in a container of 20 cm height. At the left is the heated sidewall. Shown is the salinity distribution minus the initial linear stratification; white stands for high salinity with respect to the initial stratification while black indicates a relatively low salinity. The pictures are taken successively at 50 min. (a), 83 min. (b), 167 min. (c), 333 min (d), 500 min. (e) and 667 min. (f).*

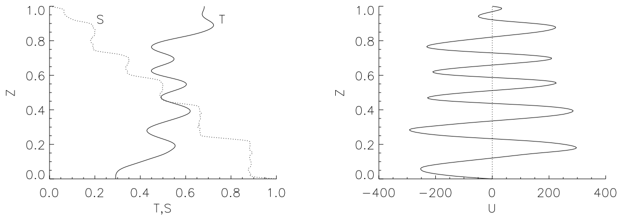

Figure 1.3: *The distribution of temperature T, salinity S and the horizontal component of the velocity U along a vertical section through the centre of the cavity for the flow as depicted in Fig. 1.2f.*

A simple physical argument for the thickness of the layers is available by considering a fluid parcel near the hot left sidewall before layer formation has started [*Chen et al.*, 1971]. Due to the sidewall heating the buoyancy of this parcel is increased and thus it rises in a vertical buoyancy driven boundary layer. Because of the low solutal molecular diffusivity the parcel remains essentially at a constant salinity as it continues to rise. The stable background stratification causes the parcel to become denser relative to its surroundings, and finally it reaches the same density as the bulk. If viscous shear forces are overcome the parcel cannot rise anymore and is forced to move laterally; double-diffusive instability results in the formation of convection cells near the heated wall which eventually evolve into the observed layers. Thus, the lengthscale over which a parcel can rise due to heating depends both on the strength of the salinity gradient and the temperature difference between the wall and the bulk of the fluid; this scale is given by

$$\eta = \frac{\alpha \Delta T}{\beta \phi_0}, \tag{1.1}$$

where ΔT is the laterally imposed temperature difference, ϕ_0 is the strength of the initial stable salinity gradient and α, β are the thermal and solutal expansion coefficients, respectively.

The observed tilt of the layers is a feature typical of double-diffusive convection; the heated fluid that is transported away from the wall loses its heat to the cooler return flow in the layer just above it through diffusion much faster than its salt, and therefore becomes heavier and tends to sink. We note that there is no qualitative difference between models that use sidewall heating and those in which sidewall cooling is applied; only the orientation of the velocity vectors and the tilt of the layers are reversed.

1.2 A review of previous work

In the past decades double-diffusive convection has developed into a separate area of research, with results available from observations, experiments and both analytical and numerical models [*Fernando and Brandt*, 1995]. In this section we present an overview of the previous work that is relevant to the research as described in this thesis. Although the motivation for these investigations often stems from oceanography, and indeed the development of the subject has been initiated in this area [*Stern*, 1960; *Stommel et al.*, 1956], double-diffusive convection has been recognised important in other areas as well. In particular, we mention its relevance for the modeling of solar ponds [*Akbarzadeh and Manins*, 1988] and magma chambers [*Fernando and Brandt*, 1995].

We start the survey with the lateral heating experiments by *Thorpe et al.* [1969]; they investigated the formation of convection cells in a salt-stratified fluid contained in a narrow, laterally heated vertical slot. Convection cells were reported along the heated wall. They suggested an instability of the thermal boundary layer to be responsible for the cell generation based on the presence of horizontal temperature and salinity gradients in the boundary layer. Furthermore they suggested that the difference in diffusivities of heat and salinity plays a central role in the built-up of the horizontal gradients. Their description thus contains the key elements of a double-diffusive mechanism, and they related it to the mechanism of layer formation in the ocean.

A criterion for the onset of layer formation and the corresponding layer size in stratified containers was established in experimental and numerical studies [*Chen et al.*, 1971; *Wirtz et al.*, 1972]. A critical Rayleigh number existed above which simultaneous layer formation occurs along the entire laterally heated wall as an instability of the thermal boundary layer. Based on a series of experiments the layer thickness was determined to be equal to the potential rise of a heated element in a stratified liquid according to the mechanism described in the introduction. At a Rayleigh number below critical successive layer formation occurred, which is induced by the horizontal boundaries and extends over only a limited vertical distance in the container.

Theoretical studies consider the onset of instability of a parallel basic flow in very simple (semi-) infinite geometries. *Thangam et al.* [1981] investigated the instability of a basic parallel flow in a differentially heated narrow (vertically infinite) slot in which a stable vertical salt gradient is present. In this case a time-independent background flow exists which can be calculated analytically. Their objective was to investigate the transition from shear instabilities (in case of a weak salt gradient) to double-diffusive instabilities for stronger salinity gradients. They found a transition from stationary steady shear instability for low weak salinity gradients, through an oscillatory instability, to steady double-diffusive instability valid for increasingly stronger salt gradients.

The stability analysis in a wide container (which is modelled by sidewall heating of a fluid which extends infinitely into the vertical and is infinite in the horizontal direction to the right) is more complex since the background flow in such a configuration is time-dependent. The stability analysis of *Kerr* [1989] and *Kerr* [1990] revealed the existence of an oscillatory instability and subcritical finite-amplitude (but unstable) flow.

Considering the available results on double-diffusive layer formation, *Huppert and Turner* [1978] suggested that the transport of meltwater from melting icebergs in polar seas is strongly influenced by the presence of double-diffusive layers due to a stable salt gradient in the ocean. In a simple experiment using a block of ice which melts in a column of salt-stratified water they showed that the fresh meltwater is mixed into the double-diffusive layers and transported mainly laterally, instead of being transported vertically along the ice edge as would be the case if the salt gradient was absent. In a profound study [*Huppert and Turner*, 1980] the layer formation was investigated for a large range of Rayleigh number using blocks of ice and both heated and cooled cylinders. The lengthscale η (1.1) was shown to be valid even for very large Rayleigh number, and transport of meltwater is mainly lateral as was suggested. Furthermore, this study revealed that the meltwater has little influence on the layer structure.

The previous investigations have been concerned mainly with an analysis of the double-diffusive instabilities which are responsible for the formation of a layered structure and the layer thickness of the developed layers. The experimental investigations of *Tanny and Tsinober* [1988] form a thorough study on the evolution of double-diffusive layers in salt stratified wide containers which are heated from one side using a prescribed time-dependent exponential temperature profile. They showed that the stability diagram for the wide container is essentially the same as for the narrow slot. The layer formation process appears to be largely independent of the temperature profile described. After layers have formed they tend to merge in, as they described it, a ”chaotic” way, i.e. no specific lengthscale for the layer thickness can be defined, until they finally attain a thickness of order η in correspondence with the results of *Chen et al.* [1971]. An investigation of the vertical density distribution across the layer interfaces revealed that layers do not merge as a result of density equalisation; they proposed interface breakdown and interface migration as the dominant mechanisms behind merging.

The presence of a linearly unstable temperature stratification in addition to the stable salt stratification - but with the total density distribution being stable - is interesting from both oceanographical and theoretical views. The presence of an unstable vertical temperature gradient in the ocean is very common as a result of cold, fresh water being on top of warmer but saltier water; examples are the cooling of polar seas by a cold atmosphere, and the outflow of warm, saline Meditterranean water in the relatively cold and fresh Atlantic Ocean near Gibraltar. In a double-diffusive context the unstable thermal stratification is interesting as a source of potential energy which may be converted into kinetic energy when the total density distribution becomes unstable due to a weakening of the salinity gradient. This energy conversion is a possible mechanism behind the so called ”self-propagation” of layers, i.e. the continuous propagation of the layer fronts even after sidewall heating has stopped.

The doubly stratified experiments by *Jeevaraj and Imberger* [1991] in laterally heated wide containers showed that the stability characteristics of a doubly stratified system are comparable to a singly stratified model, with only minor changes in critical Rayleigh number and layer thickness, but with convection more vigorous when the unstable temperature stratification becomes more important. After sidewall heating was stopped, self-propagation of layers was not observed.

Schladow et al. [1992] were able to classify the flows, depending both on the relative strength of the thermal stratification compared to the saline stratification (i.e. the vertical gravitational stability) and the lateral heatflux at the heated wall (the lateral stability). Three classes were identified; the first was identified with large lateral stability and large gravitational stability (a situation comparable with singly stratified experiments) and showed merging as a result of horizontal motions induced by the intrusions. The second class, corresponding with lower gravitational stability showed a more vigorous convection and merging was observed as a breakdown of the interfaces near the heated wall due to horizontal motions. In the third class, corresponding to low gravitational and lateral stability, self-propagation was observed after sidewall heating was removed.

The numerical work on double-diffusive systems has for the largest part concentrated on narrow container configurations in which a stable salt gradient is laterally heated from the side through one or both sidewalls. The development of layers in a container in the neighbourhood of the critical Rayleigh number was investigated by *Lee and Hyun* [1991] and they retrieved basically the same results as *Chen et al.* [1971]; for supercritical simulation layers were formed simultaneously with a thickness of order η, while in subcritical cases layer formation was successive. Since a fixed temperature difference was prescribed but saline forcing was absent, the salinity gradient became eroded and finally only the thermally driven single-cell pattern remained. In order to study the long-term behaviour of such a double-diffusive system, non-trivial steady states may be traced by fixing both the temperature at the sidewalls and the salinity at the horizontal walls. In such a configuration, *Lee et al.* [1990] showed that four different flow regimes are possible depending on the strength of the thermal and saline forcing. In addition to the simultaneous and successive regimes, a stagnant flow regime exists when the saline forcing dominates the thermal forcing, while a unicellular flow regime is present in case the thermal forcing is much larger than the saline forcing. These findings were supported by accompanying experiments [*Lee and Hyun*, 1991], which also show that the approach to the final state identifying the flow regime is not trivial; for example, in the unicellular flow regime the corresponding flow pattern is reached after subsequent merging of cells that are a result of double-diffusive instabilities.

In the latter configuration, the existence of different flow regimes encourages the investigation of the steady state structure of laterally heated narrow container configurations. The numerical study of *Tsitverblit and Kit* [1993] showed that multiple steady states exist in the double-diffusive regime due to the interplay of heat and salt. They suggested a relationship between the multiplicity of solutions and chaotic merging of layers as observed in the experiments of *Tanny and Tsinober* [1988], although the lack of a stability analysis and the differences in geometry and parameter range between the numerical model and the experiments did not improve their claim. An extended analysis of the configuration is presented in *Tsitverblit* [1995] for a larger range of parameters, showing an increasing complexity and multiplicity of solutions for larger solutal Rayleigh numbers.

1.3 Overview of the thesis

Main problem in this thesis is to determine the large scale effects that double-diffusive layered structures have on the vertical transport of fluid constituents. Therefore, our main goal is to derive effective diffusivities for heat and salt from our model results. In order to achieve this goal we have adopted the following approach. The dynamics and physics of double-diffusive layered structures due to lateral forcing are investigated in Chapters 2 – 4. In Chapter 5, the conditions for existence of layer formation and the induced transports in a simple ice-plate geometry are considered. Finally, in Chapter 6, effective vertical diffusivities for salinity are estimated.

The availability of both experimental and numerical results on the narrow container configurations using moderate values for the forcing parameters enables us to start with the analysis of these type of systems. In *Kranenborg and Dijkstra* [1995] the results of *Tsitverblit and Kit* [1993] were recomputed and extended. They showed that, studying the flow evolution towards a single, thermally dominated state in the supercritical, unicellular regime, the multiplicity of solutions was reduced, leaving only the thermally dominated unicellular solution linearly stable. Still, the multicell unstable solutions were shown to be physically relevant since during the approach to the single stable state the flow remained for a very long time close to the multicell state. These results suggest that the flow regimes found by *Lee et al.* [1990] correspond with stable states of the steady equations, while the many unstable states play a role as attractors which determine the approach towards the final, stable state. Thus it is straightforward to suggest that the boundary between two flow regimes corresponds with a stable state becoming unstable due to a singularity, and therefore we pose as a research problem for Chapter 2:

- *In which way are boundaries between the different flow regimes related to the underlying dynamical structure of the system?*

In order to answer this question the long time behaviour of flows in the narrow slot configuration as used by *Tsitverblit and Kit* [1993] and *Lee et al.* [1990] is investigated; this investigation extends the results of *Kranenborg and Dijkstra* [1995]. As in the latter study, continuation methods (see Appendix A) are applied to trace the branches of steady solutions in parameter space, while the corresponding linear stability is calculated simultaneously. The resulting structure of steady solutions reveals that boundaries between the different flow regimes as reported by *Lee et al.* [1990] are, to some extent, related to paths of bifurcation points in parameter space; the boundary between the thermally dominated unicellular flow and the double-diffusive multicell flow is determined as the path of bifurcation points in parameter space on which the unicellular pattern becomes unstable. The exact location of this boundary appears difficult to determine. Even in the unicellular regime signs of double-diffusion are present, as was already shown in *Kranenborg and Dijkstra* [1995], by the rapid evolution from a four cell pattern, through the two cell pattern corresponding with the unstable steady state, towards the stable unicellular thermally dominated pattern. In Chapter 2 it is shown through accurate calculations that the transition from the unstable two-cell pattern towards the unicellular pattern takes place through an instability as predicted by the unstable eigenvector only after a very long preconditioning phase. Here the mechanism behind the transition is interface migration. Other boundaries could not be clearly established due to an abundance of singularities occuring in the double-diffusive regime.

In Chapter 3 the evolution of the double-diffusive layers is considered. In the experimental studies of *Tanny and Tsinober* [1988]; *Jeevaraj and Imberger* [1991] and *Schladow et al.* [1992] the evolution of these layers is characterised by the occurrence of layer merging. Since layer merging increases the final scale of the layers and thereby the mixing characteristics of the flow, it is worthwhile to investigate the physical mechanisms behind it and, if possible, to relate it to the dynamical picture presented in Chapter 2. Thus, the question for Chapter 3 becomes:

- *What are the physical mechanisms behind layer merging during layer evolution?*

The time-dependent evolution of the double-diffusive instabilities is studied in the same range of Rayleigh number as the experiments of *Tanny and Tsinober* [1988] and *Jeevaraj and Imberger* [1991]. The layer scale of the simulated flows agrees very well with the various experimental results [*Chen et al.*, 1971; *Tanny and Tsinober*, 1988; *Jeevaraj and Imberger*, 1991]. The simulations on a high-resolution grid allow a detailed analysis of the layer merging process; both shear instabilities and density equalisation are ruled out as relevant. Instead, two instability mechanisms are proposed; an instability leading to layer migration as found in Chapter 2 and a differential entrainment mechanism based on a local analysis of the interface Richardson number.

If a destabilizing initial unstable temperature distribution is present in addition to a stabilizing salt gradient, and if the temperature gradient is large, then layers may continue to propagate into the bulk of the fluid even after the sidewall heating has been turned off. This behaviour has only been observed in a few experiments [*Schladow et al.*, 1992] but an analysis of the physical mechanism is not yet available. In Chapter 4, we therefore pose the following question:

- *What is the physical mechanism behind self-propagation of layers?*

In a doubly stratified system in which the sidewall heating is turned off, self-propagation of layers is shown to exist in a wide container. This is in contrast with the corresponding singly stratified system where self-propagation does not appear. Excessive transport of salt along the heated wall and intense vertical convection results in a heavy patch of fluid located near the heated wall. After sidewall forcing is stopped the patch of fluid adjusts itself to a neutrally buoyant level, which gives rise to a background flow in which local instabilities may occur. This background flow thus generates the propagation of the layers.

In an oceanographic context, vertical ice boundaries (for example ice slabs or icebergs) can provide the lateral cooling of a stably stratified fluid. The laboratory experiments of *Huppert and Turner* [1980] show that next to an ice block double-diffusive layers are formed with lengthscale η. In Chapter 5 we investigate the following questions:

- *What are the conditions for existence of layer formation near an ice plate, and how is the transport of heat and salt altered by the double-diffusive flow in such a geometry?*

A cooled solid slab is used as a simple model of an ice plate. It is shown that the thickness of the slab must be larger than the lengthscale η for layers to exist. At the lower slab edge a buoyancy jump develops which isolates the double-diffusive flows next to the slab from other fluid regions; the layer formation next to the slab takes place in the same way as in the cavity simulations of Chapters 3 and 4. The buoyancy jump causes a strong decrease of the vertical heat and salt transport, compared to the transports caused by thermal gradients only.

Finally, in Chapter 6 the effective vertical diffusivity for salt is estimated from a series of high-resolution simulations. An effective vertical thermal diffusivity could not be determined due to the absence of a vertical background temperature gradient. The vertical salt fluxes over the diffusive interfaces are shown to satisfy a well-known flux law. From these fluxes an estimate of the vertical salt diffusivity is determined for the parameter range corresponding to the simulations. Next, the estimate of the salt diffusivity is extrapolated towards oceanographic conditions, yielding a value of the same order as those determined from measurements. This result shows that some of the oceanic layered structures may be generated by double-diffusive instabilities due to lateral temperature gradients.

References

Akbarzadeh, A., Manins, P., Convective layers generated by side walls in solar ponds, *Solar Energy*, **41**(6), 521–529 (1988).

Chen, C. F., Briggs, D. G., Wirtz, R. A., Stability of thermal convection in a salinity gradient due to lateral heating, *Int. J. Heat Mass Transfer,* **14**, 57–65 (1971).

Fernando, H. J. S., Brandt, A., Recent advances in double-diffusive convection, *Appl. Mech. Rev.*, **47**(9), C1–C7 (1995).

Huppert, H. E., Turner, J. S., On melting icebergs, *Nature*, **271**, 46–48 (1978).

Huppert, H. E., Turner, J. S., Ice blocks melting into a salinity gradient *J. Fluid Mech.*, **100**, 367–384 (1980).

Jacobs, S.S., Huppert, H.E., Holdsworth, G., Drewry, D.J., Thermohaline steps induced by melting of the Erebus Glacier tongue, *J. Geophys. Res.*, **86**, 6547–6555 (1981).

Jeevaraj, C., Imberger, J., Experimental study of double-diffusive instability in sidewall heating, *J. Fluid Mech.*, **222**, 565–586 (1991).

Kerr, O. S., Heating a salinity gradient from a vertical sidewall: linear theory, *J. Fluid Mech.*, **207**, 323–352 (1989).

Kerr, O. S., Heating a salinity gradient from a vertical sidewall: nonlinear theory, *J. Fluid Mech.*, **217**, 529–546 (1990).

Kranenborg, E. J., Dijkstra, H. A., The structure of (linearly) stable double diffusive flow patterns in a laterally heated stratified liquid, *Physics of Fluids*, **7**(3), 680–682 (1995).

Lee, J. W, Hyun, M. T. & Kang, Y.S., Combined natural convection due to lateral heating in a stably stratified solution, *Int. J. Heat Mass Transfer* **33**, 869–875 (1990).

Lee, J. W. & Hyun, J. M., Double diffusive convection in a cavity under a vertical solutal gradient and a horizontal temperature gradient, *Int. J. Heat Mass Transfer*, **34**, 2423–2427 (1991).

Schladow, S. G., Thomas, E., Koseff, J. R., The dynamics of intrusions into a thermohaline stratification, *J. Fluid Mech.*, **236**, 127–165 (1992).

Schmitt, R.W., Double diffusion in oceanography, *Ann. Rev. Fluid Mech.*, **26**, 255-285 (1994).

Stern, M.E., The “salt fountain” and thermohaline convection, *Tellus*,**12**, 172–175 (1960).

Stommel, H., Arons, A.B., Blanchard, D., An oceanographic curiosity; the perpetual salt fountain, *Deep-Sea Res.*, **3**, 152–153 (1956).

Tanny, J., Tsinober, A. B., The dynamics and structure of double-diffusive layers in sidewall-heating experiments *J. Fluid Mech.*, **196**,135–156 (1988).

Thangam, S., Zebib, A. & Chen, C. F., Transition from shear to sideways diffusive instability in a vertical slot, *J. Fluid Mech.*, **112**, 151–160 (1981).

Thorpe, S.A., Hutt, P.K., Soulsby, R., The effect of horizontal gradients on thermohaline convection, *J. Fluid Mech.*, **38**, 375-400 (1969).

Tsitverblit, N., Bifurcation phenomena in confined thermosolutal convection with lateral heating: Commencement of the double-diffusive region, *Physics Fluids A.*, **7**, 718–736 (1995).

Tsitverblit, N., Kit, E., The multiplicity of steady flows in confined double-diffusive convection with lateral heating, *Physics Fluids A.*, **5**, 1062–1064 (1993).

Turner, J. S., *Buoyancy effects in fluids*, Cambridge (1973).

Turner, J. S., Small-scale mixing processes, in: *Evolution of physical oceanography; scientific surveys in honour of Henry Stommel*, Warren, B.A., Wunsch, C. (eds.), The MIT Press, Massachusetts, 236–262 (1981).

Wirtz, R. A., Briggs, D. G., Chen, C. F., Physical and numerical experiments on layered convection in a density–stratified fluid, *Geophysical Fluid Dynamics* , **3**, 265–288 (1972).

Chapter 2

A bifurcation study of double-diffusive flows

In this chapter the double diffusive layer formation process in a laterally heated liquid layer which is stably stratified through a constant vertical salinity gradient is considered. We focus on the situation for which the salt field is fixed at the upper and lower boundaries to allow for steady state solutions. The initial layer formation, subsequent layer merging and the long time evolution are considered from a dynamical systems point of view. The structure of the stationary solutions in parameter space and their linear stability is determined using continuation methods whereas transient flows are studied through direct numerical simulation. An attempt is made to identify the boundaries between different flow regimes, as observed experimentally, as paths of particular bifurcation points in parameter space. This is only partly successful due to an abundance of singularities in some parameter regimes. However, much is learned on the dynamics of these type of flows during the attempt. For instance, the evolution towards stable states at selective points in parameter space shows that unstable steady states are physically relevant because the time at which the particular instability sets in may be very long.

2.1 Introduction

When a lateral temperature gradient is applied to a motionless liquid layer which is stably stratified through a constant vertical salinity gradient ϕ_0, a buoyancy driven flow appears. This flow may become unstable when a critical value of the lateral temperature gradient is exceeded. The instabilities are shear driven for small ϕ_0, but when ϕ_0 is large the flow becomes unstable to double diffusive instabilities. The latter are due to the different thermal and solutal diffusivities. A parcel of liquid near the hot vertical wall is heated and moves upward, retaining almost all of its salt due to the relatively small saline diffusivity. As the parcel rises, the background salinity stratification causes the lateral density difference between the parcel and the bulk of the fluid to decrease. The vertical excursion is limited to the height where the parcel density is equal to that of the surrounding liquid and because of continuity it is then forced to move laterally; a layered flow pattern results.

The vertical temperature and salinity structure associated with these layers show characteristic step-like structures. Such step structures in temperature and salinity have been found over large areas in the upper ocean. Since the presence of layers significantly influences the transport of heat and salt, double diffusive convection is a potentially important transport mechanism e.g. for heat and salt in the ocean [*Schmitt*, 1994]. Apart from the oceanographic context, there are many technological motivations to study these types of flow, for example crystal growth [*Fernando and Brandt*, 1995] and heat storage in solar ponds [*Akbarzadeh and Manins*, 1988].

Much information on the layer formation process was obtained from laboratory experiments. These were performed either in narrow slots or in wide tanks. They differ also in the way the heating is imposed at the lateral walls, for example very slowly [*Thorpe et al.*, 1969] or through a particular time dependence [*Chen et al.*, 1971; *Tanny and Tsinober*, 1988; *Wirtz et al.*, 1972]. In most of the experiments three stages of flow development are observed. There is an initial stage characterized either by spontaneous cell formation along the heated wall or by flow developing from the horizontal boundaries. In the latter flows, the cells at the horizontal boundaries penetrate towards the center of the cavity during the second stage of evolution. In the first type of flows, layers merge during the second stage leading to an increase in the average thickness of the layers. Eventually, in both cases, a quasi-steady pattern forms with a layered structure over the whole container. Nice sets of pictures showing these three stages can, for example, be found in *Tanny and Tsinober* [1988].

The experiments indicate that there is a boundary in parameter space separating these two qualitatively different regimes of flow. In *Chen et al.* [1971], a boundary in parameter space was proposed as the critical value of a Rayleigh number Ra_η based on the length scale

$$\eta = \frac{\alpha \Delta T}{\beta \phi_0} \tag{2.1}$$

Here ΔT is the laterally imposed temperature difference and α, β the thermal and solutal expansion coefficients, respectively. The length scale η is directly related to the movement of a heated liquid parcel to its neutrally buoyant level. It was found [*Chen et al.*, 1971] that when Ra_η exceeds a critical value given approximately by $Ra_{\eta,cr} = 1.5\ 10^4$ the layers formed simultaneously. In this case, a layered convection pattern with a vertical lengthscale η developed [*Huppert and Turner*, 1980; *Jeevaraj and Imberger*, 1991; *Tanny and Tsinober*, 1988]. Below the critical value the layers grow successively from the horizontal walls and layers with a larger scale may develop.

Theoretical work has mainly focussed on the initial stage of layer formation as an instability of a weak buoyancy driven background flow. In the ideal situation of a vertically unbounded layer this flow is parallel, with liquid rising near the hot wall and descending along the cold wall. The parallel flow can be calculated analytically [*Thangam et al.*, 1981] and at large salinity gradient ϕ_0, it can be shown to be unstable to double diffusive instabilities for sufficiently large lateral temperature gradient. A rigorous series of studies on the instability of the boundary layer due to a gradually heated wall has been performed by *Kerr* [1989, 1990]. He demonstrated that for this case, the instability is oscillatory and that finite amplitude flows exist below the instability boundary (although these were found to be unstable).

In this chapter, we focus on the long time behavior of double diffusive layered flows in a narrow slot. The question we try to answer is whether the different flow regimes are related to a change in attractive regions in phase space of the governing system of equations. In that respect, the experimental results in *Lee et al.* [1990] and numerical results in *Lee and Hyun* [1991] are most relevant. In *Lee et al.* [1990], an experimental configuration was used for which the salt field at the horizontal walls was kept constant by using permeable membranes, maintaining a salinity difference ΔS between the walls. Here, real steady equilibria exist and can be calculated numerically in parameter space by solving for the steady equations directly. Apart from the above mentioned type of flows, which they called simultaneously formed layer flows (regime III) and successively formed layer flows (regime II), they also found two other regimes. At low buoyancy ratio[1] $R = \frac{\beta \Delta S}{\alpha \Delta T}$, a unicellular flow pattern was found (regime IV) and at very large buoyancy ratio, a very weak flow (or no flow at all) was found (regime I).

In addition to the aspect-ratio A of the liquid layer (ratio of length to depth), the Prandtl number and the Lewis number, two other parameters control the dynamics of the flow. These are the thermal Rayleigh number Ra_T based on the liquid height H (or Ra_η based on η) and the above mentioned buoyancy ratio R. The solutal Rayleigh number Ra_S is the product of Ra_T and R. The aspect-ratio, the Prandtl number and the Lewis number will be fixed throughout this study. The salt boundary conditions at the horizontal walls are chosen to allow for steady states to exist (as in *Lee et al.* [1990]). We use techniques from numerical bifurcation theory to determine branches of steady solutions in the two-dimensional parameter space spanned by Ra_η

---

[1] In literature, different symbols and definitions exist for the buoyancy ratio, a fact which may lead to some confusion. In this thesis, the symbol R is used for the buoyancy ratio based on the *horizontal* background temperature difference ΔT. The commonly used symbol R_ρ is reserved for the vertical buoyancy (stability) ratio as used in Chapter 4.

and the buoyancy ratio R. In addition, some trajectories showing the evolution of the flow are computed by direct numerical simulation at particular locations in parameter space.

Main aim of this chapter is to identify the boundaries between the different flow regimes as paths of particular bifurcation points in parameter space. The work leads to the stability boundary of the weak buoyancy driven nonparallel flow; this is a symmetry breaking bifurcation point. A lower bound for the successively layered flow regime is likely to be associated with a path of limit points on the asymmetric branch originating from this symmetry breaking bifurcation. The boundary between the unicellular flow regime and that of the simultaneously formed layer regime is associated with the instability of the unicellular flow. Further identification could not be made due to an abundance of bifurcation points in several regions of parameter space.

2.2 Formulation and Numerical Methods

A two-dimensional rectangular container (length L and height H) is filled with a Newtonian liquid with a constant thermal diffusivity κ_T and kinematic viscosity ν. A stable vertical salinity gradient is maintained within the liquid by imposing a constant salinity difference ΔS between the horizontal walls of the container; the vertical heat flux at these walls vanishes. A constant horizontal temperature difference ΔT is applied between the vertical walls, which are impervious to salt. The density ρ depends linearly on temperature and salinity and is given by $\rho = \rho_0(1 - \alpha(T^* - T_0) + \beta(S^* - S_0))$, where the zero subscript refers to reference values. The governing equations are non-dimensionalized using scales H, H^2/κ_T and κ_T/H for length, time and velocity, respectively. A dimensionless temperature T and salinity S are defined by $T = (T^* - T_0)/\Delta T$ and $S = (S^* - S_0)/\Delta S$. In terms of the streamfunction ψ and vorticity ω, where

$$u = \frac{\partial \psi}{\partial z},\; w = -\frac{\partial \psi}{\partial x},\; \omega = -\nabla^2 \psi \tag{2.2}$$

the full equations, with the usual Boussinesq approximation, are given by:

$$Pr^{-1}(\frac{\partial \omega}{\partial t} + J(\omega, \psi)) = \nabla^2 \omega + Ra_T(\frac{\partial T}{\partial x} - R\frac{\partial S}{\partial x}) \tag{2.3}$$

$$\frac{\partial T}{\partial t} + J(T, \psi) = \nabla^2 T \tag{2.4}$$

$$\frac{\partial S}{\partial t} + J(S, \psi) = Le^{-1}\nabla^2 S \tag{2.5}$$

where the Jacobian J is defined as

$$J(a, b) = \frac{\partial a}{\partial x}\frac{\partial b}{\partial z} - \frac{\partial a}{\partial z}\frac{\partial b}{\partial x} \tag{2.6}$$

At all boundaries no-slip conditions for velocity are prescribed and for the temperature and salinity the following boundary conditions hold.

$$x = 0: \; T = -\frac{1}{2}; \; \frac{\partial S}{\partial x} = 0, \; x = A: \; T = \frac{1}{2}, \; \frac{\partial S}{\partial x} = 0, \tag{2.7}$$

$$z = 0: \; S = 1, \; \frac{\partial T}{\partial z} = 0; \; z = 1: \; S = 0, \; \frac{\partial T}{\partial z} = 0. \tag{2.8}$$

The dimensionless parameters which appear in the equations above are defined as

$$Ra_T = \frac{g\alpha\Delta T H^3}{\nu\kappa_T}, \; R = \frac{\beta\Delta S}{\alpha\Delta T}, \; Pr = \frac{\nu}{\kappa_T}, \; Le = \frac{\kappa_T}{\kappa_S}, \; A = \frac{L}{H} \tag{2.9}$$

and the solutal Rayleigh number is given by

$$Ra_S = Ra_T R = \frac{g\beta\Delta S H^3}{\nu\kappa_T} \tag{2.10}$$

A relation between the Rayleigh numbers Ra_η, used in *Chen et al.* [1971], and Ra_T is $Ra_\eta = Ra_T/(R)^3$. Using $\partial S_0/\partial z = \Delta S/H$, a straightforward relation exists between the lengthscales H, η and the buoyancy ratio, i.e. $H/\eta = R$. In a liquid layer of height H, solutions with characteristic length scale η therefore correspond to R cells.

The equations and boundary conditions were discretized using a finite volume finite difference method as in *Dijkstra* [1992]. We use three types of numerical codes to study steady and transient solutions of the system of equations above. Steady states and their linear stability are calculated as a function of parameters using the continuation code presented in *Dijkstra* [1995]. A non-equidistant grid was used near the vertical boundaries in order to get an accurate representation of boundary layers. No stretching was applied in z because, in addition to the boundary layers at the horizontal walls, also large internal vertical gradients, in particular in salinity, may occur.

Two time-dependent numerical solvers, an explicit code using a fast Poisson solver and an fully implicit solver, were used. The first code has the advantage that it can be run at high resolution. However, its disadvantage is the restriction of the time step because of numerical instability. With the second code larger time steps can be taken but at lower resolution. Hence, the explicit code was used in the initial stage of the development of the flow and the implicit code in the approach to steady state. The codes were verified using standard problems and the choice of resolution and time step was based on extensive testing of the accuracy of the solutions.

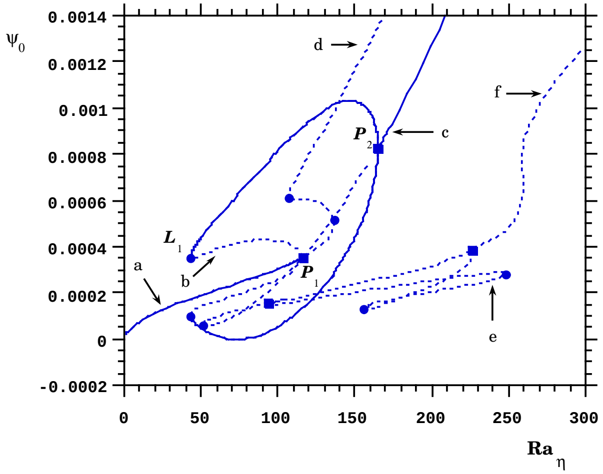

Figure 2.1: *Bifurcation diagram for $R = 3$ at small Ra_η. Note that the unstable branch starting at P_2 is not connected to P_1; the crossing is a visual effect caused by the particular choice of the monitor function.*

2.3 Results for the unicellular flow regime: $R = 3$

The Prandtl and Lewis numbers are fixed at values corresponding to the heat/salt system: $Pr = 6.7$, $Le = 101$ and the aspect–ratio A is fixed at $A = 1/2$. In a typical experiment in the unicellular flow regime, regime IV in *Lee et al.* [1990], first a 4-cell pattern is observed, thereafter cells merge until a 2-cell state is reached and finally a 1-cell solution is obtained, which appears to be a steady state of the system. In this section, we first determine the steady states of the system and subsequently study the time evolution towards the stable steady states.

2.3.1 Branches of steady solutions

In these computations, we choose Ra_η as the bifurcation parameter; when this parameter is varied, both Ra_T and Ra_S vary. In Fig. 2.1 the bifurcation diagram for $R = 3$ is shown for relatively small Ra_η; this figure was computed using a $25 * 41$ grid. On the vertical axis, a value of the streamfunction at a particular gridpoint (ψ_0) is plotted, chosen to clearly distinguish the different solution branches. Drawn (dotted) lines indicate stable (unstable) branches and bifurcation points are indicated by markers. A square is a pitchfork bifurcation and a dot indicates a limit point. At labelled points along the branches in Fig. 2.1, plots of the streamfunction

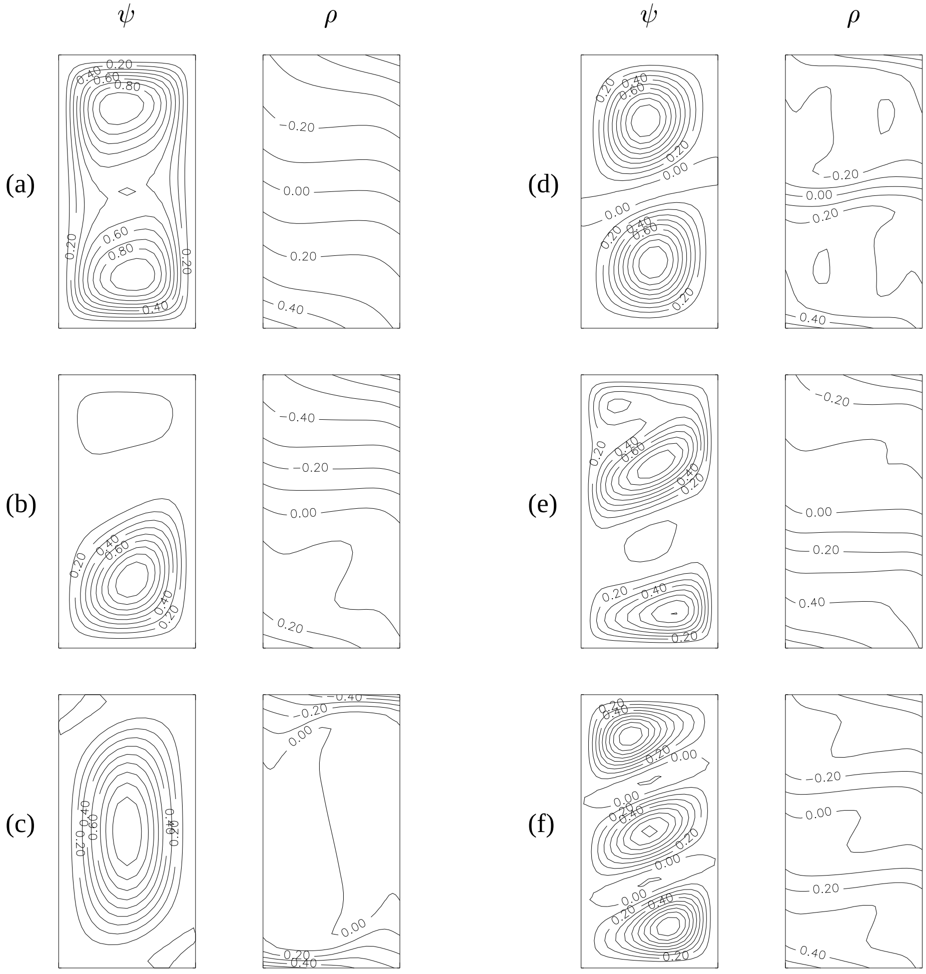

Figure 2.2: *Contour plots of the streamfunction and density at selected points in Fig. 2.1. For the density the value at the center is subtracted first. All contour levels are with respect to the maximum of the field.*

and density are shown in Fig. 2.2, where the dimensionless density ρ is computed as $\rho = Ra_T(RS - T)$.

When Ra_η is smaller than the value at L_1 in Fig. 2.1, there is a unique stable steady state consisting of two cells (Fig. 2.2a), which rotate in the same direction (counterclockwise). With

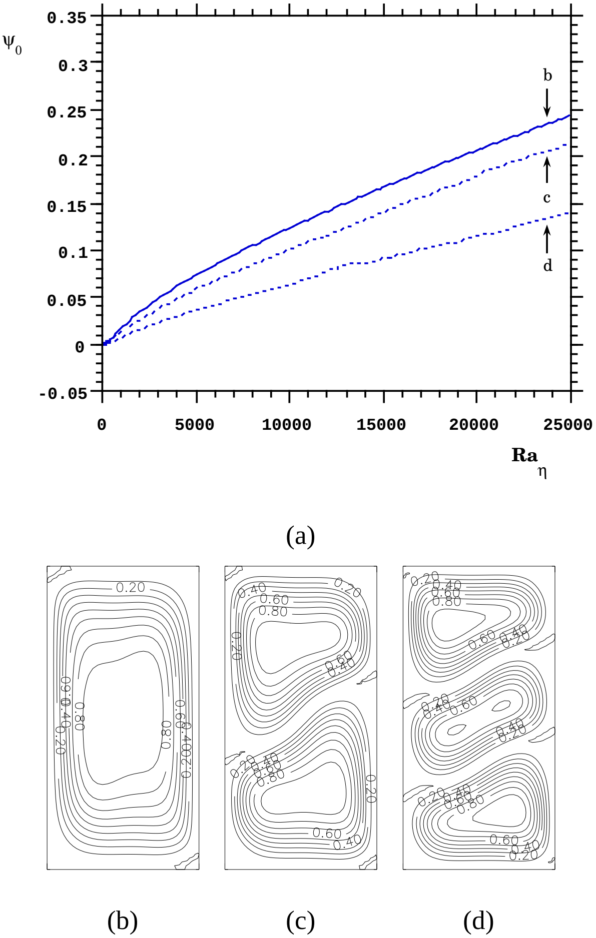

(a)

(b) (c) (d)

Figure 2.3: *Bifurcation diagram similar to that in Fig. 2.1 for* $R = 3$ *at large* Ra_η*. b-d. Flow patterns at selected points in Fig. 2.3a.*

increasing Ra_η, this 2-cell pattern becomes unstable through a subcritical pitchfork bifurcation at the point labelled P_1. This bifurcation is symmetry breaking and two branches of asymmetric solutions – but related through point-symmetry about the center of the cavity – appear. One of these solutions, a mixed 1-cell/2-cell pattern, is shown in Fig. 2.2b. Both asymmetric patterns remain unstable up to the limit point L_1, but stabilize with increasing Ra_η and remain stable up to the bifurcation point P_2. Along the branch $L_1 - P_2$, the flow pattern changes from a 2-cell to a 1-cell solution. For values of Ra_η larger than at P_2, the 1-cell pattern is the only stable pattern (Fig. 2.2c). The density is nearly homogeneous in the center of container and there is a region of weakly (statically) unstable stratification. Along the symmetric branch which continues from P_1, the 2-cell pattern is unstable. At larger Ra_η, both cells become separated by a relatively sharp interface, most clearly seen in the density distribution (Fig. 2.2d). Within each cell, the density is nearly constant in the central region, while large gradients appear near the top and bottom. In regions of upward flow, advective salt transport increases the density upwards, causing smaller gradients downstream, but larger ones upstream. In regions of downward flow, just the opposite occurs.

The branch coming down from P_2 also remains unstable. Along this branch, there are two other symmetry breaking bifurcation points. Here a curve of asymmetric solutions, an example shown in Fig. 2.2e appears; only one of these symmetry related branches is shown in Fig. 2.1. Along the symmetric branch, patterns appear with a slightly larger tilt and more cells at larger Ra_η. An example of a 3-cell pattern, sandwiching two small cells, is shown in Fig. 2.2f. The corresponding density plot shows that the regions of large gradients have disappeared indicating that the temperature determines the spatial pattern of the density and that the salt is well mixed (except at top and bottom). The tilt in the cells is caused by double diffusion; when the liquid moves away from the right (hot) wall, it looses its heat faster than its salt and therefore becomes heavier as the left wall is approached. The patterns along this part of the symmetric branch are all unstable.

In the small Ra_η regime there are multiple stable steady states over an interval $L_1 - P_2$ and unique stable steady states exist outside this interval (Fig. 2.1). Three branches extend into the region of larger Ra_η without any change in stability (Fig. 2.3a). The gradients in both velocity (Fig. 2.3b-d) and density become stronger and more concentrated near the boundaries of a cell, including the interfaces between the cells. The salt is well mixed within each cell and very sharp salt gradients appear at the interfaces giving a characteristic step structure in the vertical.

The increase in heat and salt transport due to convection, was monitored by calculating the Nusselt number $Nu = \int_0^1 \partial T/\partial x \, dz$ based on the heat flux through the vertical walls and Sherwood number $Sh = A^{-1} \int_0^A \partial S/\partial z \, dx$ based on the salt flux through the horizontal walls. It appeared that both quantities are constant over the layer within 1% as should be for steady flow. Generally, transport increases (Fig. 2.4a,b) with Ra_η because, at constant R, Ra_η controls the total buoyant forcing. The numbers along the branches in the Figs. 2.4 refer to the number of cells in the solution. As the number of cells increases they become smaller, allowing less vertical salt transfer because convection occurs on a smaller scale; this results in lower Sherwood numbers (Fig. 2.4b). With an increasing number of cells, the heat gain at the hot wall also decreases

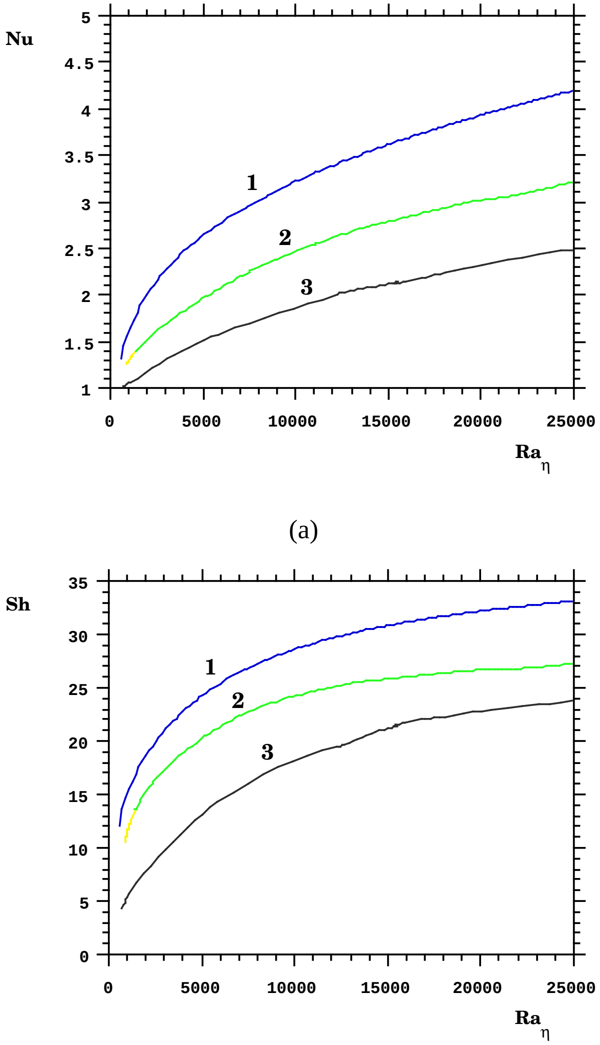

(a)

(b)

Figure 2.4: *Plot of the Nusselt number* Nu *(4a) and Sherwood number* Sh *(4b) as a function of* Ra_η *along the branches of Fig. 2.3a.*

which leads to a smaller horizontal heat transport resulting in a smaller Nusselt number (Fig. 2.4a).

Although there may be more branches of steady states which do not connect to ones in the small forcing regime, a relatively simple bifurcation structure is found over a whole range of Ra_η (At least up to $Ra_\eta = 2.5\ 10^4$, in an oceanographic context Ra_η is much larger: $Ra_\eta = O(10^9)$). There is only one stable pattern, the 1-cell solution, and one would expect long-term time-dependent calculations to approach this solution. This is in agreement with numerical results in *Lee and Hyun* [1991], where a 1-cell pattern was found for $R = 3$ and $Ra_T = 8.0\ 10^7$ (corresponding to $Ra_\eta = 2.96\ 10^6$). It is also in agreement with experimental results in *Lee et al.* [1990] since the parameters here belong to those characterizing regime IV.

2.3.2 Evolution towards steady state

The evolution of the flow in the cavity is studied from an initially motionless isothermal liquid which is stably (salt) stratified. At $t = 0$ a constant horizontal temperature difference is imposed. The initial conditions are

$$t \leq 0 \quad : \quad \psi = \omega = 0;\ S = 1 - z \tag{2.11}$$

$$t < 0 \quad : \quad T = 0 \tag{2.12}$$

$$t = 0 \quad : \quad T(x = 0) = -\frac{1}{2};\ T(x = A) = \frac{1}{2} \tag{2.13}$$

and are compatible with all boundary conditions. The $25 * 41$ grid used the determine the steady states in Fig. 2.3 proved to be too coarse, because during the initial evolution smaller scale patterns appeared. It turned out that a $49 * 81$ grid gave sufficiently accurate results in that doubling the spatial resolution and halving the time step did not show much difference over a chosen time interval. This grid size is comparable to that used in *Lee and Hyun* [1991].

For $Ra_\eta = 2.37\ 10^4$ the evolution monitored by the maximum of the streamfunction ψ_m shows three different stages (Fig. 2.5). In the first stage, a four cell solution (Fig. 2.6a) is reached in a relatively short time. The vertical length scale of the convection cells is slightly smaller than η. Consistent with Fig. 2.3a, where no 4-cell stable steady solution was found, two pairs of cells merge as time progresses and a 2-cell pattern forms (Fig. 2.6b). Both the flow pattern and the corresponding density field hardly change over a long time interval (Fig. 2.5). However, the integration was continued, because no stable 2-cell pattern was found in Fig. 2.3a. Eventually, indeed the 2-cell pattern becomes unstable, weakening the lower cell (Fig. 2.6c) and relatively quickly the 1-cell pattern (Fig. 2.6d) is reached which remains steady, consistent with Fig. 2.3a.

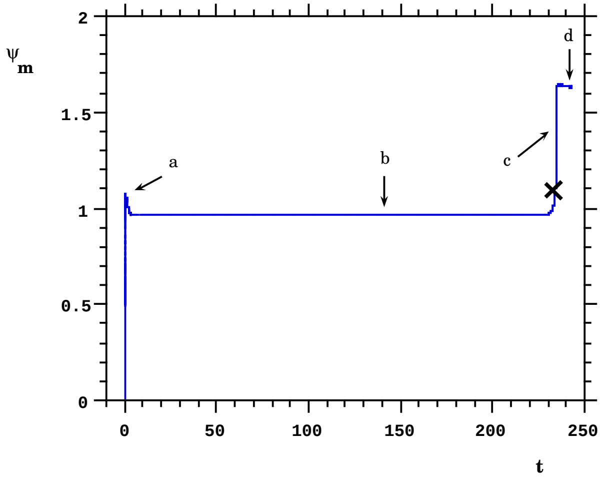

Figure 2.5: *Maximum of the streamfunction as a function of time for* $R = 3$ *and* $Ra_\eta = 2.37\ 10^4$.

At $t = 0$ a discontinuity in the temperature distribution at the vertical boundaries occurs. Since Nu is evaluated at the vertical boundaries, it is not defined at t = 0. As the 4-cell pattern is formed, Nu quickly falls to a value of about 1.9. Subsequent transitions, leading to the 2-cell and the final 1-cell pattern, cause Nu to increase for reasons described above. Similarly, the Sherwood number increases with each transition to less cells. The final values of Nu and Sh for the 2-cell and 1-cell solutions agree well with the values that can be obtained from Fig. 2.4 at $Ra_\eta = 2.37\ 10^4$. Small differences in the numerical values occur because of the different grid sizes used in the calculations ($25 * 41$ for the calculation of the steady branches and $49 * 81$ for the time dependent results).

The correspondence between the 2-cell pattern in Fig. 2.3c and Fig. 2.6b is striking. Actually, the time dependent 2-cell solution proved to be a very close approximation to the steady-state solution at the 2-cell branch in Fig. 2.3a. Using the former as a steady-state approximation for the continuation method, a steady state was reached within three Newton iterations. From Fig. 2.5 it can be seen that the unstable 2-cell solution is physically relevant, because it will be observed for a long time. Since time is scaled with the thermal diffusion time, which is in the order of a day for typical experimental configurations, the 2-cell solution may be present for a much longer time-period. i.e. about $100H^2/\kappa_T[s]$. As the salt diffusion time scale $\tau_S = H^2/\kappa_S$ based on the height of the container has this order of magnitude, the instability of the 2-cell steady solution in Fig. 2.3c is likely to be related to intercellular salt diffusion. In Fig. 2.7 the vertical profile of the

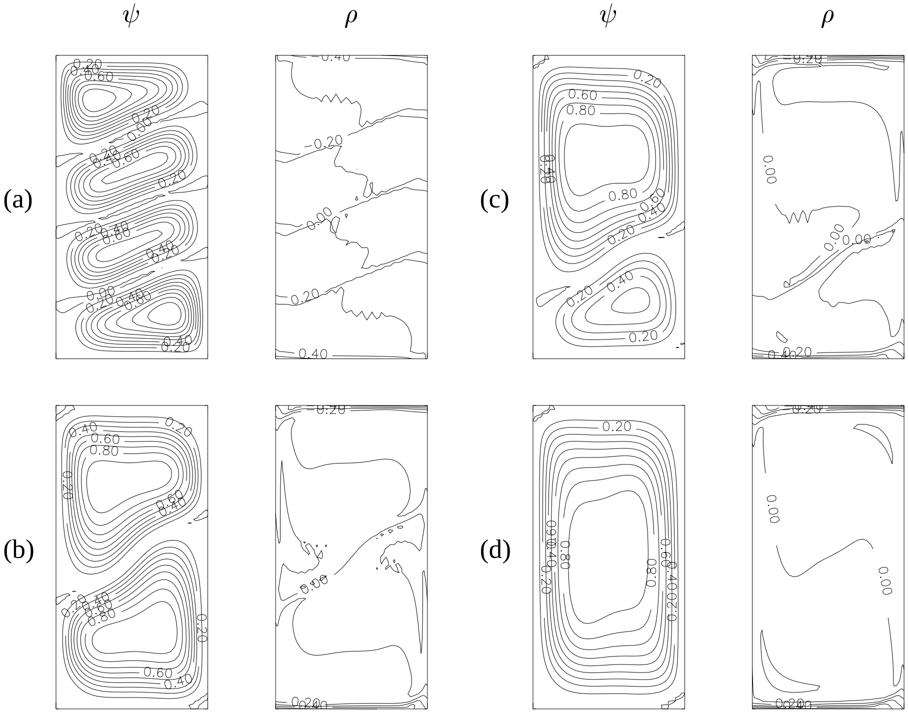

Figure 2.6: *Plot of the stream function and the density at selected points in Fig. 2.5.*

salt field ($S(A/2, z)$) at the middle of the container is shown both for the 2-cell unstable steady state (drawn line) and at the marked point in Fig. 2.5 (dotted line). Indeed, the characteristic length scale over which the salinity difference between both layers exists is of the order H.

However, when the growth factor ($\lambda = 6.78\ 10^{-2}$) – calculated by solving the linear stability problem of the 2-cell steady state – is considered, this value gives a time scale much smaller than τ_S. What actually happens is observed from the flow pattern of the most unstable mode (Fig. 2.8a) and the difference between the time dependent flow and the 2-cell steady solution (Fig. 2.8b - c) at different times. At the beginning of the quasi-steady regime, the difference solution (Fig. 2.8b) contains more modes than the most unstable mode, in particular a 4-cell pattern. It appears that a long preconditioning phase is necessary to filter out the components of the stable modes. Once these modes have decreased in magnitude (Fig. 2.8c), the instability of the 2-cell flow pattern sets in. This instability occurs indeed on a time scale set by λ as was confirmed by perturbing the 2-cell steady state with the unstable mode of very small positive amplitude

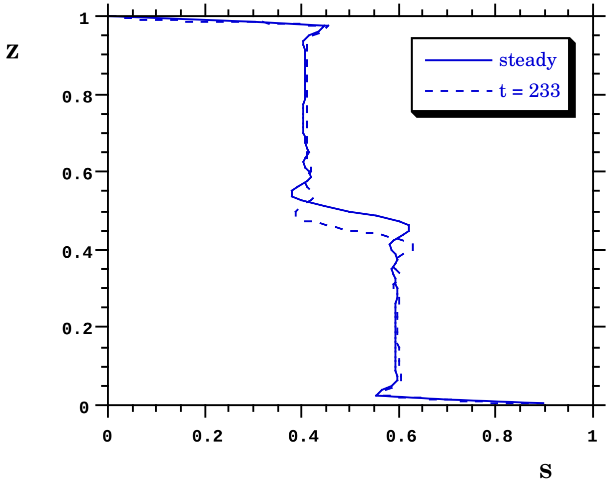

Figure 2.7: *Vertical profile of the salinity field $S(A/2, z)$ for the 2-cell steady state of Fig. 2.3c and that of the time-dependent state at the marked point in Fig. 2.5.*

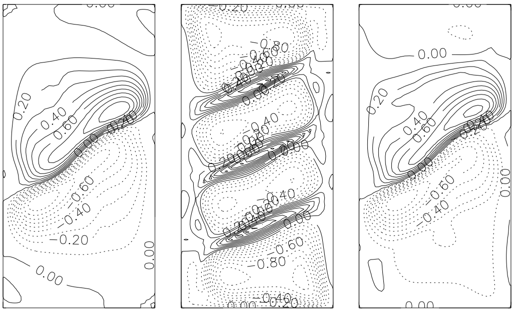

(a) (b) (c)

Figure 2.8: *a. Plot of the streamfunction of the eigenvector corresponding to the most unstable mode of the 2-cell branch ($Ra_\eta = 2.37\ 10^4$). b. Difference of the streamfunction of the transient state at $t = 7.92$ and the steady state. c. Same as b. but at $t = 2.29\ 10^2$.*

and following the evolution by time integration. Exponential growth was observed immediately; the growth factor was computed as $6.95\ 10^{-2}$, very close to the value of λ. If one perturbs the steady state with the same perturbation pattern but with a negative amplitude (this is also an eigenvector), the same instability develops and the lower cell is strengthened.

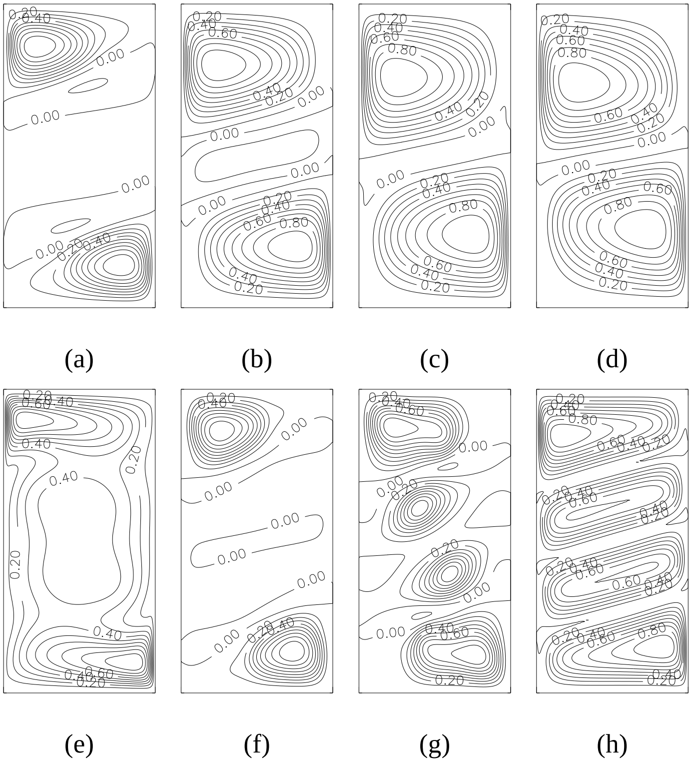

(a) (b) (c) (d)

(e) (f) (g) (h)

Figure 2.9: *Comparison of initial flow development for small* $Ra_\eta = 5.0\ 10^3$ *(panels a-d) and larger* $Ra_\eta = 2.37\ 10^4$ *(panels e-h).*

The flow development as described above depends on the value of Ra_η. We performed another transient run, at much smaller $Ra_\eta = 5.0\ 10^3$. In Fig. 2.9, a comparison between small and large Rayleigh number initial flow development is shown as a sequence of plots of the streamfunction. At small Ra_η, convection cells form at the lower and upper wall and spread out into the cavity (Fig. 2.9a-d). Further integration in time shows that a 2-cell solution appears which approaches the unstable 2-cell steady solution (as in Fig. 2.3c). At large Ra_η, two cells form in the center and the two cells close to the horizontal walls (Fig. 2.9e-h) do not extend downward. The time scale for which the evolution in Fig. 2.9a-d is shown is about a factor 10 slower than that of the development shown in Fig. 2.9e-h. Clearly, the main difference between the large and small Rayleigh number transients is the appearance of the 4-cell state.

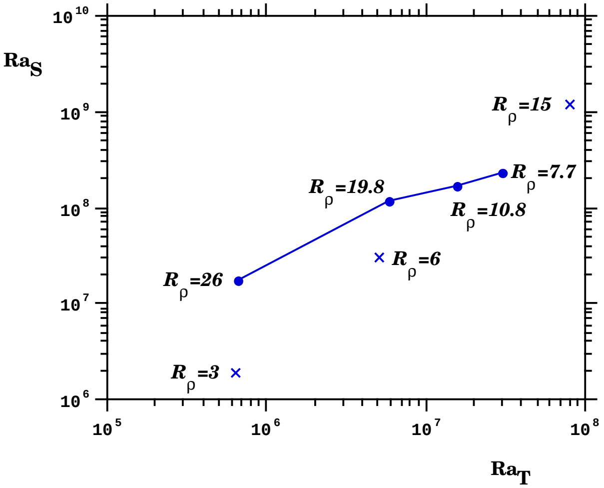

Figure 2.10: *Path of the bifurcation point corresponding to the instability of the unicellular flow. Also indicated are the locations where trajectories were computed (crosses).*

2.4 Boundaries between different flow regimes

In *Lee et al.* [1990] it was shown that in a container with the same boundary conditions and aspect-ratio as used in our model, different steady state flow regimes exist depending on the values of Ra_T and R. In this section, we try to identify the boundaries between the qualitatively different flow regimes as paths of particular bifurcation points of the underlying dynamical system.

For example, the results in *Lee et al.* [1990] suggest that the unicellular thermally dominated solution no longer exists at larger buoyancy ratio, where cells form simultaneously. A boundary between regimes III (the simultaneously formed layer flow regime) and IV (the unicellular flow regime) apparently exists. We will approach this boundary from the results in Fig. 2.3a, where three solution branches were computed up to very large Ra_η. At four fixed values of Ra_T, the flow pattern at the 1-cell branch was continued up to larger Ra_S, thereby increasing the buoyancy ratio. For each of these cases, the unicellular flow becomes unstable at a critical value of the buoyancy ratio through a pitchfork bifurcation. The path of this bifurcation in the (Ra_T, Ra_S) plane is plotted in Fig. 2.10. At larger Ra_T, the value of the buoyancy ratio is of the order 10, which is reasonably in agreement with the experiments in *Lee et al.* [1990]. This value may depend on the Lewis number, actually it is close the square root of it, but this is not further explored here. The result in Fig. 2.10 strongly supports that the boundary between region III and

IV can be identified as the instability of the unicellular flow.

However, even in the unicellular flow regime, layered flow patterns with a much smaller scale may be observed for a long time. As an example we present (Fig. 2.11) the transient flow for $R = 6$ and again $Ra_\eta = 2.37\ 10^4$. The location of the trajectory in the (Ra_T, Ra_S) plane is also indicated in Fig. 2.10. A flow pattern with vertical lengthscale η appears after some time, but changes into a 4-cell solution. The vertical distribution of fluid properties in the 4-cell solution compares qualitatively well with the case of $R = 3$: convection cells are separated by thin interfaces.

To the left of the drawn curve in Fig. 2.10, the 1-cell solutions no longer exist as stable steady states. When the points on the curve are continued towards smaller values of Ra_T, while fixing Ra_S, region III is explored. The buoyancy ratio is increased further along this path in parameter space. However, along each path computed, an enormous amount of bifurcation points and limit points appear, similar to that found in the small buoyancy ratio regime at large Ra_S [*Tsitverblit and Kit*, 1993; *Kranenborg and Dijkstra*, 1995; *Tsitverblit*, 1995]. Computationally, it became too expensive to investigate these bifurcation structures in detail. However, the results in *Kranenborg and Dijkstra* [1995] suggest that indeed multicellular flow patterns may exist as steady states. These states appear due to a combined effect of advection of salt and the appearance of stagnant flow regions when the forcing decreases which are filled up with cells when the forcing increases. These states may be unstable, as in *Kranenborg and Dijkstra* [1995], but they might be physically relevant, because also a preconditioning mechanism may be necessary for the instability to occur. With respect to the steady state structure, regimes II and III cannot be clearly distinguished since solution branches corresponding to both regimes likely exist in the same region of parameter space.

Characteristic of the patterns found in regime II is their asymmetry with respect to the center of the cavity [*Lee et al.*, 1990]. This indicates that these patterns are associated with asymmetric branches, appearing through symmetry breaking bifurcations from the symmetric branch. As an example of such an asymmetric pattern, the evolution of the flow for $R = 15$ and $Ra_\eta = 2.37\,10^4$ is shown in Fig. 2.12. The location of the trajectory in the (Ra_T, Ra_S) plane (indicated in Fig. 2.10) is certainly to the left of the curve bounding the unicellular flow regime. The numerical resolution of this particular simulation was increased to a $50*100$ grid (and the initial stages were checked with grids up to $150*300$), because small scale structures appear during the initial stages of evolution. Even with this high resolution, the flow development is quite irregular (Fig. 2.12a) and certainly no steady state has been reached at the end of the computation. The evolution of the flow pattern (Fig. 2.12b-e) is similar to the one observed in *Lee et al.* [1990] in the successively formed layer flow regime. Cells appear near upper and lower boundary, where well mixed layers

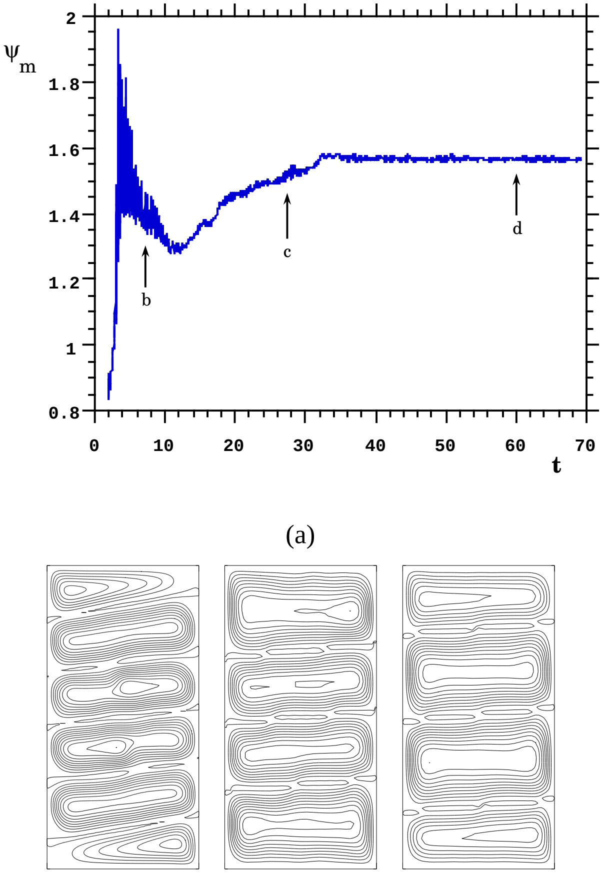

(a)

(b) (c) (d)

Figure 2.11: *a. Plot of the maximum of* ψ *as a function of time for* $R = 6$ *and* $Ra_\eta = 2.37\ 10^4$. *b-d. Flow patterns at selected points in Fig. 2.11a.*

develop. At first these cells appear symmetrically, but later an asymmetry develops as also seen in experiments. The lower cell remains well mixed as a whole whereas in the upper area two separate layers develop.

According to the experiments in *Lee et al.* [1990], regime I is characterized by a very weak flow concentrated near the horizontal walls. This weak flow is similar to that on the primary solution branch (Fig. 2.1 and Fig. 2.2a), which is obtained by continuation of the zero flow

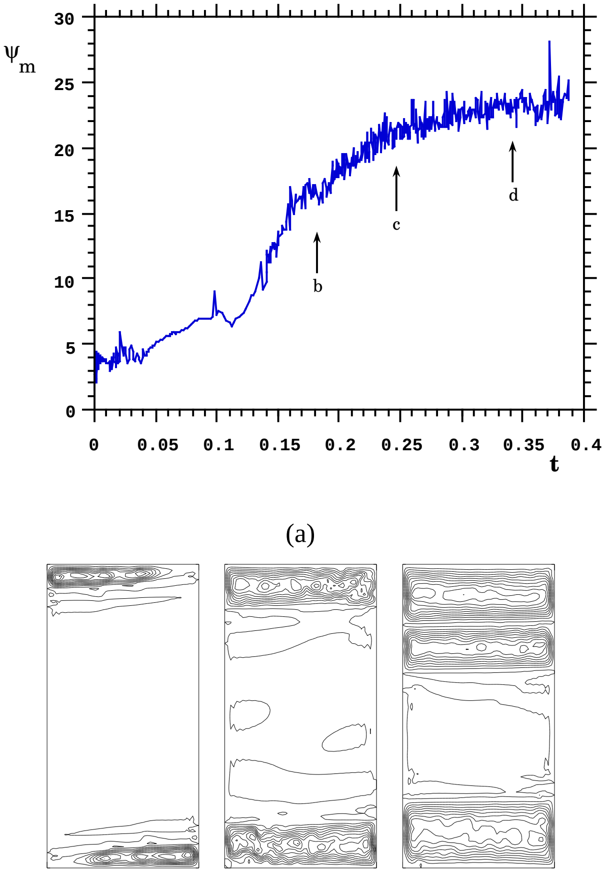

(a)

(b) (c) (d)

Figure 2.12: *Same as Fig. 2.11, but for* $R = 15$.

solution to larger thermal forcing. As regime II is associated with the occurrence of asymmetric solutions, the limit point L_1 in Fig. 2.1 is a good candidate as a boundary of different qualitative behavior since below this point, only symmetric solutions exist. However, because of the large computational effort we have not followed the path of the limit point in parameter space.

2.5 Discussion

In this chapter, we attempted to identify the different flow regimes as found in experiments of *Lee et al.* [1990] by paths of bifurcation points of the governing system of differential equations. This has been partly succesful since basically only the boundary between region III and IV can be clearly identified and a good guess is obtained for that between region I and II. The boundary between regimes II and III is not that clearly defined because of the abundance of bifurcation points in this area of parameter space. The precise reason for this is unclear but apparently the symmetric flow is very sensitive to asymmetric perturbations.

However, many interesting results have been obtained during this attempt. Above some critical value of Ra_η associated with the limit point marking the boundary between regimes I and II, multiple steady states were found over a large region of parameter space. In regime IV, the low buoyancy ratio regime, the structure of attractors is quite simple since only three branches extend to very large Ra_η. The evolution of the flow towards the unicellular stable flow was shown to remain for a long time near one of the unstable states before it undergoes an instability. This means that the unstable states are physically relevant since they may be observed for a very long time. In principle, this instability can be due to the shear in the basic state or it can be buoyancy driven, whereby double diffusion may play a role. To investigate whether shear might be a candidate, the Richardson number defined by $Ri = -\frac{\partial \rho}{\partial z} / \frac{\partial u}{\partial z}^2$ where u denotes the horizontal component of the velocity was computed. The values of Ri near the interface between the two cells (Fig. 2.6b) are quite large (> 1). Hence, it is unlikely that shear will drive the instability. Also the structure of the most unstable mode (Fig. 2.8a) does not suggest a shear driven instability, since smaller perturbation structures would be expected.

It turns out to be difficult to show why the most unstable mode, as in Fig. 2.8a, and the corresponding perturbations in the other quantities get amplified through a buoyancy driven mechanism. However, when the flow perturbation (Fig. 2.8a) is superposed on the steady state flow (Fig. 2.3c), the upper cell gets amplified, and the intensity of the lower cell is diminished. Hence, there will also be asymmetric transport of heat and salt and apparently this leads to amplification of the perturbations. During the transition from the 2-cell solution to the final 1-cell solution, there is little sign of interface breakdown, at least not in the early stages of the transition. As the interface migrates downwards, both the strength of the salinity gradient and the thickness of the interface remain nearly the same (Fig. 2.7).

Even when the parameters are chosen in the unicellular flow regime, it should be stressed that for large enough Ra_T, cellular structures with lengthscales much smaller than that of the container size may be observed for a long time. In other words, signatures of regime III may already be present in the trajectories in regime IV. These patterns likely are related to unstable steady states just as in the case $R = 3$. Similarly, at small Ra_T signatures of the successively formed flow regime can be found in the trajectories in regime IV. Hence, these results indicate that it should be difficult to distinguish the different flow regimes experimentally, in particular the boundary between the regions II and III. Indeed, *Lee et al.* [1990] and *Chen et al.* [1971] give overlapping intervals for the buoyancy ratio corresponding to the two regimes. The critical value of Ra_η as proposed by *Chen et al.* [1971] cannot be identified here as a path of a particular bifurcation point.

The boundary between region I and II is likely to be related to the appearance of the limit point on the asymmetric branches appearing from the first pitchfork bifurcation. One might ask, whether this pitchfork bifurcation is related to the double diffusive instability of a parallel flow in the limit of a vertically unbounded layer *Thangam et al.* [1981]. With $A = 1/2$ the steady state solutions near this pitchfork are not a good approximation to the parallel flow in an infinite vertical slot. We followed the path of the primary bifurcation point (P_1 in Fig. 2.1) towards smaller A, and although the steady state flow became more and more parallel, the primary bifurcation was always to an asymmetric state and not to an array of cells. These results clearly show that the primary bifurcation point and the point of instability of the parallel flow in a narrow slot are not clearly related; the upper and lower walls appear to play a dominant role in the instability of the flow.

As a summary, it appears that the underlying dynamical structure of the attractors in this particular case does not help to understand the observed flow patterns as much as one could hope for. Several aspects of the flow in experiments, other than in *Lee et al.* [1990], are neglected in this study such as impervious horizontal walls and a time - dependent heating function at the sidewall. The influence of these aspects can only be studied by direct numerical simulation using a high resolution. Although in this case, only steady patterns exist for which the salt is homogeneous, it is expected that the attractors computed with fixed salt field at top and bottom ’deform’ to slow regions in phase space. In this case, the patterns found above (e.g. the unicellular flow), may appear as quasi-steady states. However, certainly at higher buoyancy forcing, very complicated trajectories can be expected; work on this is currently in progress.

References

Akbarzadeh, A., Manins, P., Convective layers generated by side walls in solar ponds, *Solar Energy*, **41**(6), 521–529 (1988).

Chen, C. F., Briggs, D. G., Wirtz, R. A., Stability of thermal convection in a salinity gradient due to lateral heating, *Int. J. Heat Mass Transfer*, **14**, 57–65 (1971).

Dijkstra, H.A., On the structure of cellular solutions in Rayleigh-Bénard-Marangoni flows in small-aspect-ratio containers, *J. Fluid Mech.*, **243**, 73-102 (1992).

Dijkstra, H.A., Molemaker, M.J., Van der Ploeg, A., Botta, E.F.F., An efficient code to compute non-parallel flows and their linear stability, *Computers & Fluids*, **24**(4), 415–434 (1995).

Fernando, H. J. S., Brandt, A., Recent advances in double-diffusive convection, *Appl. Mech. Rev.*, **47**(9), C1–C7 (1995).

Huppert, H. E., Turner, J. S., Ice blocks melting into a salinity gradient *J. Fluid Mech.*, **100**, 367–384 (1980).

Jeevaraj, C., Imberger, J., Experimental study of double-diffusive instability in sidewall heating, *J. Fluid Mech.*, **222**, 565–586 (1991).

Kerr, O. S., Heating a salinity gradient from a vertical sidewall: linear theory, *J. Fluid Mech.*, **207**, 323–352 (1989).

Kerr, O. S., Heating a salinity gradient from a vertical sidewall: nonlinear theory, *J. Fluid Mech.*, **217**, 529–546 (1990).

Kranenborg, E. J., Dijkstra, H. A., The structure of (linearly) stable double diffusive flow patterns in a laterally heated stratified liquid, *Physics of Fluids*, **7**(3), 680–682 (1995).

Lee, J. W, Hyun, M. T. & Kang, Y.S., Combined natural convection due to lateral heating in a stably stratified solution, *Int. J. Heat Mass Transfer* **33**, 869–875 (1990).

Lee, J. W. & Hyun, J. M., Double diffusive convection in a cavity under a vertical solutal gradient and a horizontal temperature gradient, *Int. J. Heat Mass Transfer*, **34**, 2423–2427 (1991).

Schmitt, R.W., Double diffusion in oceanography, *Ann. Rev. Fluid Mech.*, **26**, 255-285 (1994).

Tanny, J., Tsinober, A. B., The dynamics and structure of double-diffusive layers in sidewall-heating experiments, *J. Fluid Mech.*, **196**,135–156 (1988).

Thangam, S., Zebib, A. & Chen, C. F., Transition from shear to sideways diffusive instability in a vertical slot, *J. Fluid Mech.*, **112**, 151–160 (1981).

Thorpe, S.A., Hutt, P.K., Soulsby, R., The effect of horizontal gradients on thermohaline convection, *J. Fluid Mech.*, **38**, 375-400 (1969).

Tsitverblit, N., Bifurcation phenomena in confined thermosolutal convection with lateral heating: Commencement of the double-diffusive region, *Physics Fluids A.*, **7**, 718–736 (1995).

Tsitverblit, N., Kit, E., The multiplicity of steady flows in confined double-diffusive convection with lateral heating, *Physics Fluids A.*, **5**, 1062–1064 (1993).

Wirtz, R. A., Briggs, D. G., Chen, C. F., Physical and numerical experiments on layered convection in a density–stratified fluid, *Geophysical Fluid Dynamics* , **3**, 265–288 (1972).

Chapter 3

Layer merging during double-diffusive layer formation

The nonlinear evolution of double-diffusive instabilities into a laterally heated stably stratified motionless liquid is studied through direct numerical simulation in a two-dimensional set-up. In this chapter, we consider liquids which are initially stratified through a constant salt gradient. The stages of evolution of the intrusions and their spatial scales correspond well with those observed in laboratory experiments. A central process in the evolution is that of layer merging. A particular case of layer merging is analysed in detail and a new physical description of this process is proposed, to which we refer as 'layer sandwiching'.

3.1 Introduction

The discovery of fine structure within the ocean has stimulated detailed studies of small-scale mixing processes. One of these processes is that of double-diffusive convection, i.e. convection in a stably stratified liquid due to different diffusivities of two components [*Turner*, 1973]. Associated with this small scale mixing process is the appearance of well mixed layers, separated by very stable interfaces over which only diffusive transport is possible. The vertical temperature and salinity structure associated with these layers show characteristic step structures. Such step structures in temperature and salinity have been found over large areas in the upper ocean. Since the presence of layers significantly influences the transport of heat and salt, double-diffusive convection is a potentially important transport mechanism e.g. for heat and salt in the ocean. Apart from the oceanographic context, there are many technological motivations to study these type of flows, for example crystal growth and the heat storage in solar ponds [*Akbarzadeh and Manins*, 1988].

A typical example of layer formation is that of a liquid which is stably stratified through a constant salt gradient ϕ_0 and which is heated through a lateral temperature gradient. The buoyancy driven flow becomes unstable when a critical value of the lateral temperature difference is exceeded. The instabilities are shear driven for small ϕ_0, but when ϕ_0 is large the flow becomes unstable to double-diffusive instabilities [*Thangam et al.*, 1981]. When a parcel of liquid near the heated wall moves upward, it retains almost all of its salt due to the very small salt diffusivity. The parcel rises to a level where its density is equal to that of the surrounding liquid and because of continuity it is then forced to move laterally; a layered flow pattern eventually results.

Much information on the layer formation process was obtained from laboratory experiments. These were performed either in narrow slots or in wide tanks, using different temperature rise curves at the heated wall and with different initial conditions. With respect to the latter, two different types can be distinguished. In singly stratified experiments, only a salinity gradient is initially present, whereas the temperature is homogeneous. In doubly stratified experiments, a destabilizing temperature gradient is also initially present such that the layer is still stably stratified. In early singly stratified experiments in narrow slots [*Chen et al.*, 1971], it was found that when a critical value of a Rayleigh number Ra_η based on the length scale

$$\eta = \frac{\alpha \Delta T}{\beta \phi_0} \tag{3.1}$$

is exceeded, layers appear over the whole length of the heated wall. Here ΔT is the imposed lateral temperature difference and α, β the thermal and solutal coefficients in the (linear) equation of state, respectively. The length scale η is directly related to the movement of a heated liquid parcel to its neutrally buoyant level. The critical value of Ra_η was determined from experiments and given approximately by $Ra_{\eta,cr} = 1.5\ 10^4$. In the supercritical flow regime, also called simultaneously formed layer regime, eventually layers with a characteristic thickness η develop [*Chen et al.*, 1971; *Huppert and Turner*, 1980; *Lee et al.*, 1990]. Below the critical value $Ra_{\eta,cr}$ the layers grow successively from the horizontal walls and layers with a larger scale than η develop.

A detailed experimental study of the evolution of intrusions in a constant vertical salt gradient was presented by *Tanny and Tsinober* [1988]. One of the sidewalls of a wide container (aspect ratio about 2.4) was heated using a prescribed temperature-rise curve. After a characteristic time t_0, a nearly constant lateral temperature difference ΔT was obtained. The flows for both the heat/salt and the heat/sugar system for different time constants t_0 in the range $75 - 8000\ [s]$ were monitored. Three different stages of development of the intrusions were distinguished. The thermal boundary layer which develops at the heated wall becomes unstable and initial layers appear. It was shown that the stability characteristics in a wide container are essentially the same as in a narrow slot [*Thangam et al.*, 1981] and do not depend on the details of the heating curve. Besides η, *Tanny and Tsinober* [1988] also used a length scale $\zeta = (\frac{\nu \kappa_S}{g \phi_0})^{\frac{1}{4}}$ to represent their results, indicating that the initial layer thickness depends only on the salinity gradient, the acceleration due to gravity g, the kinematic viscosity ν and the diffusivity of salt κ_S. In this formulation, an initial layer scale $h_i = 29.1\ \zeta$ was found and the critical Rayleigh number $Ra_{\zeta,cr}$ based on ζ was about 50.

A second stage of evolution is the transition of layers with initial thickness h_i to a slightly larger thickness due to initial layer merging. *Tanny and Tsinober* [1988] give arguments that this initial merging is due to a subsequent instability of the flow. Since a time-dependent heating curve is specified, after initiation of sidewall heating Ra_ζ increases over a time-interval of order $O(t_0)$. If the final value of Ra_ζ in a particular experiment is larger than 75, layer merging occurs at a value $Ra_\zeta = 75$. If the final value is smaller than 75, layer merging eventually occurs but it is observed after a much longer time. This is consistent with results in *Huppert and Turner* [1980], where t_0 is small and immediately layers with a final thickness were observed. Here, the initial layers have a very short lifetime and the merging stage is too short to be observed.

In the third stage of evolution, the layers approach their final thickness h_f which is characterized by the length scale η; *Tanny and Tsinober* [1988] found the relation $h_f = 0.62\ \eta$ and a similar relation was obtained by *Huppert and Turner* [1980]. In the approach to this final layer thickness, subsequent merging of layers occurs. It appears that this evolution is rather complicated, since nearly identical experiments show a different evolution and merging sequence. No specific criteria for subsequent merging could be found and it was suggested that the behavior of the flow is chaotic after the instability of the initial layers [*Tanny and Tsinober*, 1988].

More detail to the description of the subsequent layer merging process was added through the singly stratified experiments of *Jeevaraj and Imberger* [1991]. Their results are consistent with those of *Tanny and Tsinober* [1988] in that the initial merging occurs uniformly along the entire vertical sidewall. A subsequent merging process was monitored through vertical temperature profiles near the heated wall. As they describe: " ... the merging process commenced with one layer propagating slightly faster than its neighbour immediately below, and subsequently merging together ...". They also find that merging is initiated at the heated wall and is completed at the extremity of the intrusion. It is suggested that the thermal boundary layer near the heated wall penetrates the salinity interface and locally destroys the salinity step.

Despite these descriptions from laboratory experiments, the physics of layer merging process is still unclear. Theoretical work has mainly focussed on the initial stage of layer formation as an instability of a weak buoyancy driven background flow [*Thangam et al.*, 1981] and its weakly nonlinear evolution [*Kerr*, 1990]. Further progress was made through numerical simulation of the intrusions, which has only been done in two-dimensional configurations. Within narrow slots, Kamagura and Ozoe [1993] studied the evolution of the flow in both supercritical and subcritical flow regimes and found that in both regimes layers grow from the horizontal walls. Only in the supercritical case the layered structure finally extends over the entire slot, in agreement with their experimental results. *Lee and Hyun* [1991] numerically studied flows in a narrow slot configuration, where a salt difference ΔS was maintained between top and bottom, similar to their experimental set-up [*Lee et al.*, 1990]. This configuration is interesting because it allows for steady states to occur. In addition to the simultaneously and successively formed layer regimes, they find two other regimes of flow, a unicellular regime and a stagnant flow regime.

The latter configuration motivated the bifurcation studies of *Tsitverblit and Kit* [1990], *Kranenborg and Dijkstra* [1995] and the bifurcation study in Chapter 2 (*Dijkstra and Kranenborg* [1996]) for narrow slot configurations. Main result of these studies is that many steady flow patterns are possible, and that most of these flows are unstable. Within the unicellular flow regime, the structure of stable steady states was shown to be simple and to consist of only a strong thermally driven cell. However, the unstable steady states (multicellular flows) were shown to be physically relevant. The flow can remain quite long near one of these states and a long preconditioning process is needed to initiate the instability. The boundary between the unicellular flow regime and the successively formed layer regime could be associated with an instability of the unicellular flow. However, no clear boundaries were identified between the other regimes.

In this chapter, we continue the investigation of the evolution of intrusions in the supercritical case. We study the evolution of intrusions into a constant salinity gradient through a high resolution direct numerical simulation in a two-dimensional set-up. Although the flows in laboratory experiments are obviously three-dimensional, it is shown that the same stages of development and corresponding spatial and temporal scales are found. Hence, the essential physics of the evolution of the intrusions is captured by a two-dimensional model. Main contribution of this chapter is a detailed analysis of a typical case of layer merging. We propose a new description of the physics of the layer merging process, to which we refer to as 'layer sandwiching', which involves a feedback between differential entrainment and changes in the layer thickness of neighboring layers.

3.2 Formulation

A two-dimensional rectangular container (length L and height H) is filled with a Newtonian liquid with a kinematic viscosity ν and stratified through heat and salt with constant thermal diffusivity κ_T and solutal diffusivity κ_S. The density ρ of the liquid depends linearly on temperature and salinity and is given by $\rho(T^*, S^*) = \rho_0(1 - \alpha(T^* - T_0) + \beta(S^* - S_0))$, where T_0 and S_0 are (constant) reference values of the temperature and the salinity. Let ΔS and ΔT be a characteristic vertical salinity and horizontal temperature difference. The governing equations are non-dimensionalized using scales H, H^2/κ_T and κ_T/H for length, time and velocity, respectively. A dimensionless temperature and salinity are defined by $T = (T^* - T_0)/\Delta T$ and $S = (S^* - S_0)/\Delta S$. In terms of the streamfunction ψ and vorticity ω, where

$$u = \frac{\partial \psi}{\partial z},\ w = -\frac{\partial \psi}{\partial x},\ \omega = -\nabla^2 \psi, \tag{3.2}$$

the full equations , with the usual Boussinesq approximation, are given by

$$\begin{aligned} Pr^{-1}(\frac{\partial \omega}{\partial t} + \frac{\partial \psi}{\partial z}\frac{\partial \omega}{\partial x} - \frac{\partial \psi}{\partial x}\frac{\partial \omega}{\partial z}) &= \nabla^2 \omega + Ra_T(\frac{\partial T}{\partial x} - R\,\frac{\partial S}{\partial x}), && (3.3a)\\ \frac{\partial T}{\partial t} + \frac{\partial \psi}{\partial z}\frac{\partial T}{\partial x} - \frac{\partial \psi}{\partial x}\frac{\partial T}{\partial z} &= \nabla^2 T, && (3.3b)\\ \frac{\partial S}{\partial t} + \frac{\partial \psi}{\partial z}\frac{\partial S}{\partial x} - \frac{\partial \psi}{\partial x}\frac{\partial S}{\partial z} &= Le^{-1}\nabla^2 S. && (3.3c) \end{aligned}$$

The dimensionless parameters which appear in the equations above are defined as

$$Ra_T = \frac{g\alpha \Delta T H^3}{\nu \kappa_T},\ R = \frac{\beta \Delta S}{\alpha \Delta T}, \qquad Pr = \frac{\nu}{\kappa_T},\ Le = \frac{\kappa_T}{\kappa_S},\ A = \frac{L}{H}. \tag{3.4}$$

The relative importance of saline versus thermal buoyant forcing is given by the buoyancy ratio R. The lengthscale η and the Rayleigh number Ra_η can be expressed into the parameters as

$$\eta = H/R\ ;\ Ra_\eta = Ra_T/R^3. \tag{3.5}$$

In this chapter we investigate the development of intrusions into a constant salinity gradient only for a square container (A = 1). Initial conditions correspond to a motionless solution for which the salinity varies linearly with height, i.e.

$$t = 0:\ \psi(x,z) = \omega(x,z) = T(x,z) = 0\ ;\ S(x,z) = 1 - z. \tag{3.6}$$

At the left sidewall, the heating rise curve is prescribed as

$$T(x = 0, z, t) = 1 - \exp(-\frac{t}{t_0}), \tag{3.7}$$

dimensionless quantities
A = 1
Le = 101
Pr = 7
R = 5
Ra_η = $5 * 10^4$
Ra_S = $3.125 * 10^7$
Ra_T = $6.25 * 10^6$
t_0 = $1 * 10^{-3}$
dimensional quantities
H = $0.2\ (m)$
L = $0.2\ (m)$
κ_S = $1 * 10^{-9}\ (m^2 s^{-1})$
κ_T = $1 * 10^{-7}\ (m^2 s^{-1})$
ν = $7 * 10^{-7}\ (m^2 s^{-1})$

Table 3.1: *Values of both dimensionless and dimensional model parameters.*

similar to that used in the experiments of *Tanny and Tsinober* [1988]. The right sidewall is kept at the initial temperature of the bulk. The applied lateral temperature gradient is therefore constant, apart from a short initial transient phase. The upper and lower walls are isothermal. A stable salinity gradient is maintained by prescribing a constant salinity difference between the upper and lower walls; the lateral walls are impermeable to salt. In dimensionless form the remaining boundary conditions are

$$x = 0 : \frac{\partial S}{\partial x} = 0 \; ; \; x = 1 : T = 0, \frac{\partial S}{\partial x} = 0 \; ; \tag{3.8}$$

$$z = 0 : S = 1, \frac{\partial T}{\partial z} = 0 \; ; \; z = 1 : S = 0, \frac{\partial T}{\partial z} = 0. \tag{3.9}$$

At all boundaries no-slip conditions for velocity are prescribed.

3.3 Results

A 'reference' simulation is defined by the values of the parameters as given in Table 3.1. It appears difficult to perform accurate simulations in the range of buoyancy ratios used in laboratory experiments. Both in *Tanny and Tsinober* [1988] and in *Jeevaraj and Imberger* [1991], the buoyancy ratio R is within the range $30 - 50$. This is desired in experiments, because many layers develop and their average thickness can be well determined. Numerically, one does not want to simulate that many layers, because of the very high resolution required. In the 'reference' simulation, the buoyancy ratio is therefore chosen smaller than in experiments, in order to generate a smaller number of convection cells. At constant η, this means that the container height H is decreased with respect to that in experiments. Consequently, the horizontal walls of the container may have more influence on the flow development than in experiments.

The governing equations and boundary conditions are discretized spatially using second order accurate central differences on an equidistant grid. Because of the rapid evolution of the flow an explicit (first order accurate) Euler method is used to integrate in time. High spatial resolution is necessary to resolve the details of the flow, especially to resolve the large gradients in the salt field. The thickness of these saline boundary layers scales with $Pe^{-\frac{1}{2}}$ (at least in the linear case), where $Pe = \frac{U^* H}{\kappa_S}$ and U^* is a characteristic horizontal velocity scale of the convection within the layers. For the reference case, with $U^* = 5\ 10^{-5}\ [ms^{-1}]$, $Pe = 10^4$ and the estimated interface thickness is about $0.01H$. To have at least two points within each interface, an equidistant grid of 201 * 201 points is used for this simulation.

From the results in Chapter 2, it can be deduced that the parameters of the reference experiment are such that eventually a unicellular flow is reached for $t \to \infty$. In this chapter, we focus on the initial stages of evolution towards this flow. Several flow characteristics are presented in section 3.3.1 and a particular case of layer merging is observed. Thereafter, we focus on the signatures of layer merging in the heat and mass transfer rates (section 3.3.2), the overall energy balances (section 3.3.3) and in particular flow details (section 3.3.4).

3.3.1 Flow characteristics

In all simulations below, the dimensionless time t_0 in (5b) was chosen as $t_0 = 10^{-3}$. Since the thermal diffusion timescale is $4\ 10^5\ [s]$, the initial heating time is about $400\ [s]$. At the onset of layer formation the temperature at the heated wall has already reached its final value in all three cases. As is seen is Table 3.1, the 'reference' experiment corresponds to values of $Ra_\eta = 5\ 10^4$ and $R = 5$. The flow patterns at four different times are plotted in the Figs. 3.1a-d as contour plots of the streamfunction ψ. As time proceeds, convection cells form and gradually fill up the cavity with a layered flow. Cell formation happens almost simultaneously along the heated sidewall as would be expected for $Ra_\eta > Ra_{\eta,cr}$ [*Chen et al.*, 1971]. Thus, final layers are formed in about 10 hours and no subsequent layer merging is observed up to this time.

A vertical cross-section of the horizontal velocity at $x = 0.5$ and $t = 0.1$ (Fig. 3.2a) shows

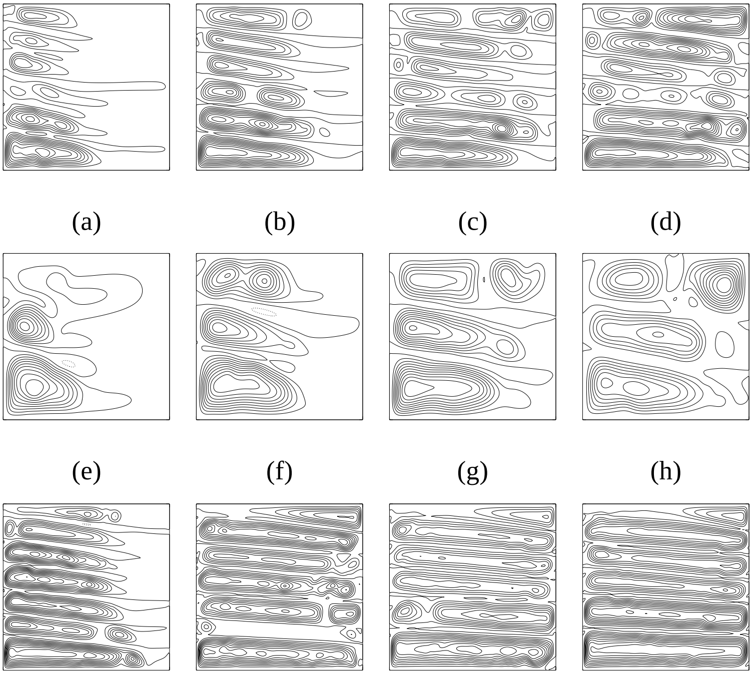

(a) (b) (c) (d)

(e) (f) (g) (h)

(i) (j) (k) (l)

Figure 3.1: *Layer formation as a function of time shown by plots of the streamfunction:* $Ra_\eta = 5\ 10^4, R = 5$ *(a-d),* $Ra_\eta = 5\ 10^4, R = 2.5$ *(e-h) and* $Ra_\eta = 2\ 10^5, R = 5$ *(i-l)); (a,e,i):* $t = 0.025$*, (b,f,j):* $t = 0.050$*, (c,g,k):* $t = 0.075$*, (d,h,l):* $t = 0.1$.

that the velocities differ in magnitude from layer to layer; typical maximal horizontal velocities are in the order of $10^{-5} - 10^{-4}\ [ms^{-1}]$. It was shown by *Jeevaraj and Imberger* [1991] that the flow within a layer (relatively far from the sidewalls) can be quite well approximated by a parallel flow driven by a layer averaged lateral temperature gradient $K(t)$. In dimensionless quantities, the equation for $u(z,t)$ follows from the dominant balance in (3.3a) between friction and buoyancy forcing, assuming a slow temporal variation of the lateral temperature gradient and the absence of a lateral salt gradient. In dimensionless form, the solution for the parallel flow becomes

$$u(z,t) = Ra_T K(t) h^3 (\frac{1}{6} z^3 - \frac{1}{4} z^2 + \frac{1}{12} z), \tag{3.10}$$

where h is the dimensionless thickness of the layer. In deriving (3.10), it is furthermore assumed

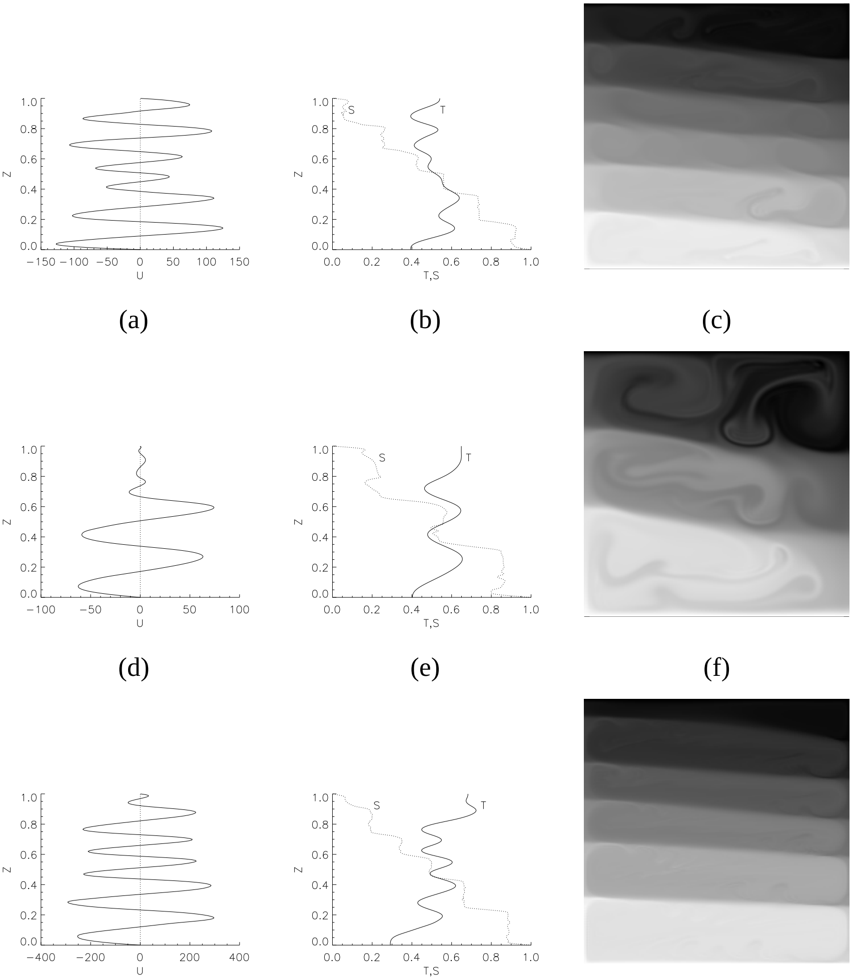

(a) (b) (c)

(d) (e) (f)

(g) (h) (i)

Figure 3.2: *Horizontal velocity (U), temperature (T) and salinity (S) profiles along a vertical section through the middle of the container and a grey-shade plot of salinity field at* $t = 0.1$*. (a-c):* $Ra_\eta = 5\ 10^4, R = 5$*, (d-f):* $Ra_\eta = 5\ 10^4, R = 2.5$*, (g-i)* $Ra_\eta = 2\ 10^5, R = 5$*.*

that the horizontal velocity vanishes at the interfaces bounding the layer. It turns out that the vertical structure (3.10) is quite a good approximation of the horizontal velocity profiles for most of the layers in Fig. 3.2a.

A vertical cross-section of temperature and salinity at $x = 0.5$ (Fig. 3.2b) clearly shows the layered structure of the flow consisting of convection cells in which salt is fairly well mixed and temperature is stably stratified, separated by thin interfaces where the salt stratification is stable but the temperature stratification is unstable. Salt can be effectively used as a tracer due to its low molecular diffusivity. A shadow plot of the salinity in Fig. 3.2c shows that indeed the salt field is nearly homogeneous within the layers, except near the right boundary, where the flow is not yet fully developed.

In the second simulation, the buoyancy ratio is lowered to $R = 2.5$ while keeping $Ra_\eta = 5\ 10^4$ the same. From (3.5) it follows that the buoyant forcing measured by Ra_T is reduced considerably. The evolution of the flow (Fig. 3.1e-h) shows that the layers have increased in scale as is expected from a smaller R and also no subsequent layer merging occurs. At $t = 0.1$ the value of the horizontal velocities is smaller (Fig. 3.2d) than in the previous case, although one expects from (3.10) that the magnitude should be about the same, since it is (note that $h \approx \eta/H$) proportional to Ra_η. The reason is that it takes longer for the flow to develop and at $t = 0.1$, the flow has not reached its maximum yet. This is also shown in the steps in the salinity profile (Fig. 3.2e) which are less pronounced than in Fig. 3.2b indicating that the salt is not well-mixed horizontally; this is confirmed in Fig. 3.2f.

In the third simulation, Ra_η is increased to $Ra_\eta = 2\ 10^5$ while $R = 5$ is the same as in the first simulation. This implies a fourfold increase in buoyant forcing and the flow is seen to evolve much quicker (Figs. 3.1i-l) than in the two simulations discussed above. The larger buoyancy forcing induces the much larger horizontal velocities in Fig. 3.2g, and these are more of equal magnitude in the different layers. The increase in velocity is only slightly smaller than the factor 4 increase expected from the idealized profile (3.10). The step structures are well-pronounced in the salinity and temperature profiles (Fig. 3.2h) and the salt is well-mixed within the layers (Fig. 3.2i). In all cases above, the number of final layers formed is $\mathcal{O}(R)$, which implies that the layers have a thickness of order η. The layer scale is therefore strongly dependent on R, whereas the time scale of evolution depends strongly on Ra_η.

An important observation from the large Ra_η case (Figs. 3.1i-l) is that there is a clear example of subsequent layer merging. The intrusions reach the cold wall before $t = 0.025$ (Fig. 3.1j) and about seven layers seem to form. However, during the evolution one of the layers disappears (Fig. 3.1k), leading eventually to a pattern of six cells at $t = 0.1$ (Fig. 3.1l). This merging process is similar to that observed, for example, in Fig. 18 of *Schladow et al.* [1992], to which they refer to as class I merging. In subsequent sections, we will focus on this particular layer merging process by looking at several signatures of this process.

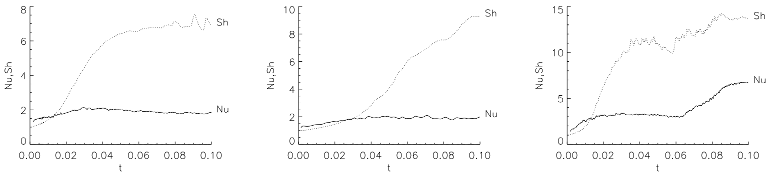

(a) (b) (c)

Figure 3.3: *Development in time of* $\overline{Nu}$ *(solid line) and* $\overline{Sh}$ *(dotted line); (a):* $Ra_\eta = 5\,10^4, R = 5$*, (b):* $Ra_\eta = 5\,10^4, R = 2.5$*, (c):* $Ra_\eta = 2\,10^5, R = 5$*.*

3.3.2 Heat and salt transport

The appropriate parameters that indicate the increase of transport due to convection are the vertically integrated horizontal heat transport and the horizontally integrated vertical salt transport. The nondimensional time in the simulation is just the Fourier number $Fo = t^* H^2/\kappa_T$ which is smaller than 0.1. Hence, the diffusive lateral heat transport $\mathcal{H}_d$ due to a temperature step (since the heating is relatively fast) is easily calculated from a one-dimensional semi-infinite layer approximation.

The local Nusselt number Nu associated with the horizontal heat transport and its vertically averaged value $\overline{Nu}$ are

$$Nu(x,z,t) = \frac{uT - \frac{\partial T}{\partial x}}{\mathcal{H}_d}\ ;\ \overline{Nu}(x,t) = \int_0^1 Nu(x,z,t)\,dz. \tag{3.11}$$

Similarly, the Sherwood numbers associated with the vertical salt transport are

$$Sh(x,z,t) = Le\,wS - \frac{\partial S}{\partial z}\ ;\ \overline{Sh}(x,t) = \int_0^1 Sh(x,z,t)\,dx. \tag{3.12}$$

The temporal development of $\overline{Nu}(0,t)$ and $\overline{Sh}(0,t)$ is shown in Fig. 3.3 for the three simulations in the previous section; for this case $\mathcal{H}_d(0,t) = \left(\frac{1}{\pi t}\right)^{\frac{1}{2}}$. As the layers have (almost) reached the right wall, $\overline{Nu}$ and $\overline{Sh}$ have the same order of magnitude in all three simulations. As the number of layers decreases for smaller buoyancy ratio, convective transport of salt becomes stronger and hence $\overline{Sh}$ increases (compare Fig. 3.3a and Fig. 3.3b). The lateral heat transport

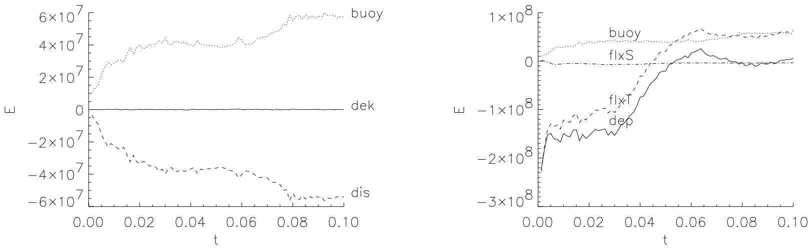

(a) (b)

Figure 3.4: *The evolution of the terms in the kinetic (3.14) and potential energy balances (3.15) for* $Ra_\eta = 2\ 10^5, R = 5$*; (a): Kinetic energy balance, (b): Potential energy balance. Annotation: dek =* $Pr^{-1} d < E_k > /dt$ *(change in kinetic energy), buoy =* $- < \rho w >$ *(buoyancy production), dis =* $< \vec{u} \cdot \nabla^2 \vec{u} >$ *(viscous dissipation), dep =* $d < E_p > /dt$ *(change in potential energy), flxT =* $Ra_T < z \nabla^2 T >$*, flxS =* $Ra_T R Le^{-1} < z \nabla^2 S >$*.*

is nearly independent of R; the increase in heat transport due to larger layer thickness is compensated by a decrease due to smaller buoyancy forcing. Larger Ra_η gives larger velocities and consequently a larger heat and salt transport as shown in Fig. 3.3c. In the latter case, one observes that $\overline{Nu}(0, t)$ approaches a value of about 3 near $t = 0.06$ but then increases again to have about a magnitude 7 at $t = 0.1$. The increase in heat transport is a signature of the subsequent layer merging process, as observed in Figs. 3.1g-i. A similar signature can be seen in the salt transport although it fluctuates much more than the heat transport.

3.3.3 Energy balances

The volume averaged kinetic and potential energy balances can be derived easily from the governing equations. A nondimensional density, the (local) kinetic energy E_k and potential energy E_p are defined as follows:

$$\rho = Ra_T(RS - T); E_k = \frac{1}{2}(\vec{u} \cdot \vec{u})\ ;\ E_p = \rho z, \tag{3.13}$$

where $\vec{u} = (u, w)$ is the velocity vector. The global kinetic energy balance is derived by taking the inner product of $\vec{u}$ with the momentum balance and integrate the result over the flow domain

Ω. One obtains

$$Pr^{-1}\frac{d}{dt} < E_k > \; = \; < \vec{u}\cdot\nabla^2\vec{u} > - < \rho w > \; ; \; < \cdot >= \int_\Omega \cdot \, dxdz. \tag{3.14}$$

The global potential energy balance is obtained by multiplying (3.3b) with $-zRa_T$, (3.3c) with zRa_TR, add and integrate the result over the flow domain. This gives

$$\frac{d}{dt} < E_p >=< \rho w > -Ra_T(< z\nabla^2 T > -RLe^{-1} < z\nabla^2 S >) \tag{3.15}$$

The evolution of terms in the kinetic and potential energy balances is presented in the Figs. 3.4 for the case $Ra_\eta = 2\,10^5, R = 5$. At all times, the primary kinetic energy balance is between viscous dissipation $< \vec{u}\cdot\nabla^2\vec{u} >$ and buoyancy production by the flow (equal to $< -\rho w >$) (Fig. 3.4a). The change in kinetic energy $d < E_k > /dt$ is orders of magnitude smaller. Initially, from $t = 0$ to about $t = 0.025$, all terms in the kinetic energy balance increase in amplitude showing the evolution of the double-diffusive instabilities. Between $t = 0.025$ and about $t = 0.06$, both buoyancy production and dissipation remain fairly constant. Layer merging is associated with an increase in buoyancy production (and an increase of dissipation), since this term increases from $t = 0.06$ up to $t = 0.1$.

Because the Lewis number is large ($Le = 101$), the contribution of changes in the salt concentration and the salt fluxes at the boundaries of the flow domain to the change in potential energy (Fig. 3.4b) is small. The buoyancy production and the term $< z\nabla^2 T >$ determine the change in potential energy. During the first stage of the evolution, this change is strongly negative since potential energy is converted into kinetic energy by the instability of the initial flow. During the merging process, the release of potential energy decreases and there is even a small interval, where the potential energy production is positive. The latter feature is absent at lower forcing (in the other two simulations considered) and is another signature of the layer merging process.

3.3.4 Analysis of flow details

We further investigate the layer merging as observed in the Figs. 3.1i-l. In the Figs. 3.5, six shadow plots of the density are shown at different times between $t = 0.025$ and $t = 0.075$. In Fig. 3.5a, the dot is exactly at the same position as the one in Fig. 3.5f. For ease of description, we label the disappearing layer with M and those bounding this layer above and below with $M+$ and $M-$, respectively. The interfaces bounding M clearly move to each other during the merging and finally a new interface is established between $M-$ and $M+$ nearly at the position halfway layer M before merging (Fig. 3.5f). This seems different from the usual interface migration

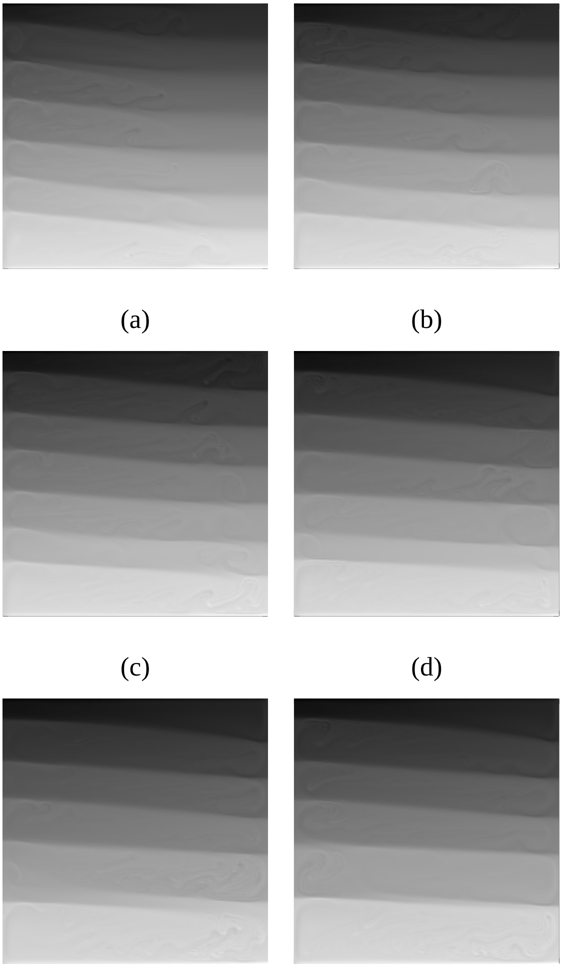

(a) (b)

(c) (d)

(e) (f)

Figure 3.5: *Density profiles showing subsequent layer merging,* $Ra_\eta = 2\ 10^5, R = 5$*, the dots in (a) and (f) are on the same position; (a):* $t = 0.025$*, (b):* $t = 0.03125$*, (c):* $t = 0.0375$*, (d):* $t = 0.05$*, (e):* $t = 0.0625$*, (f):* $t = 0.075$*.*

[*Linden*, 1976] where one of the interfaces remains stationary. From the Figs. 3.5, it is not clear whether merging starts near the heated wall or elsewhere. At $t = 0.025$ (Fig. 3.5a), the interface between M and $M+$ is vaguer near the heated wall, but at other times (for example Fig. 3.5d)

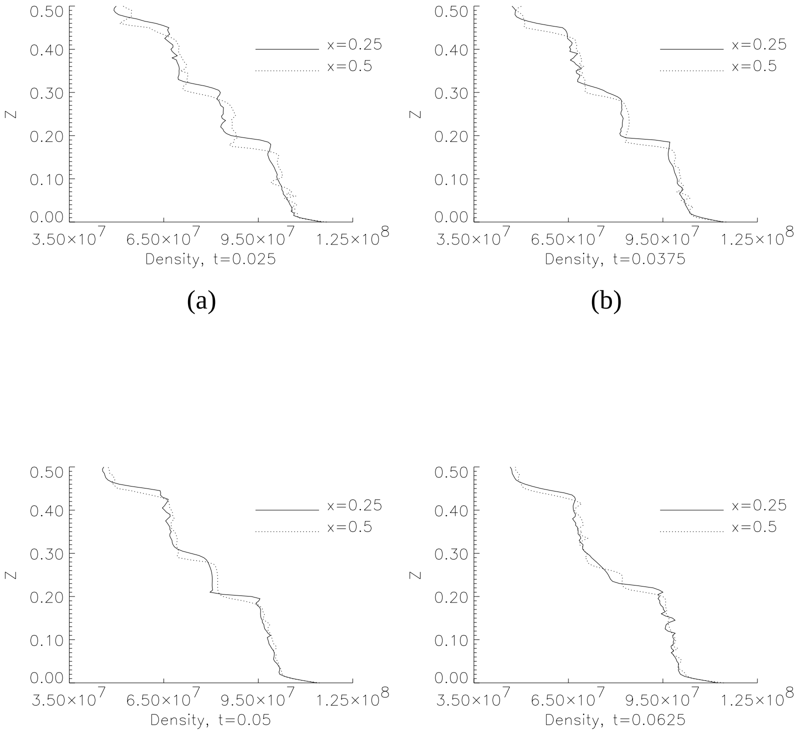

(a) (b)

(c) (d)

Figure 3.6: *The subsequent merging process revealed by two vertical sections (near the wall and through the centre) of the density at different instants. For clarity only the lower half of the sections is shown; (a):* $t = 0.025$, *(b):* $t = 0.0375$, *(c):* $t = 0.05$, *(d):* $t = 0.0625$.

the interface between $M-$ and M appears vaguer near the cold wall.

We first consider the evolution of the buoyancy jump between both interfaces bounding M. In Fig. 3.6, vertical sections are shown of the density at two positions ($x = 0.25$ and $x = 0.5$) within the layers. Although there are some locations where the flow appears unstably stratified, the results clearly show that merging is not related to the development of an unstable stratification and subsequent mixing. This supports the remark made by *Tanny and Tsinober* [1988] that an unstable stratification is not necessary for layer merging to occur. By comparing the profiles at both locations, it is observed that the layer M disappears first at $x = 0.25$ and later on at $x = 0.5$ (Fig. 3.6d), supporting the view that layer merging starts at the heated wall. In Fig. 3.7, the horizontal velocity and the temperature are plotted along the same sections. The horizontal velocity within the layer M decreases to zero and the unstable temperature stratification over both the interfaces bounding layer M is eroded during the merging process. There appears to be a phase lag in this development between the evolution of the temperature and the horizontal velocity profile, with the former leading the latter. The interface M is shown to disappear earlier in the temperature profile than in the horizontal velocity profile. By only looking at the temperature, the layer M appears to disappear first at $x = 0.5$ rather than at $x = 0.25$ (Fig. 3.7b-c) contrary to that seen for the density in Fig. 3.6. The salt field clearly is important for the changes in the spatial pattern during the layer merging process.

The results in Fig. 3.7 motivate to look at the origin of the velocity decrease within layer M. According to (3.10), the horizontal velocity can change due to variations in the layer thickness (h) or changes in the lateral temperature gradient ($K(t)$). By computing the horizontal heat balance over a vertical section of the layer [*Jeevaraj and Imberger*, 1991], it can be shown that the lateral temperature gradient depends on changes in layer thickness. However, when the spatial gradients in the layer thickness remain small, as is observed in Fig. 3.5, this effect is small and K(t) can be assumed constant during the layer merging.

Changes in layer thickness may be caused by changes in the entrainment rate [*Turner*, 1973]. This motivates to look for a measure of this entrainment rate, i.e. the Richardson number, defined by

$$Ri = -\frac{\frac{\partial \rho}{\partial z}}{\left[\frac{\partial u}{\partial z}\right]^2}. \tag{3.16}$$

At $t = 0.0375$, which is before merging, shadow plots of the salinity and Ri are shown in Fig. 3.8a and Fig. 3.8b, respectively. In Fig. 3.8b, a dark area indicates locations where Ri is relatively small, whereas it is relatively large at light areas; the precise shading values are given in the caption. Within the layers, Ri is smaller than zero, which is characteristic of strong convective activity. However, along an interface Ri increases from the heated wall to the cold wall. A smaller value of Ri indicates a less stable interface between layers, and a larger entrainment rate is expected.

The position of the interface is determined by the location where the horizontal velocity changes sign. In Fig. 3.8c, the values of Ri exactly at the interfaces between M and $M+$ and between M and $M-$ (at $x = 0.1$) are plotted at several instants prior to merging. During

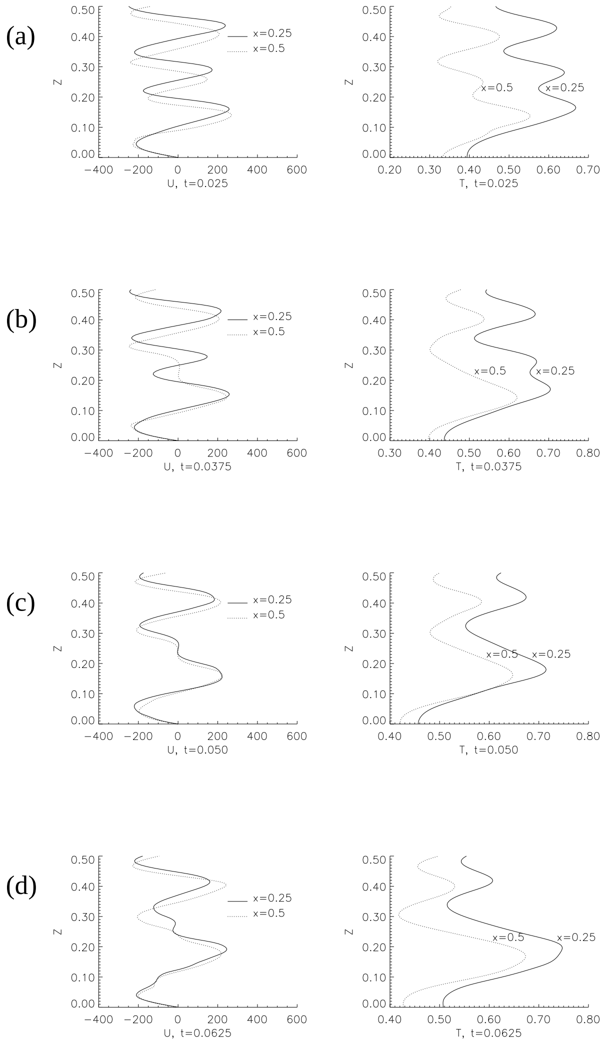

Figure 3.7: *Cross sections of the horizontal velocity U and temperature T, as in Fig. 3.6; again only the lower half of the sections is shown. (a): $t = 0.025$, (b): $t = 0.0375$, (c): $t = 0.05$, (d): $t = 0.0625$.*

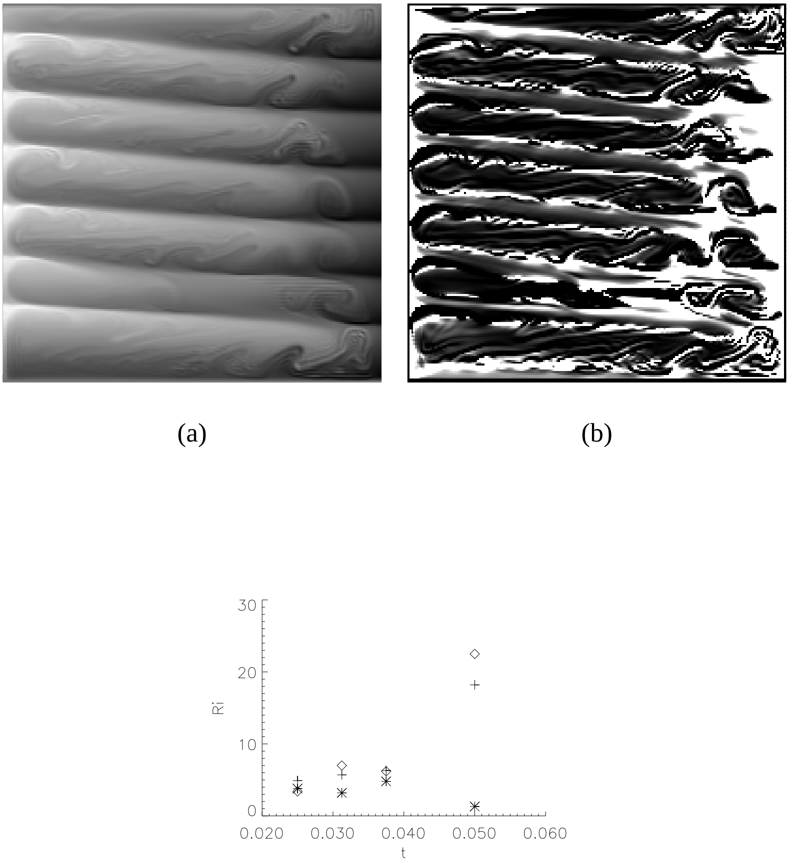

(a) (b)

(c)

Figure 3.8: *(a): Grey-shade plot of salinity minus initial stratification at $t = 0.0375$, just before subsequent merging sets in; white corresponds to a maximum and black to a minimum in salinity. (b): The same as (a) but for Ri; white corresponds to $Ri \geq 16$, black corresponds to $Ri \leq 0$; (c): Temporal development of Ri near the heated wall $(x = 0.1)$ for the first three interfaces from below. The results for the first, second and third interface are annoted with a plus, star and diamond respectively. At $t = 0.06$ and beyond, the second interface does not exist anymore.*

merging, where layer M ceases to exist, the values of Ri of the surrounding interfaces strongly increase, indicating that these interfaces become more stable.

3.4 Discussion

The results from the two-dimensional numerical simulations of the evolution of intrusions into a stratified liquid show many features also observed in experiments. This *a postiori* justifies the use of the two-dimensional model; the dominant physics of layer formation and merging appears to be captured by such a model. Focus of this work was on the subsequent layer merging process as observed in one of the simulations. Based on these results we propose the following physical picture of this process.

Again, we refer to the layers M, $M-$ and $M+$ as the layer which eventually disappears, its lower and its upper neighbor, respectively. The results on the distribution of Ri indicate (Fig. 3.8b) that the entrainment rate along the interface bounding M and $M-$ is not constant along the interface. Assume now that the interface between M and $M-$ is locally displaced upward. Since the velocity gradients in layer $M-$ are largest near the heated wall (giving smaller Ri), largest displacements will occur there. By the direct change in the layer thickness, the horizontal velocity, according to (3.10), locally decreases in layer M whereas it increases in layer $M-$. The higher velocities in layer $M-$ then lead to a larger entrainment upwards and thereby to a further displacement of the interface upwards. This view is also consistent with the observation by *Tanny and Tsinober* [1988] that the thermal boundary layer near the heated wall penetrates the interface and locally destroys the salinity step. Because the velocities in layer M decrease, the stronger convection in layer $M+$ will cause consequently a downward migration of the interface between M and $M+$.

Hence, the interfaces bounding M and $M-$ and M and $M+$ move towards each other, consistent with observations in the Figs. 3.6 and 3.7. Because the velocities increase in both layers $M-$ and $M+$, the buoyancy production increases (Fig. 3.4) and the horizontal heat transport as well as the vertical salt transport increases (Fig. 3.3). As the interfaces have reached each other and layer M has disappeared, the stability of the resulting interface increases because of the larger density difference over the newly formed interface (Fig. 3.6). This is reflected in the larger values of Ri of this interface after merging (Fig. 3.8c) and also in the positive potential energy production found in Fig. 3.4b, which indicates a restratification of the flow.

An alternative, dynamical systems point of view of this process is obtained using the results presented in Chapter 2. In the unicellular flow regime, many (unstable) steady states exist at large Ra_η. It was shown that a trajectory may remain a very long time near such an unstable state. Eventually, this state is left through an instability and the flow evolves to a situation with more layers. Although the instability mechanism was not described, it was suggested to be associated with the movement of the interface between the layers. In view of the description of the physics above, this instability may be identified in terms of the feedback between differential entrainment and changes in the layer thickness.

One can view the flow prior to merging to be near such an unstable steady state, to which the flow trajectory is attracted along the stable manifold. The differential entrainment along the interfaces separating the layers can be considered as finite amplitude perturbations on this unstable steady state. Because many steady states are present, these perturbations easily induce a transition to another state with less layers. The transitions are basically dependent on how differential entrainment is able to drive the trajectory into the unstable manifold of the underlying steady state prior to merging. This view may explain why different experiments, with the same set-up and parameters, are likely to give very different merging sequences.

References

Akbarzadeh, A., Manins, P., Convective layers generated by side walls in solar ponds, *Solar Energy*, **41**(6), 521–529 (1988).

Chen, C. F., Briggs, D. G., Wirtz, Stability of thermal convection in a salinity gradient due to lateral heating, *Int. J. Heat Mass Transfer*, **14**, 57–65 (1971).

Dijkstra, H. A., Kranenborg, E. J., A bifurcation study of double-diffusive flows in a laterally heated stably stratified liquid layer, *Int. J. Heat Mass Transfer*, **39**, 2699–2710 (1996).

Huppert, H. E., Turner, J. S., Ice blocks melting into a salinity gradient *J. Fluid Mech.*, **100**, 367–384 (1980).

Jeevaraj, C., Imberger, J., Experimental study of double-diffusive instability in sidewall heating, *J. Fluid Mech.*, **222**, 565–586 (1991).

Kamagura, K., Ozoe, H., Experimental and numerical analyses of double diffusive convection, *Int. J. Heat Mass Transfer*, **36**, 2125–2134 (1993)

Kerr, O. S., Heating a salinity gradient from a vertical sidewall: nonlinear theory, *J. Fluid Mech.*, **217**, 529–546 (1990).

Kranenborg, E. J., Dijkstra, H. A., The structure of (linearly) stable double diffusive flow patterns in a laterally heated stratified liquid, *Physics of Fluids*, **7**, 680–682 (1995).

Lee, J. W, Hyun, M. T. & Kang, Y.S., Confined natural convection due to lateral heating in a stably stratified solution, *Int. J. Heat Mass Transfer* **33** , 869–875 (1990).

Lee, J. W. & Hyun, J. M., Double diffusive convection in a cavity under a vertical solutal gradient and a horizontal temperature gradient, *Int. J. Heat Mass Transfer*, **34** , 2423–2427 (1991).

Linden, P. F., The formation and destruction of fine-structure by double-diffusive processes, *Deep-Sea Res.*, **23**, 895–908 (1976).

Schladow, S. G., Thomas, E., Koseff, J. R., The dynamics of intrusions into a thermohaline stratification, *J. Fluid Mech.*, **236**, 127–165 (1992).

Tanny, J., Tsinober, A. B., The dynamics and structure of double-diffusive layers in sidewall-heating experiments, *J. Fluid Mech.*, **196**,135–156 (1988).

Thangam, S., Zebib, A. & Chen, C. F., Transition from shear to sideways diffusive instability in a vertical slot, *J. Fluid Mech.*, **112**, 151–160 (1981).

Tsitverblit, N., Kit, E., The multiplicity of steady flows in confined double-diffusive convection with lateral heating, *Physics Fluids A.*, **5**, 1062–1064 (1993).

Turner, J.S., *Buoyancy effects in fluids*, Cambridge (1973).

Chapter 4

The physics behind self-propagating layers

Flows developing in initially doubly stratified systems are considered, i.e. in addition to a stabilizing salinity distribution a destabilizing temperature distribution is present. Lateral heating of such a system results in the formation of intrusions consisting of laterally expanding convection cells separated by diffusive interfaces. Although the development of the intrusions is qualitatively similar to that in singly stratified liquids, important differences occur when the initial destabilizing temperature gradient becomes large. When the lateral heating is turned off, intrusions are still able to propagate. The main contribution of the chapter is a detailed study of the physics of this self-propagation process.

4.1 Introduction

Double-diffusive convection, i.e. convection in a stably stratified liquid due to different diffusivities of two components [*Turner*, 1973] is a potentially important mixing process of heat and salt in the ocean [*Schmitt*, 1994]. Clear signatures of this process are well mixed layers, separated by very stable interfaces over which only diffusive transport is possible. A typical case where these layers occur is a laterally heated liquid which is initially stably stratified through a constant vertical salt gradient. Laboratory experiments [*Wirtz et al.*, 1972; *Jeevaraj and Imberger*, 1991] have provided the scales of these layers in terms of parameters of the flow. In Chapter 3 of this thesis [*Kranenborg and Dijkstra*, 1996], which was concerned with the layer merging process of intrusions developing in an initially singly stratified liquid, the experimental results were shortly reviewed. If the lateral temperature gradient is ΔT and the initial density gradient ϕ_0, then the characteristic layer scale is

$$\eta = \frac{\alpha \Delta T}{\beta \phi_0} \tag{4.1}$$

where α and β are the expansion coefficients in the linear equation of state relating density changes to temperature and salinity changes, respectively.

In experiments, also situations have been considered in which, apart from a stabilizing salt gradient $\frac{\partial S_0}{\partial z}$, a destabilizing temperature gradient $\frac{\partial T_0}{\partial z}$ was initially present [*Jeevaraj and Imberger*, 1991; *Schladow et al.*, 1992]. Motivation for these experiments was the potential ability to tap energy from the initial thermal stratification. Layers may continue to propagate even when sidewall forcing is turned off, a process called self-propagation. The doubly stratified systems are particularly interesting in an oceanographic context because the presence of an additional unstable temperature gradient is common in the upper parts of the ocean [*Jacobs et al.*, 1981].

Jeevaraj and Imberger [1991] anticipated the self-propagation of intrusions for relatively low values of the vertical stability ratio R_ρ, defined as

$$R_\rho = \frac{\beta \frac{\partial S_0}{\partial z}}{\alpha \frac{\partial T_0}{\partial z}} \tag{4.2}$$

However, even at the smallest value of $R_\rho = 2.5$, they did not observe it.

Extensive experimental and numerical work on the evolution of intrusions in doubly stratified systems was presented in *Schladow et al.* [1992]. Instead of a wall temperature rise as in *Jeevaraj and Imberger* [1991], they use a constant lateral heat flux forcing q. They classify the flows according to the values of R_ρ and a lateral stability parameter R_l, defined as

$$R_l = \frac{\frac{\alpha q}{k}}{\alpha \frac{\partial T_0}{\partial z} - \beta \frac{\partial S_0}{\partial z}} \tag{4.3}$$

where k is the thermal conductivity. In the case of high lateral and gravitational stability (small R_l and large R_ρ, class I) the system behaves like the singly stratified case. Within the layers, the temperature is stably stratified and the salt is well mixed. As the lateral heating becomes more important (class II) convection becomes more vigorous and the layer thickness increases. The salinity is generally well mixed or slightly unstable stratified within the layers and convection due to salt-fingering is possible. In the case of very low gravitational and lateral stability (class III), both heat and salt are well-mixed within the layers. Under conditions of small R_ρ and relatively large R_l, self-propagation of layers is observed.

In this chapter, the evolution of intrusions into a doubly stratified liquid is studied through direct numerical simulation in a two-dimensional set-up. At a low stability ratio, self-propagation of intrusions is found and several characteristics of this process are obtained. Based on the analysis of the numerical results, two energy sources for the self-propagation are identified. First, local instabilities which develop ahead of the intrusions may transfer energy used for the propagation. This source is similar to that proposed in *Schladow et al.* [1992]. Another source of energy is shown to come from the global adjustment of the density field.

4.2 Formulation

The model is similar to that in Chapter 3 but shortly repeated for convenience. A two-dimensional rectangular container (length L and height H) is filled with a Newtonian liquid with a kinematic viscosity ν and stratified through heat and salt with a constant thermal diffusivity κ_T and solutal diffusivity κ_S. The governing equations are non-dimensionalized using scales H, H^2/κ_T, κ_T/H, ΔS and ΔT for length, time, velocity, salinity and temperature, respectively. The equations describing the evolution of the flow are the two-dimensional Navier-Stokes equations and the conservation equations of heat and salt given in Chapter 3 in terms of the streamfunction ψ and the vorticity ω.

Apart from the Prandtl number $Pr = \frac{\nu}{\kappa_T}$, the Lewis number $Le = \frac{\kappa_T}{\kappa_S}$ and the aspect ratio $A = \frac{L}{H}$, the relevant parameters in these equations are the thermal Rayleigh number Ra_T, the buoyancy ratio R, the length scale η and the Rayleigh number Ra_η based on η

$$Ra_T = \frac{g\alpha\Delta T H^3}{\nu\kappa_T},\ R = \frac{\beta\Delta S}{\alpha\Delta T},\ ;\eta = H/R\ ;\ Ra_\eta = Ra_T/R^3 \tag{4.4}$$

At all boundaries no-slip conditions for velocity are prescribed. At the left sidewall, the heating rise curve is prescribed as

$$T(x=0,z,t) = 1 - \exp(-\frac{t}{t_0}) \tag{4.5}$$

and the right sidewall is assumed to be isolated. This situation is similar to that in the experiments by *Jeevaraj and Imberger* [1991]. All walls are impermeable to salt; in dimensionless form the remaining boundary conditions are

$$x = 0 : \frac{\partial S}{\partial x} = 0\ ;\ x = 1 : \frac{\partial T}{\partial x} = 0, \frac{\partial S}{\partial x} = 0\ ; \tag{4.6}$$

$$z = 0 : \frac{\partial S}{\partial z} = 0, \frac{\partial T}{\partial z} = 0\ ;\ z = 1 : \frac{\partial S}{\partial z} = 0, \frac{\partial T}{\partial z} = 0 \tag{4.7}$$

dimensionless quantities
A = 1
Le = 101
Pr = 7
R = 5
Ra_η = $5 * 10^4$
Ra_T = $6.25 * 10^6$
t_0 = $1 * 10^{-3}$
dimensional quantities
H = $0.2\ (m)$
L = $0.2\ (m)$
κ_S = $1 * 10^{-9}\ (m^2 s^{-1})$
κ_T = $1 * 10^{-7}\ (m^2 s^{-1})$
ν = $7 * 10^{-7}\ (m^2 s^{-1})$

Table 4.1: *Values of both dimensionless and dimensional model parameters.*

4.3 Results

A 'reference' experiment is defined by the values of the parameters as given in Table 4.1. As in Chapter 3, the thermal diffusion time scale is $4\ 10^5 [s]$ and all dimensionless times below are with respect to this time. The initial conditions are different from those in Chapter 3 in that there is, in addition to a stabilizing salt gradient, now also a destabilizing temperature gradient. The initial conditions introduce the stability ratio R_ρ and become

$$t = 0 : T_0(x, z) = -R{R_\rho}^{-1} z \ ; \ S_0(x, z) = 1 - z. \tag{4.8}$$

The limiting singly stratified case is obtained as $R_\rho \to \infty$.

A value of $R_\rho = 1.5$ is potentially in the regime of self-propagation [*Schladow et al.*, 1992]. To be able to make comparisons with the singly stratified flows in Chapter 3, the buoyancy ratio R is chosen such that the initial density gradient based on (4.8) is the same as the initial density gradient in the standard case in Chapter 3 ($R = 5$); this results in $R = 15$. Due to the initial vertical temperature gradient, the lengthscale η and therefore the Rayleigh number Ra_η vary linearly with z. The initial temperature distribution and Ra_η were prescribed such that at $z = 1/2 : Ra_\eta = 5\ 10^4$, which is the standard value in Chapter 3. Hence, for $z < 0.5$ ($z > 0.5$) the buoyancy forcing is weaker (stronger) than that at $z = 0.5$, because the lateral temperature

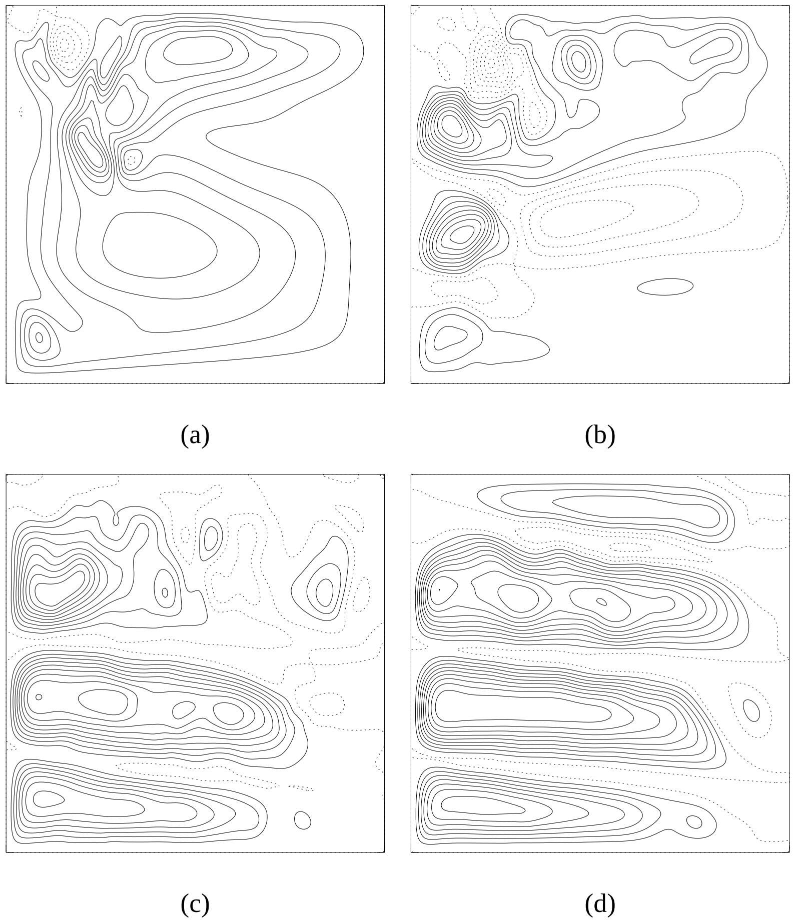

Figure 4.1: *Contour plots of the streamfunction, showing the development of layers in the doubly stratified case,* $Ra_\eta = 5\ 10^4, R = 5$*; (a):* $t = 0.005$*, (b):* $t = 0.01$*, (c):* $t = 0.05$*, (d):* $t = 0.1$.

difference (between wall and liquid far from the heated wall) decreases with z.

4.3.1 Flow characteristics

We first consider a cavity with aspect ratio $A = 1$ as in Chapter 3 and use the same numerical methods and the same resolution ($201 * 201$ equidistant gridpoints). The layer development for the standard case $Ra_\eta = 5\ 10^4$ and $R = 15$ is presented in the Figs. 4.1, where four snapshots of

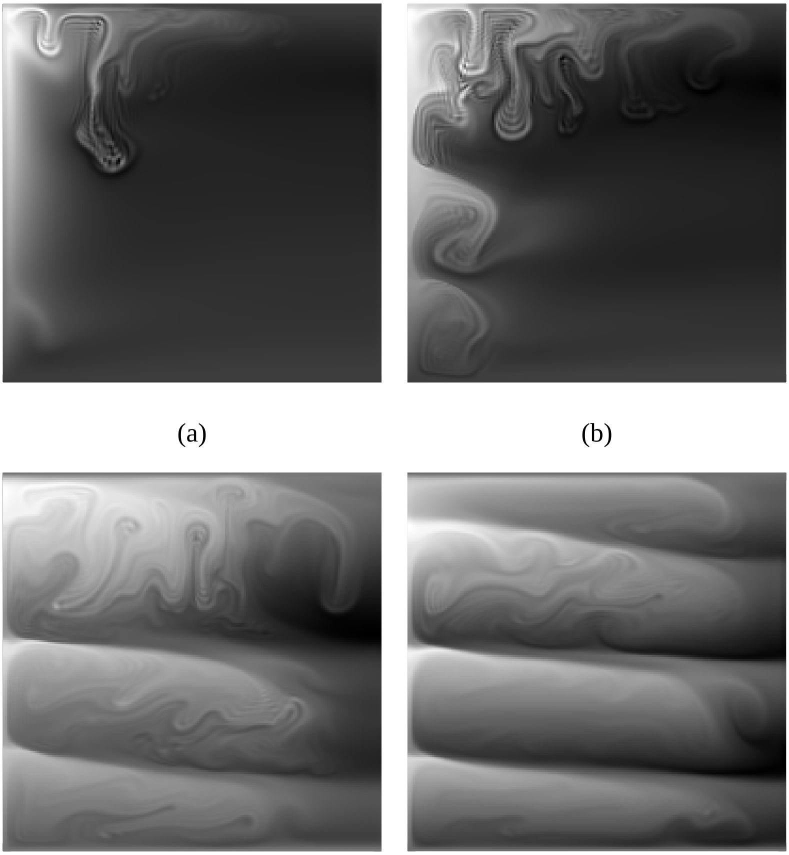

(a) (b)

(c) (d)

Figure 4.2: *Development of layers in the doubly stratified case for* $Ra_\eta = 5\ 10^4, R = 5$. *Shown is the salinity distribution minus the initial salinity distribution: white corresponds to relatively salty liquid, black corresponds with relatively fresh liquid. (a):* $t = 0.005$*, (b):* $t = 0.01$*, (c):* $t = 0.05$*, (d):* $t = 0.1$.

the flow field are shown as contour plots of the streamfunction. More details of the flow can be observed in the Figs. 4.2, where the difference of the actual salinity field and the initial salinity distribution are presented as a grey-shade plot. The latter salinity fields are also shown in the Figs. 4.3 at corresponding times for the singly stratified case with $R_\rho = \infty$, $R = 5$.

In both singly and doubly stratified cases, layers develop within about 10 hours. However,

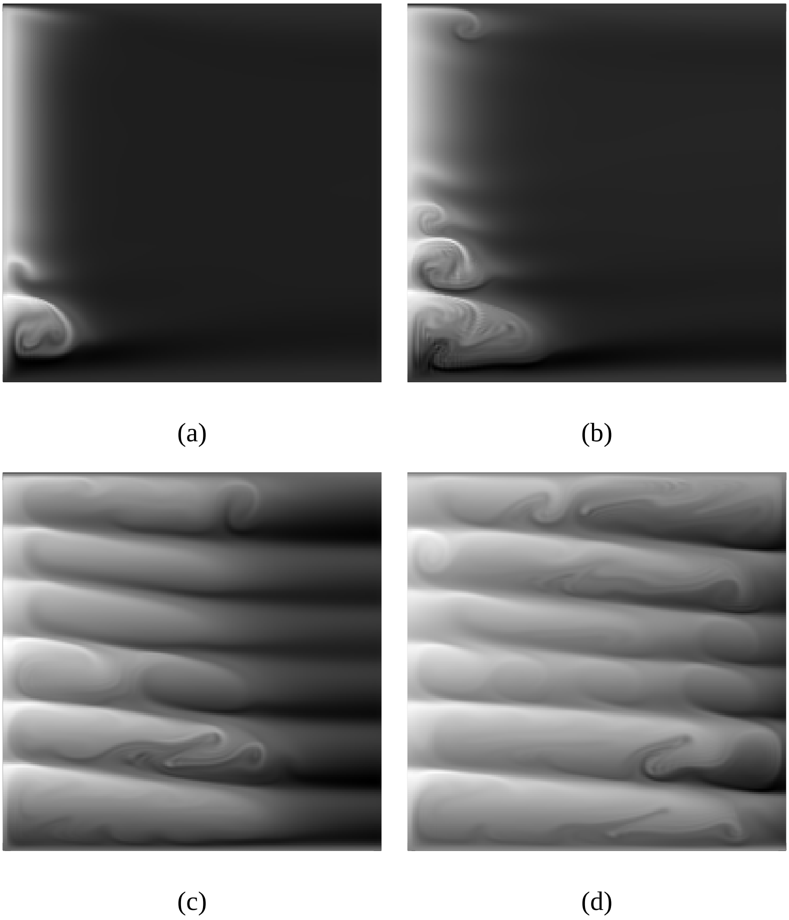
(a) (b)

(c) (d)

Figure 4.3: *As Figure 4.2, but now for the singly stratified case at the same instants.*

the initial development and the final scales of the layers are strikingly different for both cases. Whereas in the singly stratified case about 6 layers develop (Fig. 4.3c-d), the number of layers is smaller in the doubly stratified case. About 4 layers are observed (Fig. 4.2c-d), of which only the lower three are well-developed. For these three layers, the thickness increases upwards contrary to the layers in Fig. 4.3c-d whose thickness decreases upwards. The layer size is larger than that of the corresponding singly stratified flow, which is in accordance with the observations of *Jeevaraj and Imberger* [1991].

Plots of the horizontal velocity, temperature, salinity and density along a section through the

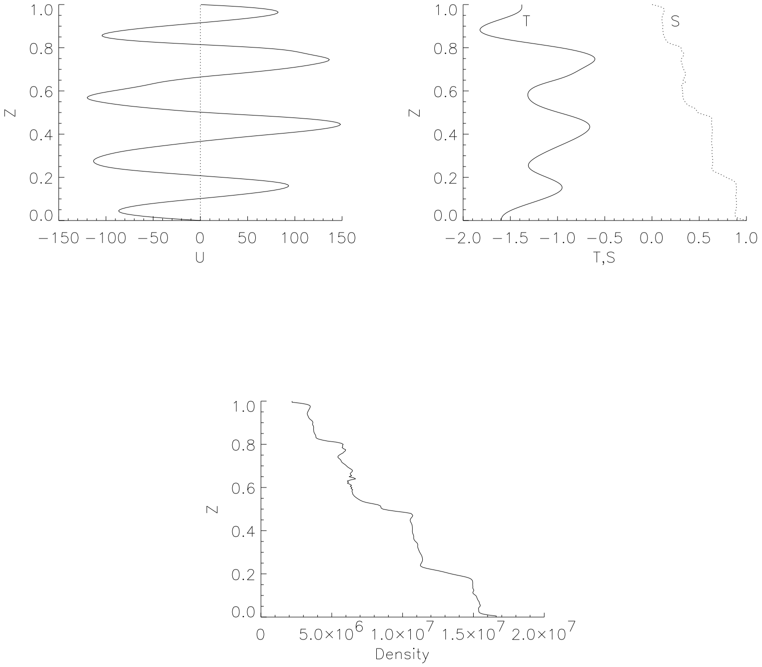

Figure 4.4: *Horizontal velocity U,temperature T, salinity S and density ρ for the doubly stratified case at $t = 0.1$ along a section through the middle of the container.*

middle of the container ($x = 0.5$) are shown at $t = 0.1$ for the doubly stratified case in the Figs. 4.4. The horizontal velocities have a slightly smaller amplitude in the lower layer and nearly equal magnitude in the next two layers (Fig. 4.4a). Within each layer, the temperature is stably stratified whereas the salinity is well mixed (Fig. 4.4b). Over the interfaces separating the layers, the temperature is unstably stratified, similar to the distributions found in the singly stratified case (Chapter 3). The salinity profile in Fig. 4.4b also reveals the increase of layer thickness with height. The latter effect can easily be explained, since the layer thickness depends on the lateral temperature difference which varies with liquid height in the doubly stratified case. The density distribution is generally stable both in the layers and the interfaces between them (Fig. 4.4c).

A main difference between the flows in the Figs. 4.2 and the Figs. 4.3 is the convective activity in the upper layer which is much stronger for the doubly stratified case (compare Fig. 4.2a-b with Fig. 4.3a-b). Clear signatures of this strong convection are also shown in Fig. 4.1b-c. These features were also noted by *Schladow et al.* [1992] in their doubly stratified experiments. For instance, their Fig. 5a shows the same plume-like structures as those in the Figs. 4.2. This strong convection is absent in the singly stratified case (Figs. 4.3). The existence of flow with significant convective activity suggests that the simulated flow would fit into either class II or III of *Schladow et al.* [1992], but since the temperature is stably stratified within the layers (Fig. 4.4b), class II seems appropriate.

Although we prescribe no constant heat flux at the left wall, as in *Schladow et al.* [1992], we consider the magnitude of the lateral stability parameter R_l by computing the range of the heat flux in the simulation. The parameter R_l, as given in (4.3), can be expressed into our model parameters by nondimensionalization and using the values of the vertically averaged horizontal heat flux $\overline{Nu}(x,t)$ (defined in Chapter 3) at the heated sidewall ($x = 0$). This gives

$$R_l = \frac{\mathcal{H}_d \overline{N}u(0,t)}{R(1 - {R_\rho}^{-1})} \tag{4.9}$$

where $\mathcal{H}_d$ is the diffusive heat flux in absence of any flow (see Chapter 3). In the simulation above, with a constant temperature at the left sidewall, the heat transport varies significantly along the heated wall because Ra_η varies vertically. However, the value of R_l based on the averaged heat flux is in the range $[4, 40]$. For a typical case, with $\mathcal{H}_d\overline{N}u = 60$ $(t = 0.1)$, $R = 15$ and $R_\rho = 1.5$, the stability parameter equals $R_l = 12$. Hence, a comparison with the experimental results in table 2 of *Schladow et al.* [1992] confirms that, considering the values of R_ρ and R_l, even for this large range of R_l the simulation undoubtly falls into Class II. For this regime, self-propagation is therefore possible, and we consider its existence in a slightly larger aspect ratio container.

4.3.2 The analysis of self propagation

For the same values of the parameters as in the previous simulation, the evolution of the intrusions is investigated for a wide tank with $A = 4$. The numerical resolution in the simulations was chosen to be 401 * 101. This choice was determined by a desire to just resolve the salinity boundary layers but keep the computation manageable in terms of CPU time.

In these simulations, the thermal forcing at the left sidewall is maintained until $t = 0.05$. We present the flow development after $t = 0.05$ for three different cases in the Figs. 4.5. In the Figs. 4.5a, the development of the flow has been plotted for the case that the thermal forcing is

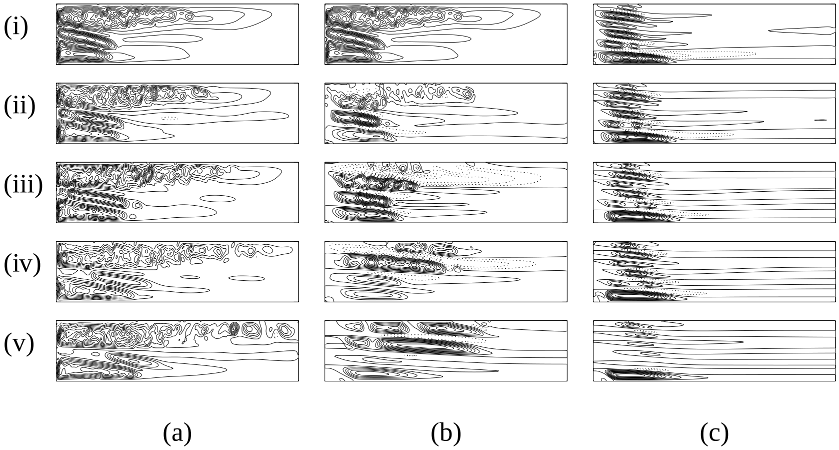

Figure 4.5: *Contour plots of the stream function from* $t = 0.05$ *for both doubly stratified and singly stratified cases, for* $A = 4$*. (a): doubly stratified, thermal forcing continued, (b): doubly stratified, no thermal forcing, (c): singly stratified, no thermal forcing. Time intervals:* $(i) : t = 0.05, (ii) : t = 0.06, (iii) : t = 0.07, (iv) : t = 0.09, (v) : t = 0.1.$

continued after $t = 0.05$. The layers continue to develop towards the right wall and the region of strong convective activity extends to nearly half the container. If for this case, the thermal forcing is stopped at $t = 0.05$, then still the layers continue to propagate towards the right (Fig. 4.5b). The latter is a clear signature of self-propagation and will be analysed below. For comparison, the evolution for the singly stratified case, for which the forcing is turned off at $t = 0.05$ is also shown (Fig. 4.5c). Self-propagation does not occur and the layers disappear due to viscous dissipation.

The flow in the Figs. 4.5b is considered in more detail by vertical sections of the temperature, salinity and density at different horizontal positions within the layer. At $t = 0.05$, it is observed that heat and salt have been transported upwards within the upper layer in Fig. 4.5b, such that the temperature distribution is stabilizing (Fig. 4.6a) and the salinity distribution (Fig. 4.6b) is slightly destabilizing. However, the liquid is still stably stratified (Fig. 4.6c) apart from some small intervals where it is unstably stratified. Hence, the main source of convective activity can be attributed to salt-fingering, with localized areas where direct buoyancy induced convection occurs. As the forcing is turned off, the stabilizing influence of the temperature distribution decreases since thermal diffusion is fast (Fig. 4.6d). The salt transport to the top of the upper layer decreases and consequently maxima in salinity appear within the upper layer (clearest seen

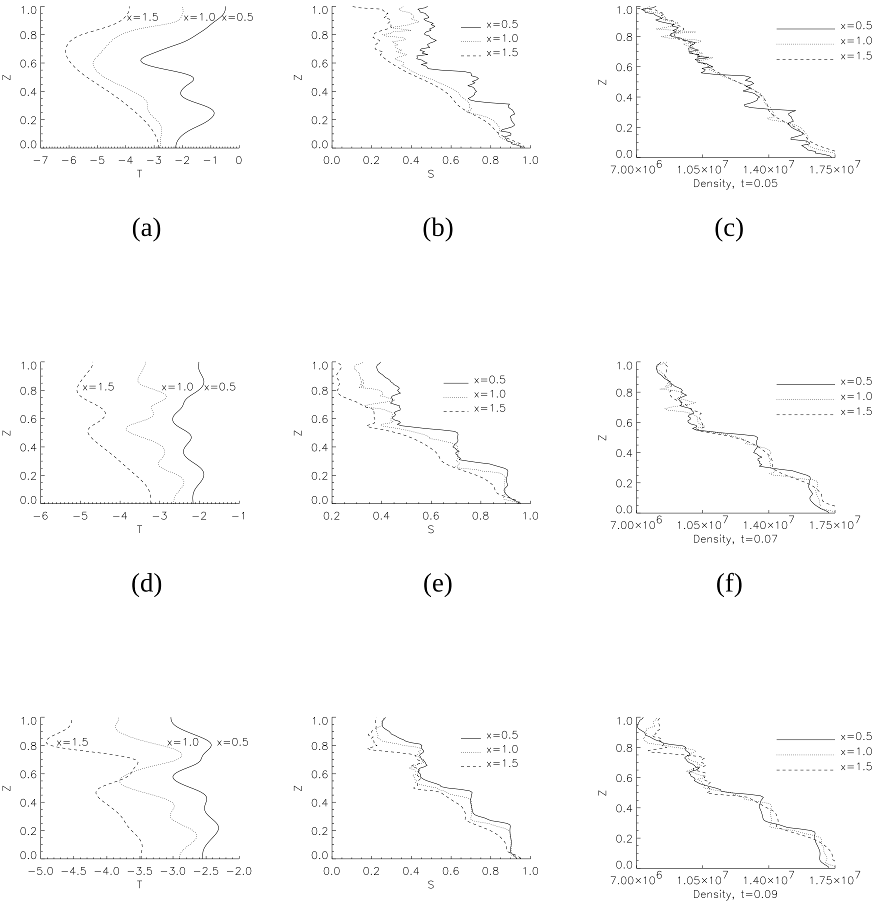

(a) (b) (c)

(d) (e) (f)

(g) (h) (i)

Figure 4.6: *Vertical sections of temperature, salinity and density for the doubly stratified ($A = 4$) case at several instants; (a - c): $t = 0.05$, (d - f): $t = 0.07$, (g - i): $t = 0.09$. The horizontal scales for T and S differ in order to magnify the differences between the profiles in a plot.*

in Fig. 4.6e at $x = 1.0$). The influence on the density is such that the distribution remains stably stratified (Fig. 4.6f). At $t = 0.09$, the temperature profiles have reversed near the top of the

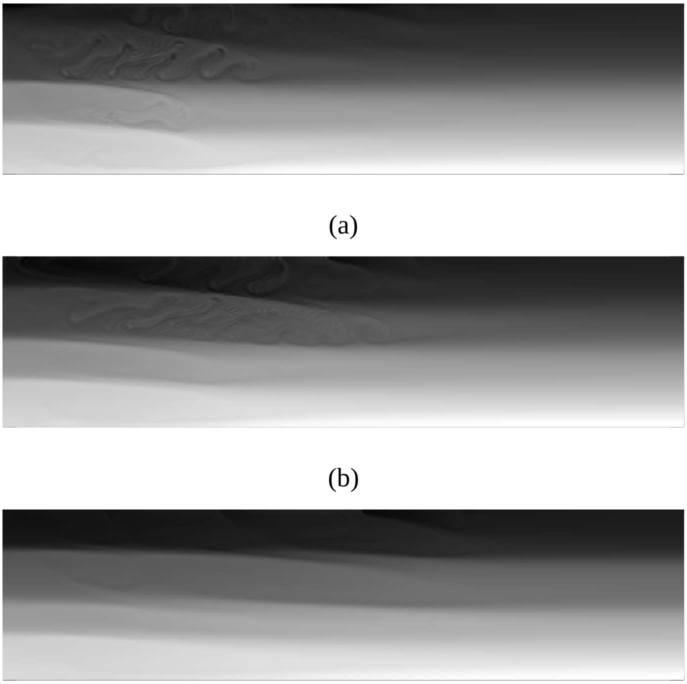

(a)

(b)

(c)

Figure 4.7: *Density grey-shade plots for the doubly stratified case after thermal forcing has been turned off. (a):* $t = 0.07$ *(panel (iii) in Fig. 4.5), (b):* $t = 0.09$ *(panel (iv) in Fig. 4.5), (c):* $t = 0.15$ *(panel (v) in Fig. 4.5).*

upper layer (Fig. 4.6g) and a maximum in the temperature appears near $z = 0.8$ at $x = 0.5$ and appears at $z = 0.7$ at $x = 1.5$. A similar shift in the maxima of the salinity profile in the upper layer is observed (Fig. 4.6h) with a larger salinity at $x = 0.5$ than at $x = 1.5$. Consequently, the isopycnals slope towards the horizontal, as can be seen in Fig. 4.6i. This slope is clearly visible in a gray-shade plot of the density at the corresponding times ($t = 0.07$ and $t = 0.09$) shown in Fig. 4.7a and Fig. 4.7b, respectively. At a later time ($t = 0.15$), this slope decreases due to adjustment (Fig. 4.7c). The corresponding density plots for the singly stratified case (Fig. 4.8a-c) show a much smaller slope and hardly any change with time after the forcing has been turned off.

The horizontal velocity at $x = 0.5$ (Fig. 4.9a) and $x = 1.5$ (Fig. 4.9b) for two different times

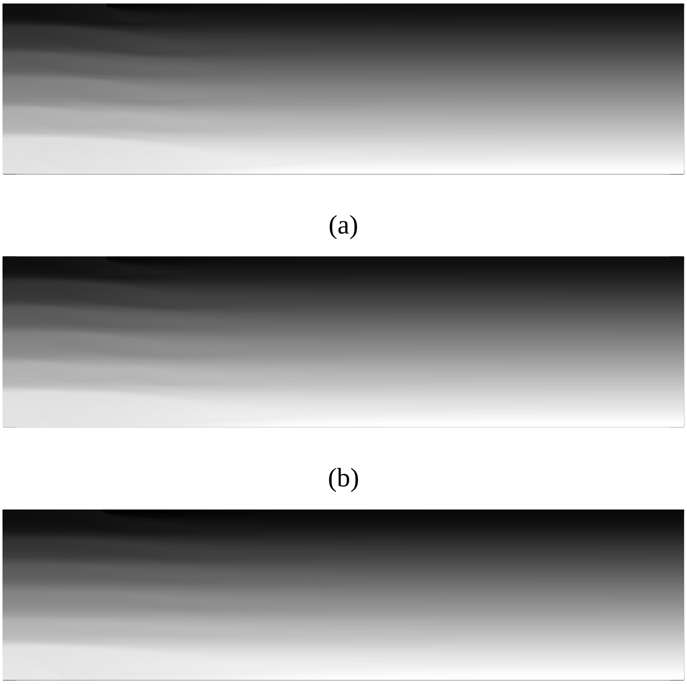

(a)

(b)

(c)

Figure 4.8: *As Figure 4.7, but now for the singly stratified case at the same instants.*

during the evolution of the flow in Fig. 4.5b are shown in Figs. 4.9. In Fig. 4.9a, the magnitude of the horizontal velocity at about $z = 0.8$ increases in time, although the forcing is off. The same is seen in Fig. 4.9b, but the maximum occurs at smaller values of z ($z = 0.7$). The increase in velocity is also observed in the development of the average kinetic energy $< E_k >$ of the flow which is plotted in Fig. 4.10a. In the unforced doubly stratified flow in Fig. 4.5b, $< E_k >$ initially increases up to $t = 0.08$ and then decreases. For comparison, the evolution of $< E_k >$ is also shown (Fig. 4.10b) for the singly stratified flow in Fig. 4.5c. As is expected, $< E_k >$ decreases immediately as the forcing is turned off due to viscous dissipation.

The flow shown in Fig. 4.5b and its characteristics presented above are a clear example of self-propagation. The main question is how to describe the physics of this phenomenon and identify its energy sources. *Schladow et al.* [1992] suggest that local instabilities induced by liquid blocking due to endwall effects [*Turner*, 1973] are the main energy source of self-propagation.

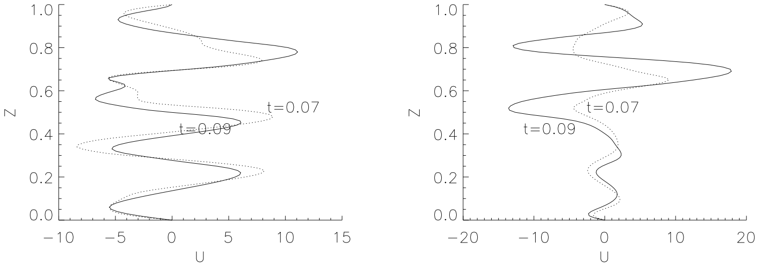

(a) (b)

Figure 4.9: *Vertical section of the horizontal velocity at $x = 0.5$ (a) and $x = 1.5$ (b) for two different times after shut-off of thermal forcing (doubly stratified case).*

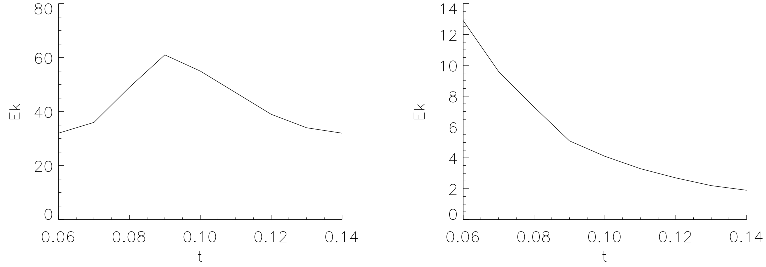

(a) (b)

Figure 4.10: *Change in $< E_k >$ with time when thermal forcing has been shut off; (a): doubly stratified case (Fig. 4.5b), (b): singly stratified case (Fig. 4.5c).*

Characteristic of liquid blocking is a weak upward and downward flow just ahead of the intrusion. This flow disturbs the stabilizing salinity distribution but leaves the unstable temperature distribution merely intact due to the much larger thermal diffusivity. Hence, the value of R_ρ is

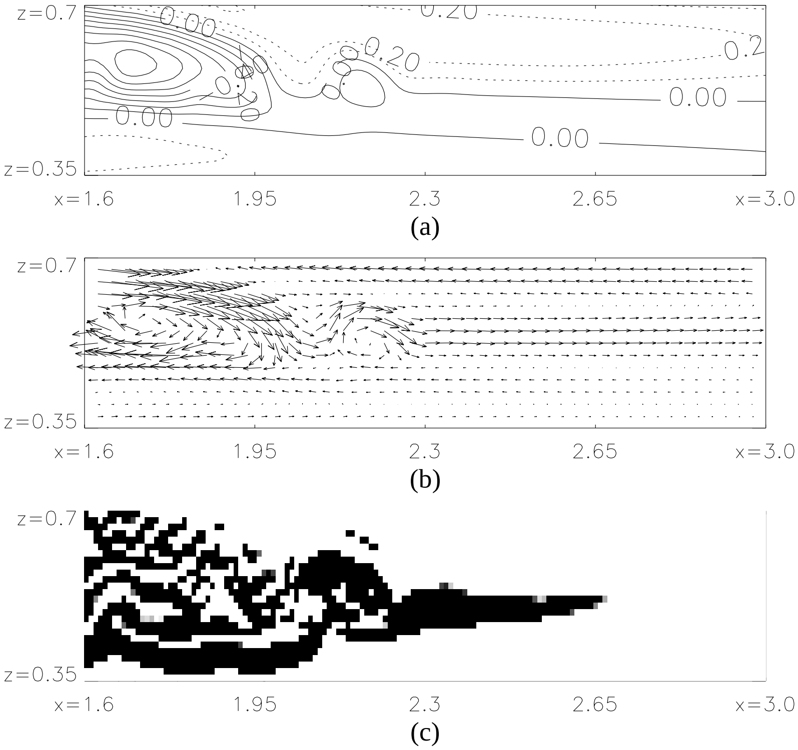

Figure 4.11: *Detail of the intrusion front in Figure 4.5b (panel iv) for the doubly stratified case; (a): ψ near intrusion front, (b) velocities (for clarity a reduced number of vectors is shown), (c) R_ρ, black regions correspond to $R_\rho < 1$.*

locally reduced and local instabilities provide the energy for the intrusion to grow.

To test this hypothesis, the flow just ahead of the intrusions is considered during the self-propagation stage. The streamfunction field (Fig. 4.11a), a vector plot of the velocity (Fig. 4.11b) and the R_ρ field (Fig. 4.11c) are plotted just ahead of the propagating intrusion (detail of figure 4.5b*(iv)*). Note the different vertical scale in this plot, compared to the ones in Fig. 4.5b. Although there is a weak buoyancy driven flow ahead of the intrusions, there are no signatures of a blocked flow ahead of the intrusion (Fig. 4.11a-b). The background flow is nearly parallel and returns only in a thin boundary layer near the right wall. The black regions in Fig. 4.11b indicate values of $R_\rho < 1$ and show that the flow ahead of the intrusion is statically unstable. This is caused by an unstable thermal stratification and a strongly reduced salinity gradient.

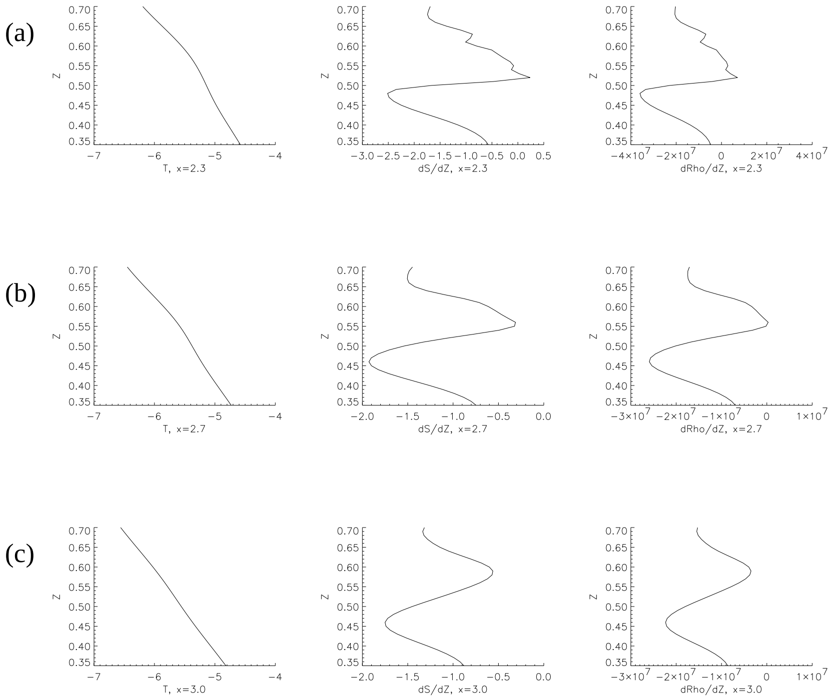

Figure 4.12: *Vertical sections of temperature, vertical salinity gradient and vertical density gradient ahead of the intrusion front; (a)* $x = 2.3$*, (b)* $x = 2.65$*, (c)* $x = 3.0$.

The Figs. 4.12a-c show that the temperature field farther ahead of an intrusion is indeed undisturbed, but that the salinity field is affected by the weak background flow. The vertical scale over which the unstable stratification occurs is sufficiently large (about 0.1 units) to cause a buoyancy driven direct instability. Even if the stratification is stable, double-diffusive instabilities may cause growth of perturbations ahead of the intrusions.

However, the origin of the weak background flow is the gravitational adjustment associated with the sloping isopycnals and is not related to any blocking. This can be seen in the Figs. 4.5b (panels (iii) and (iv)), where the flow in the upper layer is to the right along the first interface, just as one would expect from an adjustment. Moreover, one can observe the adjustment in the Figs. 4.7a-c. Hence, local instabilities may provide an energy source of the self-propagation of the intrusions, but only in the presence of such a weak background flow, induced by adjustment.

4.4 Conclusions

The results from the two-dimensional numerical simulations of the evolution of intrusions into a stratified liquid show many features also observed in experiments. This *a postiori* justifies the use of the two-dimensional model; the dominant physics of layer formation and self-propagation is already captured by such a model.

The analysis of the flow details lead to the following physical picture of self-propagation in doubly stratified systems. If the vertical stability ratio R_ρ is small enough, the upward transport of salt along the heated wall is able to cause intense convection in the upper layer through salt-fingering (or direct instabilities). This cannot be accomplished in a singly stratified liquid, because (i) the initial temperature distribution does not destabilize the flow and (ii) the layer thickness does not increase but decreases upwards. Hence, most of the salt is transported by the lowest layers in this case, contrary to that in the doubly stratified case, where most salt is transported by the most upper layer.

As the lateral temperature forcing is turned off, a horizontal salt gradient results because near the heated wall more salt has accumulated than far from that wall. Contrary to the temperature distribution, the salinity distribution recovers slowly. Consequently, a relatively strong slope in the isopycnals results when the sidewall heating is turned off. During the unforced evolution, the liquid adjusts itself and the heavier liquid moves to its neutral level. This sets up a background flow and provides a simple source of energy of self-propagation. Due to the presence of the background flow the salinity field is modified just ahead of the intrusion whereas the temperature field is hardly modified because of relatively large thermal diffusion. Local instabilities, which may be direct or diffusively driven, may provide kinetic energy to the intrusion.

Hence, the heart of the physics of the self-propagation is the slope of the isopycnals set-up by the differential salt transport in the upper layer due to salt fingering. This slope provides itself an energy source due to adjustment and provides the background flow such that local instabilities may occur. When the stability ratio increases, both sources of energy are much weaker since the slope in the isopycnals is much smaller and no background flow (and consequently no local instabilities) occurs. This description therefore explains why self-propagation does not occur in singly stratified systems.

References

Jacobs, S. S., Huppert, H. E., Holdsworth, G., Drewry, D. J., Thermohaline steps induced by melting of the Erebus Glacier tongue, *J. Geophys. Res.*, **86**, 6547–6555 (1981).

Jeevaraj, C., Imberger, J., Experimental study of double-diffusive instability in sidewall heating, *J. Fluid Mech.*, **222**, 565–586 (1991).

Kranenborg, E.J, Dijkstra, H.A., The evolution of double-diffusive intrusions into a stably stratified liquid. I: A study of the layer merging process. *Int. J. Heat Mass Transfer, submitted*, (1996).

Schladow, S. G., Thomas, E., Koseff, J. R., The dynamics of intrusions into a thermohaline stratification, *J. Fluid Mech.*, **236**, 127–165 (1992).

Schmitt, R.W., Double diffusion in oceanography, *Ann. Rev. Fluid Mech.*, **26**, 255-285 (1994).

Turner, J. S., *Buoyancy effects in fluids*, Cambridge (1973).

Wirtz, R. A., Briggs, D. G., Chen, C. F., Physical and numerical experiments on layered convection in a density–stratified fluid, *Geophysical Fluid Dynamics* , **3**, 265–288 (1972).

Chapter 5

Double-diffusive layer formation near a cooled liquid-solid boundary

As an idealization of convection near an ice boundary, flows in both salt-stratified and non-stratified fluids generated by a cooled slab of solid material are considered through direct numerical simulation. When the fluid far from the slab is homogeneous, significant convection occurs below the ice and apart from a small boundary layer, hardly any flow appears next to the ice. In contrast, when the background liquid is stratified through a constant salt gradient, a layered flow appears next to the ice if the thickness of the slab is large enough. The latter flows are of double diffusive origin and have a significant effect on the transport of heat and salt near the ice.

5.1 Introduction

Step structures in vertical profiles of salinity and temperature, for example as observed in the ocean, are characteristic signatures of double diffusive processes, i.e. convection in a stably stratified fluid induced by the different molecular diffusivities of two components [*Schmitt*, 1994]. A typical situation of layered flow occurs in a salt stratified liquid over which a horizontal temperature difference is applied. These types of flow have been studied in the laboratory for idealized situations, for example in rectangular containers [*Chen et al.*, 1971; *Tanny and Tsinober*, 1988; *Jeevaraj and Imberger*, 1991]. Theoretical work has focussed on the critical conditions for double diffusive instabilities to occur [*Thangam et al.*, 1981] and their subsequent evolution to well-developed layers (*Kerr* [1990] and Chapter 3).

In case the initial temperature T_i is constant with height and the initial salinity S_i a linear function of height, layers with a characteristic scale

$$\eta = \frac{\alpha \Delta T}{\phi_0} \tag{5.1}$$

appear when a Rayleigh number Ra_η, based on η, is large enough. In equation (5.1), ϕ_0 is the background vertical component of the density gradient ($-\beta \frac{\partial S_i}{\partial z}$) and ΔT the horizontal temperature difference. The parameters α and β are the expansion coefficients in the linear equation of state relating changes in the temperature and salinity to those in the density, respectively. The initial scale of the layers may be substantially smaller, but subsequent merging of layers leads eventually to a layer thickness with scale η. An analysis of this layer merging process is given in Chapter 3 ([*Kranenborg and Dijkstra*, 1996]).

When, in addition to a stable salinity gradient, a destabilizing temperature gradient is initially present, and if the stability ratio

$$R_\rho = \frac{\beta \frac{\partial S_i}{\partial z}}{\alpha \frac{\partial T_i}{\partial z}} \tag{5.2}$$

is small enough, layers may propagate even when the lateral cooling or heating has been turned off. This so-called self-propagation has been experimentally observed by *Schladow et al.* [1992] and its physics was analysed through direct numerical simulation in Chapter 4.

A typical situation where one expects these layered flows in the ocean is near ice boundaries, for example slabs of sea-ice or icebergs, which provide the lateral cooling of the stably stratified liquid. Motivated by the fact that these flows significantly influence the melting of the ice, *Huppert and Turner* [1980]; *Huppert and Josberger* [1980] performed the first laboratory experiments on double diffusive flows near ice bodies. It was shown that, when a block of ice is put into a liquid which is stably stratified through a constant salt gradient, the layer thickness also scales with η. In this case, the lateral temperature difference ΔT must be taken as the difference between the temperature at the ice boundary (the freezing point at the far field salinity) and that of the liquid far from the ice. The layered flows were shown to be of double diffusive origin. The melting of an ice wall in a cavity filled with water of uniform salinity [*Josberger and Martin*, 1981] is completely different. In this case and at oceanic ambient salinities, the transport of meltwater relatively far from the wall is downward. However, next to the ice wall the liquid may become buoyant, because the dilution effect due to the melting of the ice may be dominant over the cooling effect. In any case, no layered flow appears.

The double diffusive flows considered experimentally in *Huppert and Josberger* [1980], using lower ambient temperatures and smaller salinity gradients than those in *Huppert and Turner* [1980], showed a similar layer formation (with the same layer scale). In polar areas, it is common that the background salinity $S_i(z)$ and temperature $T_i(z)$ decrease upwards in the upper layers of the ocean. Based on the above mentioned laboratory experiments, one would expect layer formation near ice boundaries. These layered structures have indeed been observed, for example by *Horne* [1985] near a $150\ m$ ice face in the South Cape Fiord in the Arctic.

One might question how thick such an ice body should be for layered flows to appear. For example, can these flows develop near relatively thin sheets of sea-ice? Another issue of interest is how the transport of heat and salt is altered by these double diffusive flows, in comparison with direct buoyancy driven flows near the ice. Both questions are addressed in this chapter, where we study flows near (an idealization of) an ice slab through a direct numerical simulation in a two-dimensional set-up. It is found that the thickness of the slab has to be larger than the internal length scale η for layered flows to appear. The heat and mass transport of the buoyancy driven flows is strongly modified when layers are present, for example the vertical salt and heat transport next to the ice is strongly reduced.

5.2 Model formulation and numerical implementation

The melting of a vertical wall of ice in a saline fluid is a complex process [*Carey and Gebhart*, 1982; *Josberger and Martin*, 1981; *Huppert and Turner*, 1978, 1980]. In a liquid of uniform salinity initially a laminar flow is present where the saline buoyancy force due to melting is confined to a very small boundary layer, but cooling of the bulk also occurs further from the ice boundary. The flow quickly becomes turbulent; due to entrainment of salty water and turbulent mixing, the final direction of the flow depends on both the lateral ice/bulk temperature difference and the salt concentration. Measurements by thermoresistors near the ice/water interface by *Huppert and Turner* [1980] have shown that the ice temperature at the interface is approximately $0^{\cdot}C$. This result indicates that the turbulent boundary layer approximately prescribes an effective temperature boundary condition of $0^{\cdot}C$ for the bulk of the liquid, which leads to a downward flow further from the ice boundary [*Huppert and Turner*, 1980]. Hence, the presence of a stable background salinity stratification will result in the formation of double-diffusive layered structures similar to those generated near cooled vertical solid plates. Since the layer scales for ice cooling experiments and those for metal cylinder cooling experiments are of the same order [*Huppert and Turner*, 1980], and meltwater is largely entrained into the convective layers [*Huppert and Turner*, 1978], we conclude that meltwater has limited influence on the flow development in the liquid for the cases considered. Therefore, in the present numerical study, an ice plate is represented by a cooled slab of solid material.

The slab (length $2H$, thickness D, thermal diffusivity κ_Θ and temperature Θ) is cooled from

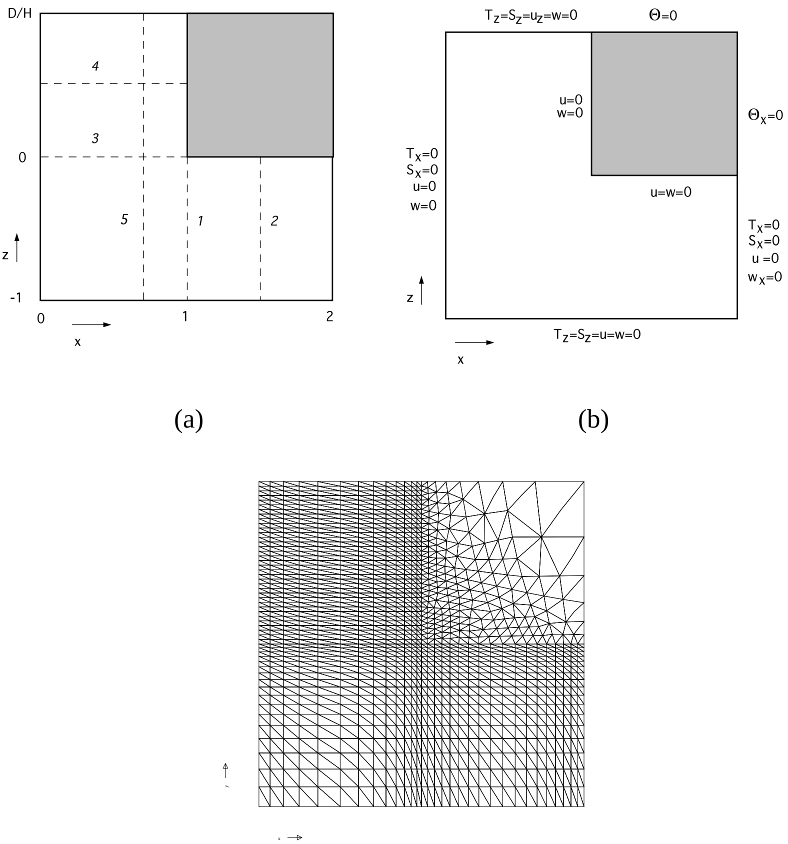

(a) (b)

(c)

Figure 5.1: *(a): Geometrical set-up of the problem. (b): Summary of the boundary conditions prescribed. (c): Typical finite element mesh as used for the thick slab simulation.*

above and partially covers a water column in a rectangular container (Fig. 5.1a) in which a stable initial salinity gradient is present (thermal diffusivity κ_T, diffusivity of salt κ_S, kinematic viscosity ν, temperature T^* and salinity S^*). Due to symmetry, only half of the container and half of the slab are presented in Fig. 5.1a; the right boundary in this figure is an axis of symmetry.

A linear equation of state with respect to a constant reference temperature T_0 and salinity S_0 is assumed, i.e. $\rho = \rho_0(1 - \alpha(T^* - T_0) + \beta(S^* - S_0))$. The governing equations are non-dimensionalized using scales H, H^2/κ_T and κ_T/H for length, time and velocity, respectively. The temperature and salinity are non-dimensionalized by $T = (T^* - T_0)/\Delta T$, $\Theta = (\Theta^* - \Theta_0)/\Delta T$ and $S = (S^* - S_0)/\Delta S$, where ΔS and ΔT are typical vertical salinity and horizontal temperature differences, respectively. With this scaling, the container wall is located at $x = 0$, the vertical solid-liquid boundary at $x = 1$, and the symmetry axis at $x = 2$. The bottom of the container is located at $z = -1$, the horizontal solid-liquid boundary at $z = 0$, and both the upper slab boundary and the top of the liquid at $z = D/H$. These boundaries are indicated in Fig. 1a and along the indicated sections, profiles and transport properties are presented below.

In primitive variables, the dimensionless governing equations become

$$Pr^{-1}(\frac{\partial \vec{u}}{\partial t} + (\vec{u}\cdot\nabla)\vec{u}) = -\nabla p + \nabla^2\vec{u} + \hat{\mathbf{z}}Ra_T(T - RS), \tag{5.3a}$$

$$\nabla\cdot\vec{u} = 0, \tag{5.3b}$$

$$\frac{\partial T}{\partial t} + (\vec{u}\cdot\nabla)T = \nabla^2 T, \tag{5.3c}$$

$$\frac{\partial S}{\partial t} + (\vec{u}\cdot\nabla)S = Le^{-1}\nabla^2 S, \tag{5.3d}$$

where $\hat{\mathbf{z}}$ is the unit vector in vertical direction. The heat transfer in the solid is modelled by the heat equation

$$\frac{\partial \Theta}{\partial t} = \lambda\nabla^2\Theta. \tag{5.4}$$

At the fixed solid-liquid boundary continuity of temperature and heat flux is expressed as

$$T = \Theta,\ \nabla T\cdot\vec{n} = \lambda\nabla\Theta\cdot\vec{n}. \tag{5.5}$$

where $\vec{n}$ is the normal on the boundary.

Along the container walls (left and lower boundary) no-slip conditions and no-flux conditions for both heat and salt are prescribed. At the symmetry axis, free-slip conditions and no-flux conditions for heat and salinity apply. The top of the slab is cooled through a constant temperature Θ_0^*. At the solid-liquid interface no-slip conditions, no-flux salinity conditions and conditions (5.5) are prescribed. Finally, at the upper boundary of the liquid free-slip conditions and no-flux conditions for temperature and salinity are prescribed. The prescribed boundary conditions of the problem are summarized in Fig. 5.1b. Boundary conditions (5.5) appear naturally at the solid-liquid interface as a result of the finite-element discretisation applied (see below).

The dimensionless parameters which appear in equations (5.3) to (5.5) are the Rayleigh number Ra_T, the buoyancy ratio R, the Prandtl number Pr, the Lewis number Le and the diffusivity ratio λ, defined as

$$Ra_T = \frac{g\alpha\Delta T H^3}{\nu\kappa_T},\ R = \frac{\beta\Delta S}{\alpha\Delta T},\ Pr = \frac{\nu}{\kappa_T},\ Le = \frac{\kappa_T}{\kappa_S},\ \lambda = \frac{\kappa_\Theta}{\kappa_T}. \tag{5.6}$$

Using the layer thickness scale η, a Rayleigh number Ra_η, based on η, can be expressed into model parameters as

$$R = H/\eta; Ra_\eta = Ra_T/R^3. \tag{5.7}$$

A standard Galerkin finite element method [*Segal*, 1994], using quadratic elements for the velocity, temperature and salinity, and linear elements for the pressure, was applied to equations (5.3-5.5). This finite element discretization is second order accurate in space. A penalty formulation is used to eliminate the pressure unknowns. The nonlinear terms are linearized using the standard Newton-Raphson method and the resulting sets of linear equations are solved using a direct (profile) solver.

The spatial resolution chosen depends on the thickness of the slab and the value of Ra_η. The lowest resolution is used with a relatively thin slab and uses 31 elements in the horizontal and 21 elements in the vertical (which amounts to 9577 unknowns), while the highest resolution (for a thick slab) corresponds to 64 elements in the horizontal and 75 elements in the vertical (49832 unknowns). An example of a typical mesh in the latter case is shown in Fig. 5.1c showing an increased resolution near the solid-liquid boundary. Time integration is performed using the implicit Crank-Nicolson method except for the first two iterations where the implicit Euler method is used. Both the resolution and the time step (dimensionless values range between 10^{-5} and 10^{-4}) were chosen such that halving grid space and time step gave similar results during the initial stages of evolution of the flow for the typical case ’A’ below.

5.3 Flow development

In the results below, the standard values of the parameters are shown in Table 5.1. This reference model can be regarded as an extension of one of the cavity models with aspect ratio $A = 1$ as investigated in Chapter 3. To analyse specific double diffusive signatures the four different cases as shown in Table 5.2 are considered. Differences appear through the thickness of the slab and the presence or absence of a stable initial stratification.

5.3.1 Stratified background

Case ’A’ represents a stratified liquid which is cooled by a relatively thick plate of thickness $D = H$. From the substitution of $H = D$ in $R = H/\eta$ it follows that $D/\eta = R = 2.5$, i.e.

$H = 0.2\ (m)$
$L = 0.2\ (m)$
$\kappa_S = 1\ 10^{-9}\ (m^2 s^{-1})$
$\kappa_T = 1\ 10^{-7}\ (m^2 s^{-1})$
$\kappa_\Theta = 1\ 10^{-6}\ (m^2 s^{-1})$
$\nu = 7\ 10^{-7}\ (m^2 s^{-1})$

$Ra_\eta = 5\ 10^4$
$R = 2.5$
$Pr = 6.7$
$Le = 101$
$\lambda = 10$

Table 5.1: Standard dimensionless and dimensional parameters in this study.

Situation	Plate thickness D	$S(x, z; t = 0)$
A (reference)	$D = H$	$S = 1 - z$
B	$D = 0.1H$	$S = 1 - z$
C	$D = H$	$S = 1$
D	$D = 0.1H$	$S = 1$

Table 5.2: Summary of the different cases considered.

the thickness of the plate is larger than the internal layer scale. The initial conditions consist of a homogeneous temperature and a linear salinity distribution, i.e.

$$t = 0 : T(x, z) = 1\ ;\ S(x, z) = 1 - z\ ;\ \Theta(x, z) = 1. \tag{5.8}$$

The time-dependent evolution up to $t = 5.5\ 10^{-2}$ (in dimensional units $t^* = 2.2\ 10^4[s]$) is shown in Fig. 5.2 through contour plots of the temperature and salinity and a vector plot of the velocity field at four different times during this evolution. Initially, a diffusive thermal boundary layer forms near the boundaries of the slab (Fig. 5.2a). A strong downward flow is induced next to the wall transporting fresh water downwards which considerably reduces the salinity near the ice. This boundary layer flow becomes unstable through double diffusive instabilities and layers start to form (Fig. 5.2b and Fig. 5.2c). Convection is stronger at the top because the horizontal temperature difference – and consequently Ra_η – is largest.

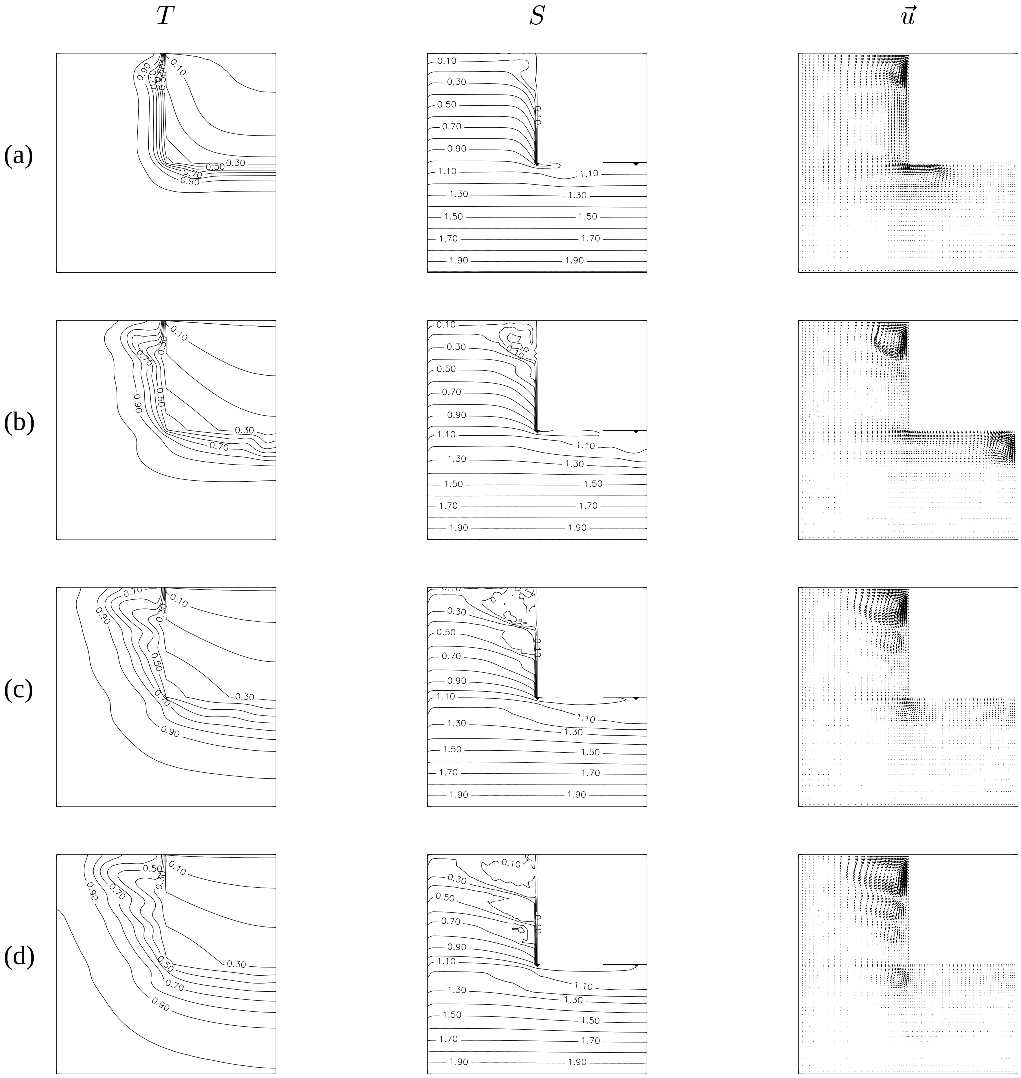

Figure 5.2: *Development in time of the temperature, salinity and velocity distribution, case 'A'; (a):* $t = 5\ 10^{-3}$ *(*$2.0\ 10^{3}$ *s); (b):* $t = 1.5\ 10^{-2}$ *(*$6.0\ 10^{3}$ *s); (c):* $t = 3.5\ 10^{-2}$ *(*$1.4\ 10^{4}$ *s); (d):* $t = 5.5\ 10^{-2}$ *(*$2.2\ 10^{4}$ *s).*

Near the corner of the slab ($x = 1, z = 0$), the isotherms of the boundary layer are necessarily curved and hence a horizontal density gradient is set-up. Because the density is larger just below the horizontal wall of the plate, the convection cell near the corner has a clockwise rotation (Fig. 5.2a). Warmer liquid is transported under the ice, maintaining the horizontal gradient and the cell propagates to the right (Fig. 5.2b). Since this flow is caused by the asymmetry in the forcing, due to the geometry, we will refer to it as a geometrically induced flow.

Although the latter (forced) convection is present below the ice slab, layer formation occurs along the complete vertical boundary of the slab and is much more intense. At the time when the flow has become quasi-stationary (Fig. 5.2d), the distribution of the density field (Fig. 5.3a) along section 5 (Fig. 5.1a) shows the characteristic step structures associated with the layers. Near $z = 0$, the density gradient changes substantially and the liquid slightly above $z = 0$ is much more stable than that immediately below $z = 0$. This jump is expected to strongly influence the vertical transport since the liquid below $z = 0$ is not easily mixed with the liquid above, in other words a ‘shielding effect’ occurs. The corresponding layer is expected to have a structure for $x < 1$ similar to the double-diffusive layers above it; the fluid just below the slab is continuously cooled which results in a persistent horizontal temperature gradient near the slab corner at $z = 0$. The continuous transport of salty water from below the slab to the left may be an important mechanism in maintaining a strong buoyancy jump near $z = 0$, thereby supporting the shielding effect.

The layered structures, as well as the the exchange of salt due to the geometrically induced flow can be more clearly observed in the greyscale plot of the anomalous salinity distribution (difference with respect to the initial salinity) in Fig. 5.3b. The vertical lengthscale h of the layers can be estimated from Fig. 5.2d and Fig. 5.3b and it is found that the ratio h/D is about 0.24. Since D/η equals the buoyancy ratio $R = 2.5$ (based on the initial salinity profile), the ratio h/η is about 0.60. There exists a close agreement between the layer development next to the plate and the initial layer development in the square cavity simulation in Chapter 3 for $R = 2.5$. First, from Fig. 4 in Chapter 3 we calculate that the ratio h/D for the middle layer at $t = 0.05$ is about 0.3. With $D/\eta = 2.5$, the value of h/η becomes 0.8 which is slightly larger than the value obtained above for slab cooling. The latter difference is attributed to the fact that in Chapter 3 the overall temperature difference is slightly larger because the temperature along the wall is homogeneous, whereas for the slab, it decreases downward along the wall. The timescale of the development of the layers in both cases is quite similar. In the slab model, the second convection cell has advanced roughly over a distance $\Delta x = 0.5$ at $t = 0.055$. In Fig. 4 of Chapter 3, a similar scale for Δx is found at $t = 0.05$.

(a)

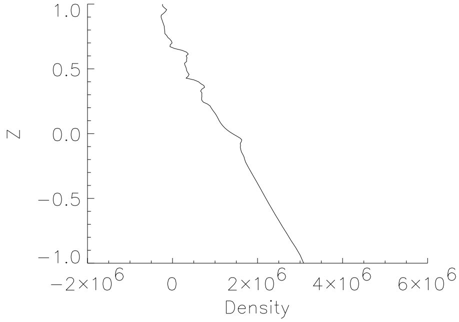

(b)

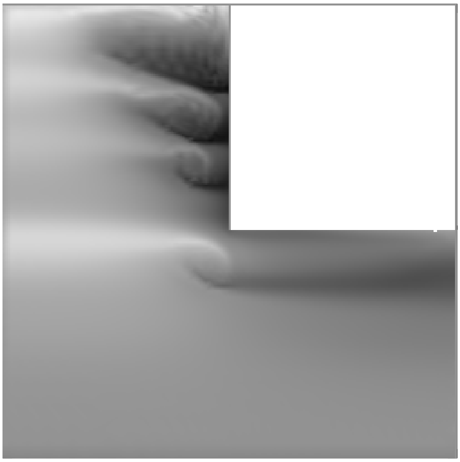

Figure 5.3: *(a): Vertical density distribution along section 5; (b): Grayscale plot of the anomalous salinity distribution (difference of actual and initial salinity) for case 'A',* $Ra_\eta = 5\ 10^4$. *Light (dark) regions indicate a higher (lower) salinity than the initial salinity.*

In case 'B' (5.2), the slab thickness is significantly smaller than the internal layer scale ($D/\eta = 0.1R = 0.25$). The patterns of the temperature and salinity (Fig. 5.4a) do not show any signatures of layer formation. On the contrary, there is strong mixing both next to and below the slab, the latter component again geometrically induced as can be seen from the velocity

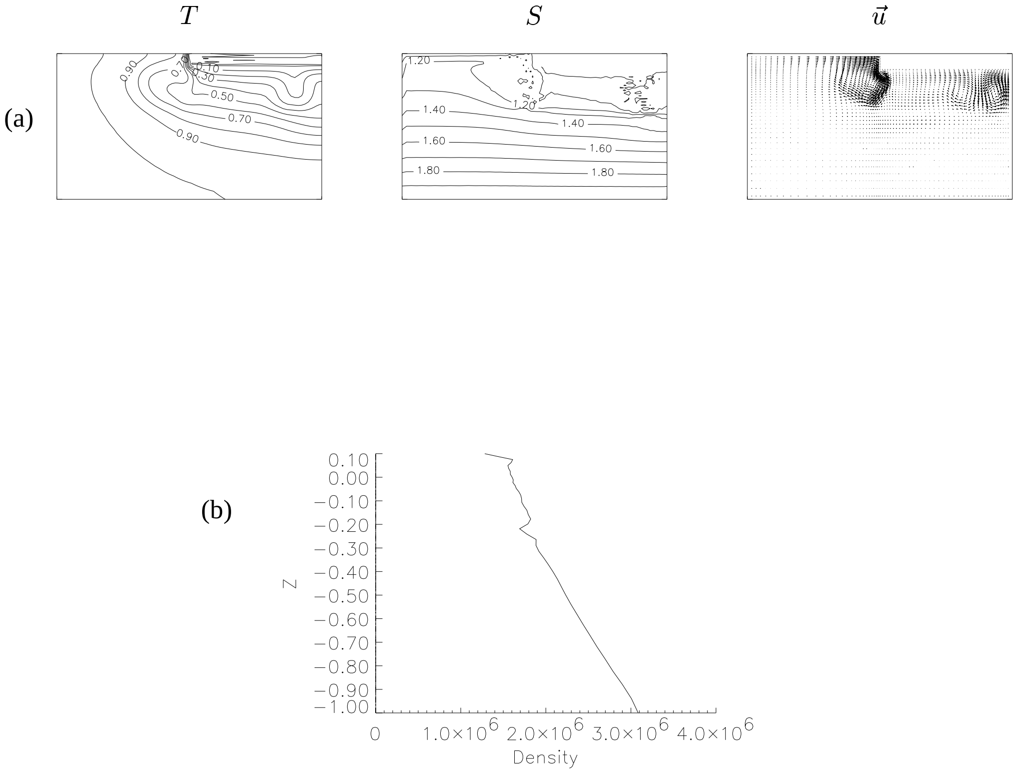

Figure 5.4: *(a): Temperature, salinity and velocity distributions at* $t = 5.5\ 10^{-2}$ *(*$2.2\ 10^4$ *s) for the stratified case 'B'; (b): Vertical density distribution along section 5.*

distribution. The latter flow strongly modifies the flow next to the slab resulting in the absence of step structures in the density profile (Fig. 5.4b). The results indicate that the slab should be sufficiently thick (larger than the internal lengthscale η) for the layers to develop. If the slab is thinner, a fluid element initially near the top of the layer that is descending along the slab must pass the corner of the slab before it can turn back inside the liquid. At that point the fluid element is necessarily influenced by the geometrically induced flow.

The value of Ra_η applied in the previous simulations is rather small compared to that in experiments performed by *Huppert and Turner* [1980]. Therefore, we increased the Rayleigh number while keeping R constant, which can be regarded as increasing the value of H while keeping other scales constant. In particular, when H is increased by a factor three, $Ra_\eta = 1.35\ 10^6$ results. For this value of Ra_η the computations are very expensive and only the initial

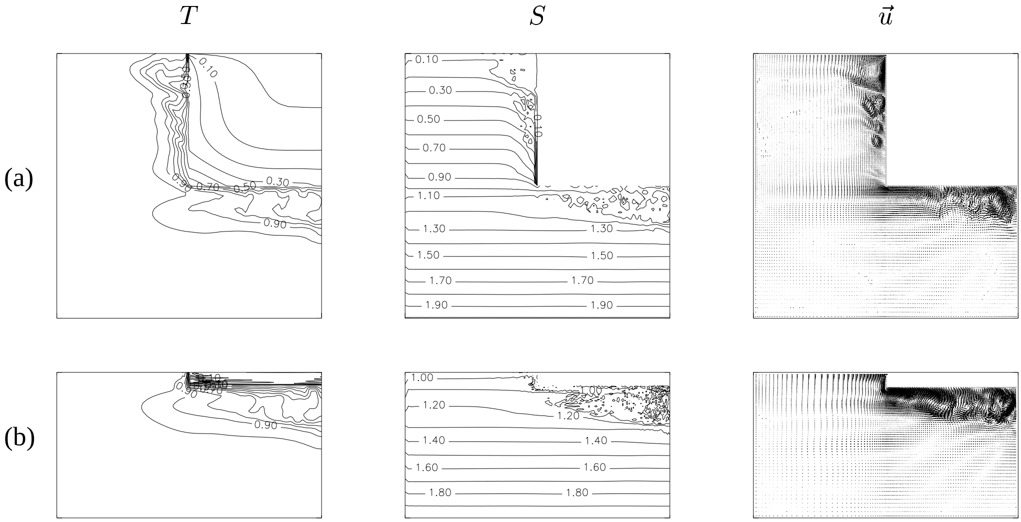

Figure 5.5: *Temperature, salinity and velocity distributions at* $t = 5 * 10^{-3}$ *(*$1.8 * 10^{4}$ *s) for the stratified cases,* $Ra_{\eta} = 1.35\ 10^{6}$*; (a): case 'A'; (b): case 'B'.*

stages of flow development were computed (up to $t = 5\ 10^{-3}$ or $t^{*} = 1.8\ 10^{4}\ [s]$). Since time scales with H^{2}, the same dimensional time t^{*} is reached at $t = 4.5\ 10^{-2}$ for the standard case $Ra_{\eta} = 5\ 10^{4}$.

The results for $Ra_{\eta} = 1.35\ 10^{6}$, shown in Fig. 5.5a ('A') and Fig. 5.5b ('B'), reveal a strong convective activity both next to as well as below the slab. Along the vertical slab wall for case 'A', a layered pattern develops similar to the simulation with $Ra_{\eta} = 5\ 10^{4}$ but with a slightly smaller thickness. This smaller scale appears because the simulation time is too small for subsequent layer merging to occur. In case 'B' no layered flow pattern develops for similar reasons as explained above. Again, most of the convective activity occurs below the slab. For both cases 'A' and 'B', significant convection is seen below the ice (Fig. 5.5) contrary to that in Fig. 5.2a and Fig. 5.4a. This is likely due to diffusive instabilities through vertical gradients [*Baines and Gill*, 1969], which have destabilized the thermal boundary layer below the slab. Its signatures are the formation of a well-mixed layer which is growing downwards through entrainment [*Molemaker and Dijkstra*, 1995].

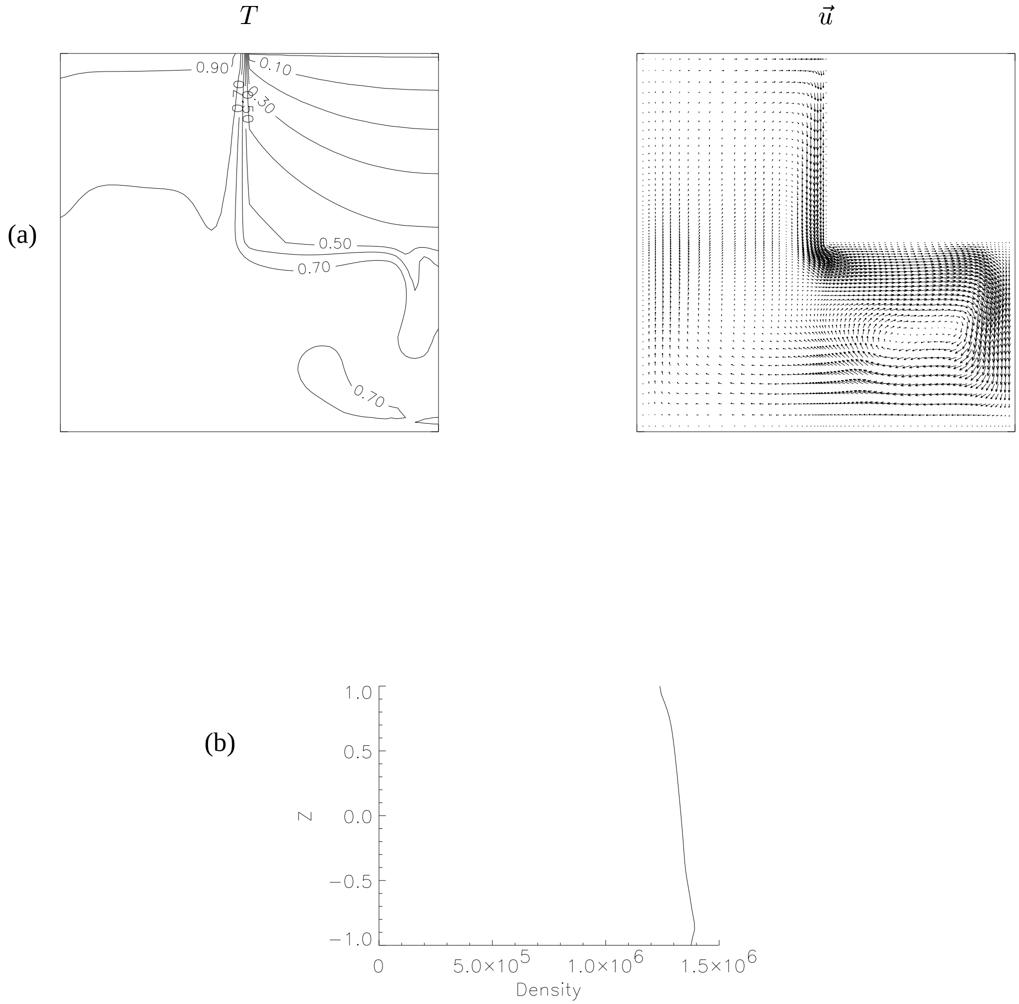

Figure 5.6: *(a): Temperature and velocity distributions for* $Ra_\eta = 5\ 10^4$ *at* $t = 5.5 * 10^{-2}$ *for the non-stratified case 'C'; (b): Vertical density distribution along section 5.*

5.3.2 Non-stratified background

Cases 'C' and 'D' (5.2) are equivalent to cases 'A' and 'B' but with the absence of the initial salinity gradient. Hence, the initial state consists of both homogeneous temperature and salinity distributions, i.e.

$$t = 0 : T(x,z) = 1 \; ; \; S(x,z) = 1 \; ; \; \Theta(x,z) = 1. \tag{5.9}$$

Note that if the salinity is homogeneous initially, it remains constant during the evolution since a constant solute concentration is compatible with the boundary conditions. Hence, only the flow due to the cooling of the liquid by thermally induced buoyancy is considered. In this way, the signatures of double-diffusive convection and, in particular, its influence on the heat and mass transport can be determined.

For the thick slab (Fig. 5.6a), a narrow thermal boundary layer forms next to the slab, of which the thickness increases downwards. This is a classical boundary layer for which the thickness scales with $Ra^{-\frac{1}{4}}$, where the Rayleigh number is based on the distance along the slab boundary. The flow below the slab is again geometrically induced by horizontal density gradients and occupies the whole region below the slab. Step structures in the density distribution at section 5 are absent (Fig. 5.6b), demonstrating that layer formation does not occur .

For the thin slab, the boundary layer next to the ice has a near constant thickness and the convection below the ice is much weaker because the temperature gradient in the ice is much smaller (Fig. 5.7a). Apart from that, the flow is very similar to that of the thick slab in that no appreciable flow appears next to the ice resulting in nearly the same density profile as that in Fig. 5.6b at section 5 (Fig 5.7b).

For $Ra_\eta = 1.35 \; 10^6$, snapshots of the flows in the cases 'C' and 'D' are shown in Fig 5.8a and Fig. 5.8b, respectively. The boundary layer thickness next to the ice is smaller, as expected, and convection is much more intense below the ice. However, still no appreciable flow develops far from the slab next to the ice. This picture is in qualitative agreement with the experimental results of *Gebhart et al.* [1983] which also show a thermally induced vigorous flow just below an ice surface. With a lengthscale equal to half of the length of the slab and a temperature difference of order $O(1)$ between the ice slab and the bulk of the liquid, their Rayleigh number is about Ra_η is about 3.2 10^6, near the value used in our simulation.

5.3.3 Heat and Mass Transfer

An analysis of the heat and mass transport of the flows computed above is considered through the values of the integrated transport across the sections depicted in Fig. 1a. The horizontal heat and salt fluxes across sections 1 and 2 are defined as

$$\Phi_T^h \quad = \quad \int_{z=-1}^{z=0} \left[uT - \partial T / \partial x \right]_{x=x_i} dz \; ; \tag{5.10a}$$

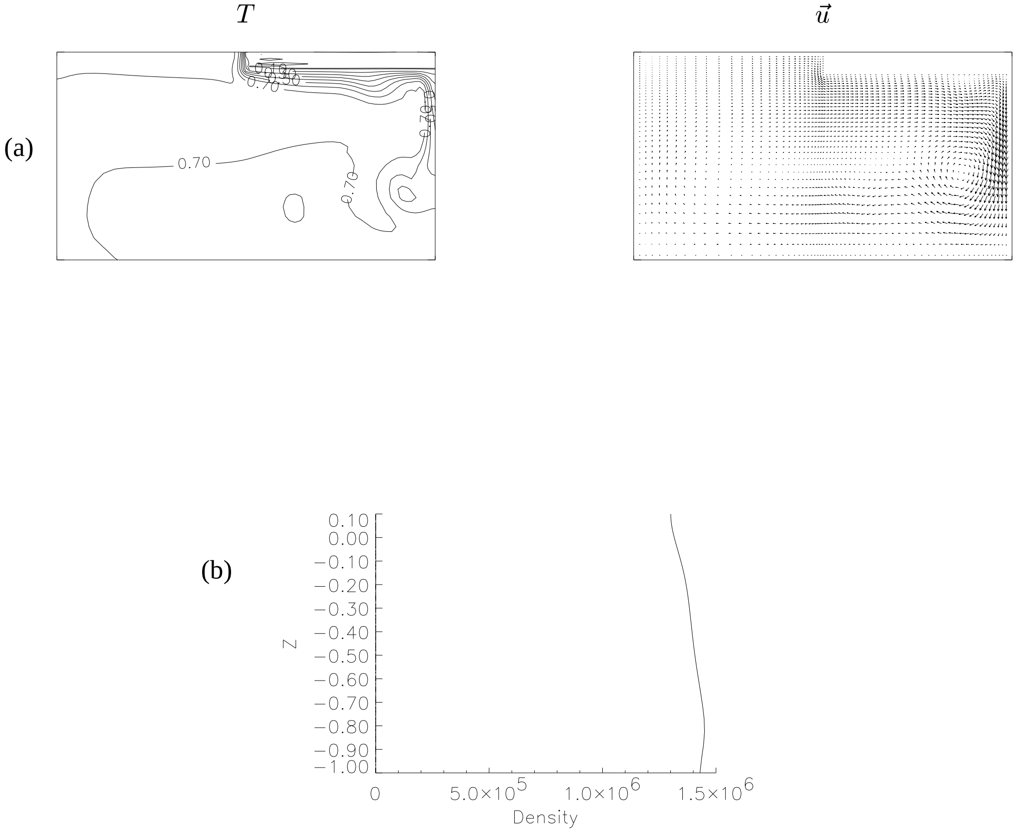

Figure 5.7: *(a): Temperature and velocity distributions for* $Ra_\eta = 5\ 10^4$ *at* $t = 5.5\ 10^{-2}$ *for the non-stratified case 'D'; (b): Vertical density distribution along section 5.*

$$\Phi_S^h \quad = \quad \int_{z=-1}^{z=0} \left[uS - Le^{-1}\partial S/\partial x\right]_{x=x_i} dz, \tag{5.10b}$$

whereas the vertical fluxes across sections 3 and 4 are computed through

$$\Phi_T^v \quad = \quad \int_{x=0}^{x=1} \left[wT - \partial T/\partial z\right]_{z=z_j} dx\ ; \tag{5.11a}$$

$$\Phi_S^v \quad = \quad \int_{x=0}^{x=1} \left[wS - Le^{-1}\partial S/\partial z\right]_{z=z_j} dx. \tag{5.11b}$$

In Fig. 5.9, the evolution of the salt fluxes along the sections 1 and 3 is shown for case 'A'. These fluxes are not expected to change significantly beyond the simulation time, unless subsequent

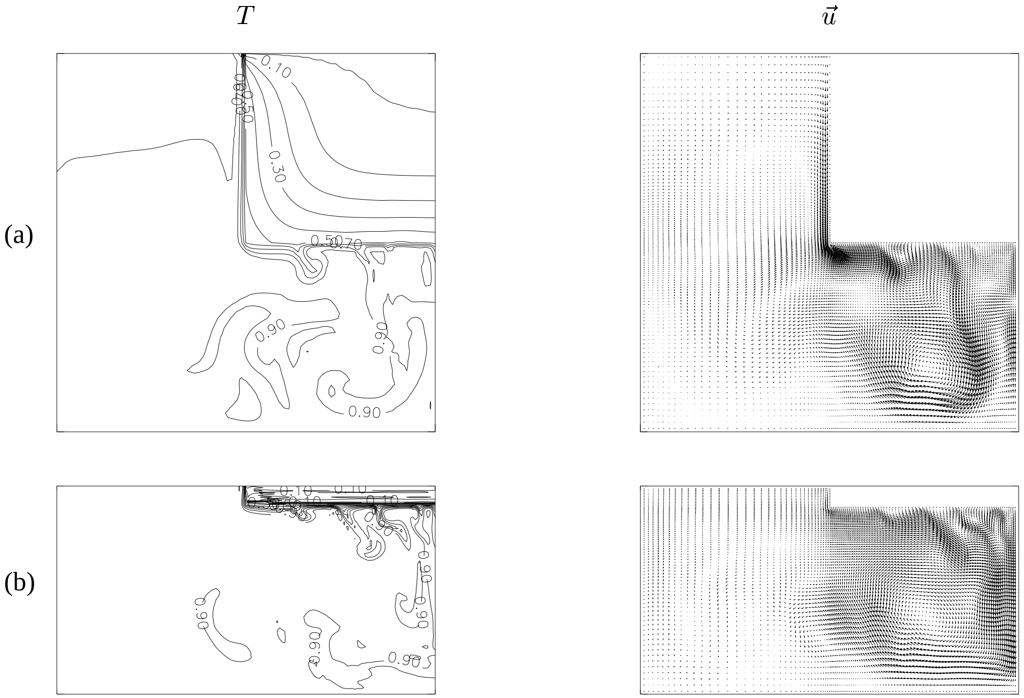

Figure 5.8: *Temperature distributions at* $t = 5\ 10^{-3}$ *for the nonstratified cases,* $Ra_\eta = 1.35\ 10^6$*; (a): case 'C '; (b): case 'D'.*

layer merging occurs leading to a different flow pattern. Nevertheless, these flows are (at best) quasi-stationary and the calculations on the heat and mass transport represent only snapshots. However, the results should be sufficient to determine the qualitative differences of the transport between the flows considered. The heat and salt fluxes across the sections $1 - 4$ for the cases 'A - D' ($Ra_\eta = 5\ 10^4$) are presented in Table 5.3 and Table 5.4, respectively. A positive value indicates transport of the particular quantity in the positive x - or z - direction.

The reduction of vertical heat transport due to layer formation can be immediately seen by comparing the heat transport through the sections 3 and 4 for the cases 'A' and 'B' (Table 5.3). Both values are significantly smaller for case 'A', indicating that the 'shielding effect' has a pronounced effect on the vertical transport of heat. The same follows for the vertical salt transport which is mainly upwards at both sections in case 'B', but upwards at section 3 in case 'A' and downwards at section 4 (Table 5.4). The latter result indicates that the layered flow also causes a

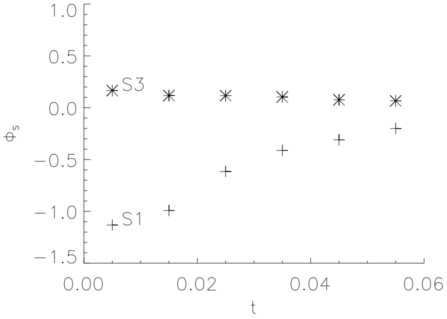

Figure 5.9: *The temporal development of salt fluxes Φ_S along sections 1 (S1) and 3 (S3) for Case 'A'.*

Case	section 1	section 2	section 3	section 4
A	0.143	0.085	0.493	0.593
B	0.672	-0.513	1.50	0.952
C	-0.530	1.02	2.84	3.07
D	2.48	0.055	1.25	0.764

Table 5.3: Integrated heat fluxes along sections indicated in Fig. 1a, $t = 4.5\ 10^{-2}$, $Ra_\eta = 5\ 10^4$.

Case	section 1	section 2	section 3	section 4
A	-0.310	-0.123	0.076	-0.023
B	-0.387	-0.424	0.437	0.349

Table 5.4: Integrated salt fluxes along sections indicated in Fig. 1a, $t = 4.5\ 10^{-2}$, $Ra_\eta = 5\ 10^4$.

strong reduction in the vertical transport of salt, and that salt transport is mainly lateral.

Below the slab, the lateral heat transport is also much smaller in case 'A' than in case 'B' along section 1 (Table 5.3). This is a consequence of the strong geometrically induced flow in case 'B' (Fig. 5.4a), where warm water is mixed under the ice; this effect is much smaller in case

’A’ (Fig. 5.2d). The same flow can explain the different heat transport along section 2. The salt transport is to the left along both sections 1 and 2 (Table 5.4), due to the return flow far below the ice. This net transport is partly responsible for the strong stratification near $z = 0$, inducing the buoyancy jump associated with the ’shielding effect’ in case ’A’, as discussed below.

The vertical transport of heat in the non-stratified case takes place mainly within the boundary layer near the slab. Since the flow is downward and the ice cools the liquid, the effective heat transport is upwards resulting in the positive values in Table 5.3 for the cases ’C’ and ’D’. The boundary layer flow is much stronger for the thick slab (compare Fig. 5.6a and Fig. 5.7a) resulting in much larger values for the heat transport along sections 3 and 4 in case ’C’. Since the flow below the ice is likely to be very intermittent, not much value can be put on the actual numbers of the horizontal heat transport along the sections 1 and 2; these are at most indicative.

5.4 Discussion

In this chapter, we considered buoyancy driven flows in a liquid near a cooled solid boundary. The liquid has either a constant background salinity or is stratified through a constant salinity gradient. In both cases, the average salinity is large enough such that a linear equation of state is applicable. Through the idealization of the ice as a non-deformable boundary dilution effects due to the melting of the ice were not considered. Also the effect of the freezing point depression due to salinity was neglected. Both features may be important in ’real’ convection near ice boundaries, but are out of the scope of this study.

It was shown that the two types of flow are completely different. In the non-stratified case, the flow in a thin boundary layer near the ice is responsible for the vertical transport of heat and salt next to the ice. Hardly any flow develops outside this boundary layer. Vigorous convection develops below the ice, forced by the temperature gradients in the ice. The thickness of the slab plays a minor role and although the intensity of the flow does depend on Ra_η, the overall character does not.

On the contrary, for the flows developing in the stratified environment, the lateral cooling of the liquid results, through double diffusive processes, in the formation of horizontal layers with a characteristic lengtscale η. For the particular case ’A’ investigated, the result $h/\eta = 0.6$ compares quite well with the scales as reported by *Huppert and Turner* [1980] and presented in their Tables 1 - 3. For example, considering experiments nr. 2 and nr. 3 in their Table 1, experiments nr. 1, nr. 6 and nr. 8 in their Table 2, and experiment nr. 14 in their Table 3, we see that for values of Ra_η close to $5\ 10^4$ the corresponding values of h/η are in the range $[0.56, 0.98]$. Moreover, our particular value is close to the value of $h/\eta = 0.65$ they propose based on all experiments. The double-diffusive flow next to the slab appears to be little influenced by the flows in other regions due to the buoyancy jump generated at the lower slab edge. This jump arises through both the appearance of layers and the geometrically induced flow. Since the salinity is low near the ice, relatively fresh-water is transported to the left by the convection just above $z = 0$ (Fig. 5.2d and Fig. 5.3b). By the geometrically induced flow, salt is transported upwards just below $z = 0$ (Fig. 5.2d) resulting in the density jump near $z = 0$. The resulting 'shielding effect' was shown to have an enormous impact on the vertical transport of heat and salt near the ice.

For layers to appear, it is necessary that the thickness of the slab is larger than the length scale η. A layered flow will not develop due to lateral gradients if the thickness is smaller than η because the flow is disturbed by the geometrically induced flow below the ice. In oceanographic measurements of step structures [*Horne*, 1985], the density gradient in the ocean is 3 orders of magnitude smaller and Ra_η is a factor 10^8 larger. This leads to scales η of the order $0.1 - 0.2\ [m]$. These layers can therefore indeed be attributed to sideways cooling due to an ice slab and both sea-ice and icebergs will be able to induce them. However, it may not be easy to distinguish the origin of the layers in terms of the destabilizing background temperature gradient. For example, all measurements used in *Kelley* [1984] to compute overall mixing coefficients due to double diffusive processes assume that these layered flows are caused by a vertical destabilizing heat flux (through diffusive instabilities [*Baines and Gill*, 1969]). However, the layers may just as well be caused by sideways cooling, for example through icebergs, which are likely to be present at some of the locations. The origin of the layers is therefore an important issue, since different layer scales may result and thereby different mixing coefficients.

References

Baines, P.G. & Gill, A.E., On thermohaline convection with linear gradients. *J. Fluid Mech.*, **37**, 289-306, (1969)

Chen, C. F., Briggs, D. G., Wirtz, Stability of thermal convection in a salinity gradient due to lateral heating, *Int. J. Heat Mass Transfer*, **14**, 57–65 (1971).

Carey, V.P., Gebhart, B., Transport near a vertical ice surface melting in saline water: some numerical calculations, *J. Fluid Mech.*, **117**, 379–402 (1982)

Dijkstra, H. A. and Kranenborg, E.J., The evolution of double-diffusive intrusions into a stably stratified liquid. II: The physics of self-propagation. *Int. J. Heat Mass Transfer*, submitted (1996b).

Gebhart, B., Sammakia, B., and Audunson, T., Melting Characteristics of Horizontal Ice Surfaces in Cold Saline Water, *J. Geophys. Research*, **88**, C5, 2935–2942, (1983).

Horne, E. P. W., Ice-induced Vertical Circulation in an Arctic Fiord, *J. Geophys. Research*, **90**, C1, 1078–1086 (1985).

Huppert, H. E., Josberger, E. G., The melting of ice in cold stratified water, *J. Phys. Oceanogr.*, **10**, 953–960 (1980).

Huppert, H. E., Turner, J. S., On melting icebergs, *Nature*, **271**, 46–48 (1978).

Huppert, H. E., Turner, J. S., Ice blocks melting into a salinity gradient. *J. Fluid Mech.*, **100**, 367–384 (1980).

Jeevaraj, C., Imberger, J., Experimental study of double-diffusive instability in sidewall heating, *J. Fluid Mech.*, **222**, 565–586 (1991).

Josberger, E. G., Martin, S., A laboratory and theoretical study of the boundary layer adjacent to a vertical melting ice wall in salt water, *J. Fluid Mech.*, **111**, 439–473 (1981).

Kerr, O. S., Heating a salinity gradient from a vertical sidewall: nonlinear theory, *J. Fluid Mech.*, **217**, 529–546 (1990).

Kranenborg, E. J., Dijkstra, H. A., The evolution of double-diffusive intrusions into a stably stratified liquid. I: A study of the layer merging process. *Int. J. Heat Mass Transfer*, submitted (1996).

Kelley, D.E., Effective diffusivities within ocean thermohaline staircases. *J. Geophys. Res.* **89**, 10,484-10,488, (1984).

Molemaker, M.J. & Dijkstra, H.A., Layer formation in a stably stratified liquid cooled from above. *Double Diffusive Convection, ed. A. Brandt and H.J.S. Fernando, Geophysical Monograph*, **94**, 97-104, (1995).

Schladow, S. G., Thomas, E., Koseff, J. R., The dynamics of intrusions into a thermohaline stratification, *J. Fluid Mech.*, **236**, 127–165 (1992).

Segal, A. *SEPRAN user manual*, SEPRA Analysis, The Netherlands (1994).

Schmitt, R.W., Double diffusion in oceanography, *Ann. Rev. Fluid Mech.*, **26**, 255-285 (1994).

Tanny, J., Tsinober, A. B., The dynamics and structure of double-diffusive layers in sidewall-heating experiments, *J. Fluid Mech.*, **196**,135–156 (1988).

Thangam, S., Zebib, A. & Chen, C. F., Transition from shear to sideways diffusive instability in a vertical slot, *J. Fluid Mech.*, **112**, 151–160 (1981).

Chapter 6

Effective diffusivities in laterally heated double-diffusive systems

The effective vertical diffusivity for salt is estimated for laterally heated double-diffusive layered structures. First, the vertical interfacial salt fluxes are calculated using data retrieved from five different numerical simulations. The salt fluxes are shown to be consistent with the flux law for a diffusive interface, derived from laboratory experiments. The fluxes appear to be independent on the buoyancy (stability) ratio over the interface for the range considered and for a typical Rayleigh number (based on the horizontal temperature difference and vertical layer scale η*) of* $Ra_\eta = O(10^5)$*. The effective vertical salt diffusivity* K_S *is almost five times larger than the molecular salt diffusivity* κ_S *but is much smaller than the values available for oceanic layered structures (*$Ra_\eta = O(10^9)$*). An extrapolation towards* $Ra_\eta = O(10^9)$ *yields a value of the same order as determined from measurements, namely* $K_S = O(10^{-7})\ m^2 s^{-1}$*, indicating that the vertical effective salt diffusivities are of the same order for both laterally and vertically cooled double-diffusive structures.*

6.1 Introduction

The previous chapters have shown that the lateral heating or cooling of a stable salinity gradient can lead to the formation of a layered structure consisting of horizontal convective layers separated by thin diffusive interfaces. In these interfaces the vertical velocity is (almost) zero, leaving only vertical diffusion as a possible transport mechanism. However, the convection has strongly modified the salinity gradient in the interface, resulting in an increased vertical salt flux. In this

Case	Ra_η	R
1	$5\ 10^4$	5
2	$2\ 10^5$	5
3	$5\ 10^4$	2.5
4	$1\ 10^6$	2.5
5	$5\ 10^4$	10

Table 6.1: *The parameters distinguishing the five simulations.*

chapter, an estimate of the vertical effective salt diffusivity will be determined.

If a stable salt gradient is heated from below, a layered structure is formed which is very similar (although with a different layer scaling [*Turner*, 1973]) to the laterally heated cases, i.e. well-mixed convective layers are formed separated by diffusive interfaces in which steep temperature and salt gradients are present. Flux laws have been derived for the vertical heat and salt fluxes across these interfaces [*Huppert*, 1971]. Effective vertical diffusivities for heat and salt have been determined for oceanographic double-diffusive layered structures [*Kelley*, 1984] using these flux laws because these structures were assumed to be generated by vertical thermal forcing. Main goal was to express the fluxes in terms of overall temperature and salinity differences, in order to parametrize the large-scale transports induced by the structures. In our laterally heated model simulations, the vertical salt distribution is akin to the distribution in vertically heated or cooled systems, and this gives rise to the question whether the flux law for the vertical salt flux also applies to our results.

High-resolution simulations like those in Chapter 3 are necessary to determine the interfacial fluxes accurately. Due to the absence of a thermal background stratification in the simulations (generally, no-flux conditions for temperature at the lower and upper boundaries apply and an initial thermal gradient is absent too) it is not possible to derive a vertical effective thermal diffusivity. Therefore only the effective vertical salt diffusivity K_S will be determined.

In this chapter an estimate of the vertical salt flux will be derived from five different numerical simulations. The applicability of the flux law is investigated. Next, K_S is calculated and extrapolated towards higher Rayleigh numbers relevant for oceanographic conditions and compared to the results of *Kelley* [1984]. The consequence for the generation mechanism of oceanographic double-diffusive structures is discussed.

Case	R_ρ	δT	δS	$-\partial S/\partial z$	$10^2\Phi_S$	10^2F_S
1	7.70	0.136	0.209	2.986	3.0	4.5
1	10.05	0.087	0.175	2.692	2.7	3.6
1	11.45	0.075	0.172	3.127	3.1	3.5
1	11.55	0.081	0.187	3.400	3.4	3.9
2	4.70	0.155	0.146	3.244	3.2	4.4
2	6.16	0.129	0.159	3.975	3.9	5.0
2	7.45	0.100	0.149	3.725	3.7	4.6
2	8.80	0.124	0.218	5.450	5.4	7.6
3	4.28	0.174	0.297	4.569	4.5	2.9
3	4.52	0.180	0.326	4.075	4.0	3.2
4	2.10	0.233	0.197	2.627	2.6	4.5
4	3.22	0.173	0.223	4.660	4.6	5.3
4	3.55	0.169	0.240	4.800	4.8	5.8
5	11.20	0.118	0.132	2.933	2.9	6.2
5	16.20	0.106	0.172	3.440	3.4	8.8

Table 6.2: *The local values of the dimensionless variables used for the calculation of the vertical dimensionless salt fluxes across the interfaces. Also shown are the resulting values of* Φ_S *(6.1) and* F_S *(6.3).*

6.2 The salt fluxes over the diffusive interfaces

For the calculation of the salt fluxes over the diffusive interfaces, the results of five different simulations were used. The parameters of these simulations are given in Table 6.1 (for definitions of these parameters, see Chapter 3). Cases 1 – 3 correspond to the results of the simulations in Chapter 3 taken at $t = 0.1$, but for cases 4 – 5 new simulations were performed with either larger Ra_η (case 4) or larger R (case 5). The other parameters retained the same value, i.e. $Pr = 7$, $Le = 101$ and $A = 1$. For these simulations the same integration method and gridsize were used as for cases 1 – 3, i.e. explicit time integration on a 201*201 grid. The layered structures visible at $t = 0.1$ for the five cases are shown in Fig. 6.1 in the form of salinity plots. For all cases the layer scale $\eta = \alpha\Delta T/\beta\Phi_0$ (the heigth a fluid parcel containing a heat surplus ΔT would rise in a linear salinity gradient with strength $\Phi_0 = -\partial S/\partial z$ until density equalisation occurs) appears to be valid. To calculate the jumps in temperature and salinity across the diffusive interfaces, vertical sections of the temperature and salinity were taken at the centre of the cavity and are shown in Fig. 6.2. Only those interfaces were regarded over which the temperature gradients were well-developed. The resulting jumps and the corresponding salt gradients are presented in the left part of Table 6.2. Here δT and δS are the jumps in temperature and salinity across the interfaces, and R_ρ is the (local) stability ratio defined as $R_\rho = \beta\delta S^*/\alpha\delta T^* = R\delta S/\delta T$ (stars denoting dimensional quantities).

The dimensionless vertical salt flux Φ_S across each interface can be calculated from:

$$\Phi_S = -Le^{-1}\frac{\partial S}{\partial z} \tag{6.1}$$

and is tabulated in Table 6.2. An estimate of the vertical salt flux is then obtained by averaging the column values of Φ_S in Table 6.2:

$$\Phi_S = 3.7\ 10^{-2}. \tag{6.2}$$

A comparison with the purely diffusive flux, equal to $Le^{-1} = 1\ 10^{-2}$, shows that convection has lead to a fourfold increase of the vertical salt flux.

At this point we check whether the vertical salt flux satisfies the flux law for diffusive interfaces. In Appendix C a flux law for the vertical salt flux is derived for a double-diffusive system where the vertical salinity distribution has a characteristic ”step”-structure, i.e. salt is well-mixed in the convective layers, whereas strong salinity gradients exist within the diffusive interfaces. In our laterally heated cases the vertical salinity distribution corresponds has this step-like structure, in contrast with the vertical temperature distribution. Therefore, according to Appendix C, expression (C.8), we use the following expression for the dimensionless vertical salt flux F_S:

$$F_S = c_S\ (Ra_\eta R^4)^{1/3}\ (-\delta S)^{4/3}. \tag{6.3}$$

As a test of the validity of flux law (6.3) the quantity $(\ F_S/(Ra_\eta R^4)^{1/3}\ )^{3/4}$ is plotted against δS in Fig. 6.3. Fig. 6.3 clearly reveals a linear relationship, which indicates that c_S is a constant. Due to scatter a range of slopes is possible; based on extremal values we derive the following range of values for c_S:

$$\text{range } c_S \in [1.15\ 10^{-3},\ 4.29\ 10^{-3}].$$

The minimum of this range provides a good value for c_S;

$$c_S = 1.15\ 10^{-3}. \tag{6.4}$$

Using this value, F_S is calculated for each interface and presented in Table 6.2. Averaging these values gives an estimate of the salt flux as calculated with the flux law (6.3):

$$F_S = 4.9\ 10^{-2}. \tag{6.5}$$

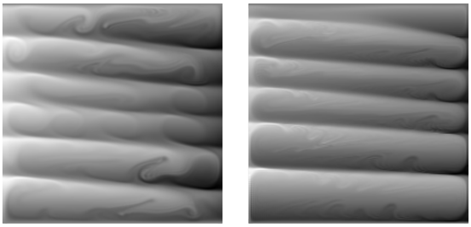

Case 1:
$Ra_\eta = 5\ 10^4$,
$R = 5$

Case 2:
$Ra_\eta = 2\ 10^5$,
$R = 5$

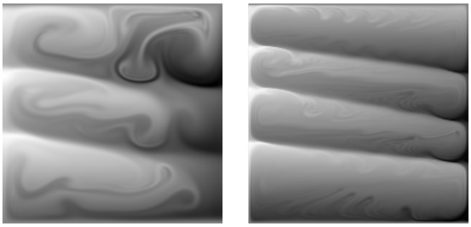

Case 3:
$Ra_\eta = 5\ 10^4$,
$R = 2.5$

Case 4:
$Ra_\eta = 1\ 10^6$,
$R = 2.5$

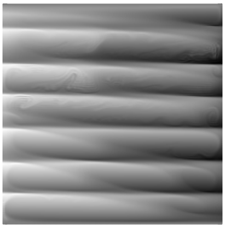

Case 5:
$Ra_\eta = 5\ 10^4$,
$R = 10$

Figure 6.1: *Grey-scale plots of the five cases; shown is the salt distribution minus the initial linear stratification.*

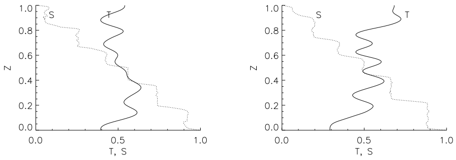

Case 1:
$Ra_\eta = 5\ 10^4$,
$R = 5$

Case 2:
$Ra_\eta = 2\ 10^5$,
$R = 5$

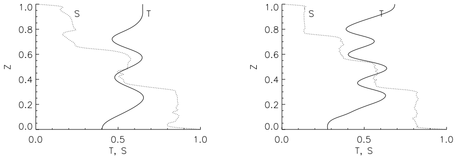

Case 3:
$Ra_\eta = 5\ 10^4$,
$R = 2.5$

Case 4:
$Ra_\eta = 1\ 10^6$,
$R = 2.5$

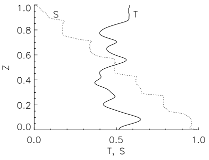

Case 5:
$Ra_\eta = 5\ 10^4$,
$R = 10$

Figure 6.2: *Vertical sections of T and S through the centre of the container for each case.*

The estimates (6.2) and (6.5) are of the same order, which shows that the flux law can be applied with succes in laterally heated double-diffusive systems.

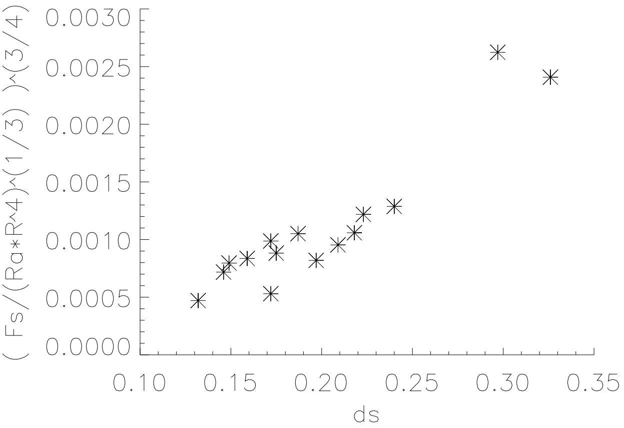

Figure 6.3: *Plot of* $(F_S/(Ra_\eta R^4)^{1/3})^{3/4}$ *as a function of* δS.

The effective dimensionless vertical salt diffusivity K_S can be defined as the ratio of the estimated vertical salt flux (6.5) and the dimensionless vertical background salt gradient. Since the latter equals one, we have the following estimate:

$$K_S = 4.9\ 10^{-2}. \tag{6.6}$$

Finally, the dimensional diffusivity K_S^* results from the application of the scales H and H^2/κ_T for length and time respectively:

$$\begin{aligned} K_S^* &= \kappa_T\, K_S \qquad\qquad (\kappa_T = 1.4\ 10^{-7}\ \mathrm{m^2 s^{-1}}) \\ &= 6.9\ 10^{-9}\ \mathrm{m^2 s^{-1}}\ . \end{aligned} \tag{6.7}$$

6.3 Discussion

The vertical salt flux in a laterally heated double-diffusive system has been shown to satisfy the flux law (6.3) for a diffusive interface. This is to be expected since, in our simulations, the vertical salt distribution is such that salt is well mixed in the convective layers, while steep salt gradients exist in the interfaces; a situation which applies also to layered double-diffusive structures that are thermally forced from below. For the range of Ra_η considered, the salt flux F_S appears to be independent of the stability ratio R_ρ, in contrast with oceanographic conditions at much larger Ra_η [*Kelley*, 1984], where the interfaces become less stable for small values of R_ρ [*Huppert*, 1971], resulting in an increased salt flux . The stability of the interfaces in our simulations is clear when the salinity perturbation plots in Fig. 6.1 are considered; the interfaces between the layers are clear and convection in the layers between the interfaces does not appear to destroy them. The estimate of K_S^* that has been determined for the simulations ($K_S^* = 6.9\ 10^{-9}\ \mathrm{m^2s^{-1}}$) is about five times larger than the molecular salt diffusivity ($\kappa_S = 1.4\ 10^{-9}\ \mathrm{m^2s^{-1}}$). This value is probably not very accurate since a range of values of c_S is possible. This is caused by scatter in Fig. 6.3 which may be attributed to the fact that some layers are not fully developed (for example in case 3, which becomes clear from Fig. 6.1c). Yet, the value chosen is of the same order as the salt diffusivity which has been calculated directly from the local salt gradients over the interfaces.

It is of interest to know whether the determined value of K_S^* is relevant in an oceanographical context. *Kelley* [1984] estimated the values of both thermal and saline diffusivity coefficients from oceanographic measurements of double-diffusive layered structures. He assumed that these layers were formed as a result of vertical cooling. Therefore we have to extrapolate K_S^*, estimated for $Ra_\eta = O(10^5)$, to values representative of oceanographic conditions as measured by *Kelley* [1984] ($Ra_\eta = O(10^9)$). Firstly, we show that the saline diffusivity is a function of Ra_η only. We start with expressing (6.3) in terms of the layer thickness scale η which has been shown both experimentally and numerically in the previous chapters to be valid for a large range of Rayleigh number. Assuming that the steps over the diffusive interfaces are of the same strength, the relation $\eta = H/R$ implies:

$$\delta S = O(R^{-1}). \tag{6.8}$$

Substituting this expression into (6.3), we arrive at:

$$F_S = c_S\ Ra_\eta^{1/3}, \tag{6.9}$$

which indeed shows that F_S - and therefore F_S^* and K_S^* - depends on Ra_η only.

An increase of Ra_η with a factor $O(10^4)$ results in $K_S^* = O(1.4\ 10^{-7}\ \mathrm{m^2s^{-1}})$. This value is certainly in the range of K_S^* as calculated by *Kelley* [1984] and depicted in his Figure 2. This result indicates that the vertical salt fluxes for vertically and laterally forced systems are the same. Still, more simulations are necessary, especially for $Ra_\eta > 10^5$, to determine accurate values for the effective salt diffusivity.

References

Huppert, H. E., On the stability of a series of double-diffusive layers, *Deep-Sea Res.*, 18, 1005-1021 (1971).

Kelley, D., Effective diffusivities within oceanic thermohaline staircases, *J. Geophys. Res.*, 89, 10,484-10,488 (1984).

Turner, J. S., *Buoyancy effects in fluids*, Cambridge (1973).

Appendix A

The continuation technique

A.1 Method description

The continuation method is an important tool in parameter studies as it allows steady state solutions to be traced systematically in parameter space. The method was originally proposed by *Keller* [1977], and since then extensions and numerous applications have been published (for example; Marangoni convection in small aspect-ratio containers by *Dijkstra* [1992], vortex shedding past variously shaped bodies by *Jackson* [1987], porous medium convection by *Riley and Winters* [1989]). General aspects of continuation techniques are described in *Seydel* [1994], the description of the implementation used here stems largely from *Dijkstra* [1995].

First we turn to some notational conventions. We assume that the finite-difference discretisation technique has been applied to the model equations of Chapter 2, using a grid with n points in the horizontal (x) direction and m points in the vertical (z) direction. The solution vector $\vec{u}$ has $N = 4 * nm$ components and can be written as

$$\begin{aligned} \vec{u} &= (\omega_{1,1}, \psi_{1,1}, T_{1,1}, S_{1,1}, \ldots, \omega_{n,m}, \psi_{n,m}, T_{n,m}, S_{n,m})^T \\ &= (u_1, \ldots, u_N)^T. \end{aligned} \tag{A.1}$$

The parameters in our model can be combined into one vector $\vec{p}$:

$$\vec{p} = (Ra_T, R_\rho, Pr, Le, A)^T. \tag{A.2}$$

The solution vector $\vec{u} \in \Re^N$ is to satisfy the following set of N equations that arises after discretisation of the model equations:

$$\Phi_{n,m}(\vec{u}, \vec{p}) = \vec{0}, \tag{A.3}$$

with $\Phi_{n,m} : \Re^N \times \Re^5 \rightarrow \Re^N$. In the sequel we will write Φ instead of $\Phi_{n,m}$ for convenience.

The continuation technique allows us to follow branches of steady state solutions as a function of one of the parameters in $\vec{p}$, from now on referred to as λ. A solution branch must be parameterized in some way, and at this point we introduce the commonly used arclength parameter s. A solution branch is then geometrically represented by the curve

$$\vec{\gamma}(s) = (\vec{u}(s), \lambda(s))^T, \tag{A.4}$$

where s gets its meaning of arclength by the requirement that the tangent to the curve in a point s_0, $\dot{\vec{\gamma}}(s_0)$, has unit length:

$$\dot{\vec{u}}^T(s_0)\dot{\vec{u}}(s_0) + \dot{\lambda}^2(s_0) = 1. \tag{A.5}$$

Equation (A.5) provides the extra constraint needed due to the addition of s. In computations we generally use a simple linearization in s_0 of (A.5) (known as pseudo-arclength parameterization):

$$\dot{\vec{u}}(s_0)\{\vec{u}(s) - \vec{u}(s_0)\} + \dot{\lambda}(s_0)\{\lambda(s) - \lambda(s_0)\} - \Delta S = 0, \tag{A.6}$$

where $\Delta S = s - s_0$ is a steplength along the branch to be chosen by the user.

We now restate the problem as follows; given a solution $\vec{u}_0 = \vec{u}(s_0)$ of (A.3) at a particular parameter value $\lambda_0 = \lambda(s_0)$ and a user-selected steplength ΔS, find a new solution on the branch by solving the following system:

$$\Phi(\vec{u}(s), \lambda(s)) = \vec{0} \tag{A.7a}$$

$$\dot{\vec{u}}_0^T(\vec{u} - \vec{u}_0) + \dot{\lambda}_0(\lambda - \lambda_0) - \Delta S = 0. \tag{A.7b}$$

The Jacobian corresponding to (A.7) reads:

$$J(s) = \begin{bmatrix} \Phi_{\vec{u}} & \Phi_{\lambda} \\ \dot{\vec{u}}^T & \dot{\lambda} \end{bmatrix}. \tag{A.8}$$

According to the properties of J in a point $(\vec{u}, \lambda)$ we define the following classification:

1. *Regular point*: $\Phi_{\vec{u}}$ is non-singular.

2. *Limit point*: dim(ker($\Phi_{\vec{u}}$)) = 1,
   $\Phi_\lambda \notin$ range($\Phi_{\vec{u}}$).

3. *Simple bifurcation point*: dim(ker($\Phi_{\vec{u}}$)) = 1,
   $\Phi_\lambda \in$ range($\Phi_{\vec{u}}$).

In the first two cases J is non-singular which implies that the branch can be continued in a unique way. The pseudo-arclength parameterization allows continuation through a limit point without problems. In a bifurcation point the solution is not unique; in the next section is described how the secondary branches emanating from this point are reached.
Although the classification is far from complete, the three mentioned cases are the most important ones, and currently these are the only cases we can identify.

A.2 Numerical implementation aspects

Given a solution on the branch, $(\vec{u}_0, \lambda_0)$, a new solution $(\vec{u}_1, \lambda_1)$ is found using a predictor-corrector technique. The predictor can be derived from the tangent to the branch at s_0 which is calculated by taking the total derivative of (A.7a) to s in s_0:

$$\begin{aligned}\frac{\mathbf{D}}{\mathbf{D}s}\Phi(\vec{u}(s_0), \lambda(s_0)) &= [\Phi_{\vec{\gamma}}]\,\dot{\vec{\gamma}}_0 \\ &= [\Phi_{\vec{u}}\ \Phi_\lambda]\begin{bmatrix}\dot{\vec{u}}_0 \\ \dot{\lambda}_0\end{bmatrix} = 0.\end{aligned} \tag{A.9}$$

In computations we first set $\dot{\lambda}_0 = 1$, solve $\Phi_{\vec{u}}\,\dot{\vec{u}}_0 = -\Phi_\lambda$, and then scale $\dot{\lambda}_0$ and $\dot{\vec{u}}_0$ by application of the normalization condition (A.5). Next, the predictor is defined as $\vec{u}^1 = \vec{u}_0 + \Delta S\dot{\vec{u}}_0, \lambda^1 = \lambda_0 + \Delta S\dot{\lambda}_0$.

For the Newton corrector equations (A.7) are linearized using

$$\vec{u}^{n+1} = \vec{u}^n + \Delta\vec{u}^{n+1}, \lambda^{n+1} = \lambda^n + \Delta\lambda^{n+1}, \tag{A.10}$$

the linearization of (A.7b) reading:

$$\dot{\vec{u}}_0^T(\vec{u}^n - \vec{u}_0) + \dot{\vec{u}}_0^T\Delta\vec{u}^{n+1} + (\lambda^n - \lambda_0)\dot{\lambda}_0 + \Delta\lambda^{n+1}\dot{\lambda}_0 - \Delta S = 0. \tag{A.11}$$

As a result the following set of equations is solved for $(\Delta\vec{u}^{n+1}, \Delta\lambda^{n+1})$, starting with the predictor $(\vec{u}^1, \lambda^1)$:

$$\begin{bmatrix}\Phi_{\vec{u}}(\vec{u}^n, \lambda^n) & \Phi_\lambda(\vec{u}^n, \lambda^n) \\ \dot{\vec{u}}_0^T & \dot{\lambda}_0\end{bmatrix}\begin{bmatrix}\Delta\vec{u}^{n+1} \\ \Delta\lambda^{n+1}\end{bmatrix} = \begin{bmatrix}-\Phi(\vec{u}^n, \lambda^n) \\ r^n\end{bmatrix}, \tag{A.12}$$

where

$$r^n = \Delta S - \dot{\vec{u}}_0^T(\vec{u}^n - \vec{u}_0) - \dot{\lambda}_0(\lambda^n - \lambda_0). \tag{A.13}$$

If we define $B = \Phi_{\vec{u}}(\vec{u}^n, \lambda^n)$ and solve $B\vec{z} = -\Phi(\vec{u}^n, \lambda^n), B\vec{y} = \Phi_\lambda(\vec{u}^n, \lambda^n)$ the solution of (A.12) is given by:

$$\Delta\lambda^{n+1} = \frac{r^n - \dot{\vec{u}}_0^T \vec{z}}{\dot{\lambda}_0 - \dot{\vec{u}}_0^T \vec{y}}, \Delta\vec{u}^{n+1} = \vec{z} - \Delta\lambda^{n+1}\vec{y}. \tag{A.14}$$

If ΔS was chosen not too large, $(\vec{u}^n, \lambda^n)$ converged to $(\vec{u}_1, \lambda_1)$ after repeated application of (A.10) and (A.14). As a convergence criterium we used max$|\vec{u}^{n+1}(i,j) - \vec{u}^n(i,j)| < \varepsilon = 10^{-6}$ except near limit and bifurcation points where a larger value had to be used (up to $\varepsilon = 10^{-1}$) due to B becoming nearly singular. The intermediate vectors $\vec{y}$ and $\vec{z}$ were calculated by LU-decomposition of B with partial pivoting and Gauss-elimination. In practical calculations with small to moderate gridsize $(< 100 * 100)$ this direct method proved to be more efficient than iterative methods.

During continuation of a branch the occurrence of a limit point or a bifurcation point was monitored by $q(s) = \det(B)$; q changes sign as the singularity is passed. Discrimination between limit points and bifurcation points is simple: if $\frac{\partial\lambda}{\partial s}$ changes sign too a limit point is passed, else a bifurcation point is encountered. The determinant can be calculated directly as the product of the diagonal elements of the LU-decomposition. After a singularity has been detected its position is accurately determined using a secant algorithm to approximate s_1 satisfying $\det(q(s_1)) = 0$. Let s^0 and s^1 the positions on the branch before and after the singularity respectively, then the following algorithm is applied starting with $i = 1$:

$$s^{i+1} = s^i - q(s^i)\frac{s^i - s^{i-1}}{q(s^i) - q(s^{i-1})}. \tag{A.15}$$

Iteration is stopped if max$|\vec{u}^{n+1}(i,j) - \vec{u}^n(i,j)| < 10^{-2}$ because convergence becomes cumbersome near the singularity.

In case of a bifurcation point a vector $(\vec{u}_{ort}, \lambda_{ort})$ orthogonal to the solution branch is calculated as a first guess to a position on the secondary branch. Let $(\tilde{\vec{u}}, \tilde{\lambda})$ be the point on the branch as the secant iteration has finished, and $\tilde{B}$ and $\tilde{\Phi}_\lambda$ the corresponding matrix and righthandside vector. Then we have to solve the following system:

$$\begin{bmatrix} \tilde{B} & \tilde{\Phi}_\lambda \\ \dot{\vec{u}}_0^T & \dot{\lambda}_0 \end{bmatrix} \begin{bmatrix} \vec{u}_{ort} \\ \lambda_{ort} \end{bmatrix} = \begin{bmatrix} \vec{0} \\ 0 \end{bmatrix}. \tag{A.16}$$

Since $\tilde{B}$ is nearly singular, a close approximation of the eigenvector $\vec{\phi}$ corresponding to the zero eigenvalue can be solved from $\tilde{B}\vec{\phi} = 0$ using inverse iteration (see for example *Golub and Van Loan* [1989]) in a few (2 to 3) steps. A solution to (A.16) can then be expressed in terms of $\vec{\phi}$:

$$\lambda_{ort} = -\frac{\dot{\vec{u}}_0^T \vec{\phi}}{\dot{\lambda}_0 - \dot{\vec{u}}_0^T \tilde{B}^{-1}\tilde{\Phi}_\lambda}, \vec{u}_{ort} = \vec{\phi} - \lambda_{ort}\tilde{B}^{-1}\tilde{\Phi}_\lambda. \tag{A.17}$$

The predictors $\vec{\tilde{u}}^1 = \vec{\tilde{u}} \pm \Delta S \vec{u}_{ort}, \tilde{\lambda}^1 = \tilde{\lambda} \pm \Delta S \lambda_{ort}$ are used to start the continuation of both parts of the secondary branch.

Appendix B

Linear stability

For the determination of the linear stability of a solution of (A.3) a generalized eigenvalue problem has to be solved of the form

$$A\vec{u} = \chi D\vec{u} \tag{B.1}$$

where diagonal matrix D is singular due to Dirichlet boundary conditions.

We only need to calculate those eigenvalues that are close to the imaginary axis since a change in them might change the stability of the solution. To calculate the eigenvalues first a mapping

$$\chi = \frac{\tau - 1}{\tau + 1}, \tau \in \mathcal{C}/\{-1\} \tag{B.2}$$

is applied which maps $\mathcal{C}^-$, the imaginary axis and $\mathcal{C}^+$ onto $|\tau| < 1$, $|\tau| = 1$ and $|\tau| > 1$ respectively. The dominant eigenvalues τ are then calculated from the transformed eigenvalue problem

$$-(A + D)\vec{u} = \tau(A - D)\vec{u}. \tag{B.3}$$

The calculation is started with a number of independent vectors equal to the desired number of eigenvalues. Infinite eigenvectors of (B.3) are first filtered out from the starting vectors by inverse iteration. Next the dominant eigenvalues are calculated using simultaneous iteration.

The solution is linearly stable if all eigenvalues have negative real parts. If at least one of the eigenvalues has a positive real part the solution is unstable. A Hopf bifurcation point is detected if a complex pair of eigenvalues $\sigma = \zeta \pm i\tau$ crosses the imaginary axis. Its position can be accurately determined using the previously described secant algorithm with $q(s) = \zeta(s)$.

Appendix C

A flux law for vertical salt transport

In double-diffusive systems as studied in this thesis, the vertical salinity distibution has a characteristic ”step”-structure, i.e. salt is well mixed within the convective layers, but strong salinity gradients exist within the diffusive interfaces. The ”step”-structure allows the formulation of a flux law for the vertical salt flux which depends on the overall temperature and salinity differences. Flux laws of this type have been formulated first for a double-diffusive system heated from below, containing only one diffusive interface, but their applicability has been shown for systems of layers as well [*Huppert*, 1971; *Turner*, 1973]. Since the vertical salinity distribution in the laterally heated case is similar to the vertically heated case, we apply the theory in a similar way. We regard a diffusive interface extending infinitely into the horizontal, enclosed by a cool and fresh layer (top) and a warm and salty layer (bottom), where each of the layers has a thickness h (m).

The Sherwood number Sh is a measure of the vertical salt transport through the interface and is defined as follows (dimensional quantities are denoted by a star):

$$Sh = \frac{F_S^*}{\kappa_S(-\delta S^*)/h}, \tag{C.1}$$

where F_S^* (m s^{-1}) is the vertical salt flux, h is the height of a convective layer ($h = O(\eta)$ as shown in this thesis) and δS^* is the jump in salinity across the diffusive interface.

In a steady-state situation, Sh can be formally expressed as [*Turner*, 1973]:

$$Sh = Sh(Ra_{\delta T}, Ra_{\delta S}, Pr, Le), \tag{C.2}$$

where

$$Ra_{\delta T} = \frac{g\alpha(-\delta T^*)h^3}{\nu\kappa_T}. \tag{C.3}$$

$$Ra_{\delta S} = \frac{g\beta(-\delta S^*)h^3}{\nu\kappa_T}. \tag{C.4}$$

Since salt is uniformly distributed in the convective layers, the salt flux through the diffusive interfaces must be independent of the layer thickness h. This condition is satisfied if we combine (C.1) and (C.2) as follows (different combinations are also possible):

$$Sh = c_S\ (Ra_{\delta S})^{1/3}, \tag{C.5}$$

where the coefficient c_S may still depend on $R_\rho = R\delta S/\delta T$ (Pr and Le are kept constant in our simulations).

Eliminating h from (C.5), substituting $\delta S^* = \Delta S\ \delta S$ and applying (C.1) we arrive at the following expression for F_S^*:

$$F_S^* = \kappa_S \Delta S\ c_S\ (\frac{g\beta\Delta S}{\nu\kappa_T})^{1/3}\ (-\delta S)^{4/3}. \tag{C.6}$$

Now F_S^* is made dimensionless using $F_S = F_S^*\ H/\kappa_T\Delta S$, which results in (absorbing the ratio κ_S/κ_T into c_S):

$$F_S = c_S\ (\frac{g\beta\Delta S H^3}{\nu\kappa_T})^{1/3}\ (-\delta S)^{4/3}, \tag{C.7}$$

or, with $Ra_S = g\beta\Delta S H^3/\nu\kappa_T$, and $Ra_\eta = Ra_S R^{-4}$:

$$F_S = c_S\ (Ra_\eta R^4)^{1/3}\ (-\delta S)^{4/3}. \tag{C.8}$$

Expression (C.8) is used in Chapter 6 to investigate the validity of the flux-law assumptions for the presented simulations.

References

Dijkstra, H. A., On the structure of cellular solutions in Rayleigh-Bénard-Marangoni flows in small-aspect-ratio containers, *J. Fluid Mech.*, **243**, 73–102 (1992).

Dijkstra, H. A., An efficient code to compute non-parallel steady flows and their linear stability, *Computers & Fluids*, **24**(4), 415–434 (1995).

Golub, G. H., and Van Loan, C. F., Matrix Computations, The Johns Hopkins University Press (1989)

Huppert, H. E., On the stability of a series of double-diffusive layers, *Deep-Sea Res.*, 18, 1005-1021 (1971).

Jackson, C. P., A finite-element study of the onset of vortex shedding in flow past variously shaped bodies, *J. Fluid Mech.*, **182**, 23–45 (1987).

Keller, H. B., Numerical solutions of bifurcation and nonlinear eigenvalue problems, Applications of Bifurcation Theory, Academic, 359–384 (1977).

Riley, D. S., and Winters, K. H., Modal exchange mechanisms in Lapwood convection, *J. Fluid Mech.*, **204**, 325–358 (1989).

Turner, J. S., *Buoyancy effects in fluids*, Cambridge (1973).

Seydel, R., *Practical Bifurcation and Stability Analysis*, IAM **5**, Springer Verlag (1994).